

# Suspension Taylor-Couette flow

Investigation of particle loading effects on transitions between flow regimes

Arjun Anantharaman

Technische Universiteit Delft





# Suspension Taylor-Couette flow

Investigation of particle loading effects on  
transitions between flow regimes

by

**Arjun Anantharaman**

to obtain the degree of Master of Science  
at the Delft University of Technology,  
to be defended on Friday October 25, 2019 at 02:00 PM.

Student number:	4741110	
P&E report number:	3000	
Project duration:	Jan 2019 – October 2019	
Thesis committee:	Prof. dr. ir. C. Poelma,	TU Delft, supervisor and chair
	Dr. ir. Gerrit E. Elsinga,	TU Delft
	Dr. ir. M. J. B. M. Pourquie,	TU Delft
	Ir. A. Dash,	TU Delft, daily supervisor

An electronic version of this thesis is available at <http://repository.tudelft.nl/>.



# Abstract

Taylor-Couette (TC) flow refers to the flow in the annulus between two coaxial, independently rotating cylinders. The TC system has been subject to multiple experiments spanning over decades due to the instability phenomena that occur in the flow. Initially used to validate the Newtonian stress assumption and as a viscometer, the TC system is primarily used in stability analysis in academia and has industrial applications as a bio-reactor for particle mixing. When the rotation rates of the cylinders are increased beyond a critical value, instabilities appear in the system that result in the formation of different flow regimes. Single-phase flow in the TC system has been studied extensively and the various flow transitions have been catalogued for different geometrical parameters and rotational conditions.

In the current experiments (Radius ratio ( $\eta$ )=0.917, Aspect ratio ( $\Gamma$ )=22), flow visualisation with anisotropic reflective particles has been used to obtain qualitative and quantitative information about the different flow regimes using Space-Time (S-T) plots and their spectral analyses. An aqueous glycerine solution was used as the working fluid for single-phase flows. With a stationary outer cylinder and a rotating inner cylinder from rest, laminar Couette flow transitions to "Taylor Vortex Flow (TVF)", where the flow arranges itself into pairs of counter-rotating vortices along the cylinder axis. The critical Reynolds number (calculated based on inner cylinder shear rate) for this transition was found to be slightly higher for the current setup in comparison to other experiments found in literature, but the order of flow transitions and their spectral characterisation for all the flow regimes showed good agreement, serving as a validation for the setup. A flow map was constructed based on the order of transitions and the regimes characterised included wavy vortices, modulated waves, chaotic waves and turbulent waves. In addition to the S-T plots, the frequency of the waves also helped to classify the transitions based on the number of azimuthal waves that were present in the system.

With the established single-phase flow as a base, the effect of particle loading on the flow transitions was studied using the aforementioned techniques. A neutrally buoyant particle-laden suspension was prepared using an aqueous glycerine solution with Poly(methyl methacrylate) (PMMA) particles of  $619 \mu\text{m}$  mean diameter. The volume fraction ( $\phi$ ) of the particles was varied from 0.05 till 0.40 and the flow map was constructed for multi-phase flow. The primary effect of particle addition is an earlier onset of the first transition from laminar Couette flow, thus indicating a destabilisation of the flow by particles. In addition to this, several non-axisymmetric flow structures appeared in the suspension experiments which were absent in the single-phase flow experiments. The particles caused the appearance of flow regimes such as spirals (Taylor vortices that move up the cylinder axis in a helical motion) and ribbons (block-like structures that have alternating light and dark squares), which normally occur in the case of counter-rotating cylinders for single-phase flow. The transitions across all volume fractions were characterised based on the S-T plots and/or spectra to obtain a consolidated flow map for particle-laden suspensions.

A single case of 10% particle loading was analysed in detail and a transition map was constructed. Several non-axisymmetric regimes were observed, and in many measurements, multiple flow regimes coexisted. This was also observed in recent studies found in literature, but they showed different flow transitions. The ribbon/ribble regime was observed in this system, and its formation was attributed to the combination of spirals having opposite inclinations. An interesting outcome of the analysis showed that the types of spirals seemed to be particle loading dependent. The reason for this is yet to be determined and is recommended for future work. The nature of the analysis is mainly qualitative due to the uncertainties in the actual flow conditions and coarseness in the Reynolds number step size. However, the results presented point towards intriguing flow behaviour that provides a large parameter space for further research in the years to come.



# Acknowledgement

Firstly, I would like to thank all the people in the lab for helping me with inputs and suggestions throughout my thesis. I have received valuable inputs from many people over nine months, so forgive me if I have left some names out in this section. I would like to thank **Amitosh Dash** for guiding me through every step of the project, and **Professor Christian Poelma** for giving useful suggestions and keeping a strict deadline that motivated me to work even harder to complete a good thesis within time. I would also like to thank the thesis committee members **Gerrit Elsinga** and **Mathieu Pourquoi** for taking the time to be a part of my defence.

In the lab, I would like to extend my gratitude to **Arnoud Greidanus**, **Jan Graafland**, **Edwin Overmars** and **Jasper Ruijgrok** for helping me with the Taylor-Couette setup and ensuring that the experiments were conducted in spite of the multiple issues that arose.

I'm not going to thank my family or friends, as I believe it is belittling to thank them in an acknowledgement. Friends and family do not act out of receiving thanks, and there now exists a paragraph that shouldn't have been there in the first place.

There is a lot of suffering in this world and as we talk about climate change, freedom of speech and equality, I feel privileged to have access to the facilities available to me today. I wrote a small placeholder initially in this section as I did not have any idea what to write or how to write it. However, it encapsulates perfectly my current state of mind and I will end on that same note:

*I am thankful for this mere existence*

*Arjun Anantharaman  
Delft, October 2019*



# Nomenclature

## Physical Constants

$g$	Gravitational Constant	$6.67384 \times 10^{-11} \text{ Nm}^2\text{kg}^{-2}$
$k_B$	Boltzmann constant	$1.38064852 \times 10^{-23} \text{ m}^2\text{kgs}^{-2}\text{K}^{-1}$

## Symbols

$r_{i,o}$	Inner, outer cylinder radii	[mm]
$\eta$	Radius ratio	[-]
$\Gamma$	Aspect ratio	[-]
$d$	Gap width	[mm]
$L$	Cylinder length (outer)	
$Re_{i,o}$	Inner, outer cylinder Reynolds numbers	[-]
$\nu_{f,s}$	Fluid and suspension viscosities (kinematic)	$[\text{m}^2\text{s}^{-1}]$
$\mu_{f,s}$	Fluid and suspension viscosities (dynamic)	$[\text{Pa} \cdot \text{s}]$
$\rho_{p,s}$	Particle and fluid densities	$[\text{kgm}^{-3}]$
$f_{i,o}$	Inner, outer cylinder rotational frequencies	[Hz]
$\Omega_{i,o}$	Inner, outer cylinder angular velocities	$[\text{rads}^{-1}]$
$d_{p,\text{diff}}$	Particle diameter and diffraction limited spot diameter	$[\mu\text{m}]$
$f_{\#}, M, \text{NA}$	f-number, magnification and Numerical Aperture of the camera lens	[-]
$\lambda$	Wavelength of illuminating light	[nm]
$\nu_{\text{sed}}$	Sedimentation velocity	$[\text{ms}^{-1}]$
$f_{\text{rot}}$	Inner cylinder rotational frequency	[Hz]
$f_{\text{dom},1}$	First temporal dominant frequency obtained from the power spectrum	[Hz]
$f_{\text{sp}}$	Spatial dominant frequency obtained from the power spectrum	$[\text{mm}^{-1}]$
$\omega^*, k$	Distinct temporal and spatial frequencies	[-]
$Re_p$	Particle Reynolds number	[-]
$St, Pe$	Stokes and Peclet numbers	[-]
$\nu_{f,s}$	Shear rate of the system	$[\text{s}^{-1}]$
$\phi$	Particle volume fraction	[-]

## Abbreviations

TC	Taylor Couette
LAM/CCF	Laminar/Circular Couette Flow

---

TVF	Taylor Vortex Flow
WVF	Wavy Vortex Flow
MWV/MWVF	Modulated Wavy Vortex Flow
CWV	Chaotic Wavy Vortices
WTV	Wavy Turbulent Vortices
TTV	Turbulent Taylor Vortices
SVF	Spiral Vortex Flow
WSVF	Wavy Spiral Vortex Flow
TW	Travelling Waves
IPS	Inter Penetrating Spirals
RIB	Riblets/Ribbons
v-K	von-Karman
DAQ	Data acquisition system
PTU	Programmable Timing Unit
FOV	Field Of View
LED	Light Emitting Diode
IR	Infra-Red
PMMA	Poly(methyl methacrylate)
FWHM	Full Width Half Maximum
QS	Quasi Steady
S-T	Space-Time
FFT	Fast Fourier Transform

# List of Figures

1.1	TC schematic and setup picture at TU Delft	2
1.2	TVF formation mechanism	3
1.3	Stability criteria of Taylor and Rayleigh	4
1.4	Transition from laminar flow to TVF	4
1.5	Multiplicity of states in the WVF	5
1.6	Modulation appearance in the MWVF regime	6
1.7	Transition map of Dutcher and Muller based on distinct spatial and temporal frequencies	6
1.8	Andereck's flow map for inner and outer cylinder rotation	7
1.9	Particle trajectory in SVF	8
1.10	Spiral formation for counter rotating inner and outer cylinders	8
1.11	Explored parameter space for TC flow at higher Reynolds numbers	8
1.12	Development of Taylor vortices with end effects	10
1.13	End cap boundary inflow caused Ekman circulation	10
1.14	Radius ratios covered in TC experiments	10
1.15	Particle migration in pipe flows showing the formation of the Segre-Silberberg annulus	11
1.16	Particle migration in CCF	12
1.17	Particle migration in TVF	12
1.18	Transition map for single phase TC flow from Majji et al.	13
1.19	S-T plots of spirals and ribbons in the TC system	13
1.20	S-T diagrams of L and R type spirals constructed from velocity fields using linear stability analysis	13
1.21	Flow map of all observed transitions in the experiments of Majji et al.	14
1.22	Coexisting TVF and SVF observed by Ramesh et al.	14
2.1	Schematic overview of the experimental setup used for the current experiments	17
2.2	Schematic of the TC system with the important dimensions indicated	18
2.3	Outer and inner cylinders after disassembly	19
2.4	Image of the camera directed at the TC system for imaging	19
2.5	Calibration grid used to obtain spatial information from the TC system	19
2.6	Estimated fluid temperature as a function of time based on the wall temperature	21
2.7	Raw microscope images of PMMA particles and the corresponding calibration grid	23
2.8	Particle size distribution graphs	23
2.9	Full Width Half Maximum (FWHM) convergence for particle size determination	24
3.1	Representation of the two types of experimental runs: QSup and QSDown	28
3.2	Data processing steps starting from image capture till the extraction of useful data	29
3.3	Steps followed to process the images and form S-T plots	30
3.4	Variation of dimensionless torque ( $G$ ) with the Reynolds number ( $Re_i$ )	31
3.5	$Nu^\omega$ variation with $Re_i$ showing the transition to TVF	32
3.6	Skin friction coefficient $c_f$ plotted as a function of shear Reynolds number, $Re_s$	33
3.7	Snapshot of the laminar TC flow, with and without Ekman vortices	34
3.8	Power spectrum of the S-T plot for the spatial and temporal frequencies in Couette flow	35
3.9	S-T plot of the laminar Couette flow regime ( $Re_i = 58$ ) in the current TC cell	35
3.10	Snapshot of the Taylor vortices occupying the whole TC cell along with schematic	36
3.11	Power spectrum of the S-T plot for the spatial and temporal frequencies in TVF	36
3.12	S-T plot of the TVF regime in the current TC cell	37
3.13	Snapshot and representation of the wavy vortices in the TC system	37
3.14	Power spectrum of the S-T plot for the spatial and temporal frequencies in WVF	38
3.15	S-T plot of the WVF regime	38
3.16	Snapshot of the TC cell with modulated waves at $Re_i=1233$	39

3.17	Power spectrum of the S-T plot for the spatial and temporal frequencies in MWVF . . . . .	39
3.18	S-T plot of the MWVF regime in the current TC cell . . . . .	40
3.19	Spectral plots of temporal frequency for CWV and WTV . . . . .	41
3.20	S-T plots of CWV and WTV . . . . .	41
3.21	Power spectrum of the S-T plot for the spatial and temporal frequencies in TTV . . . . .	42
3.22	Snapshot and S-T plot of the TC cell with the turbulent Taylor vortices . . . . .	42
3.23	Transition map for the QSDown and QSup experiments . . . . .	43
3.24	S-T plot of the entire QSDown experiment . . . . .	44
3.25	Close-up of region 'A' in Figure 3.24 . . . . .	44
3.26	Close-up of region 'B' in Figure 3.24 and S-T plot showing the development of transients . . . . .	45
3.27	Close-up of 'C' in Figure 3.24 showing three regimes within this range of Reynolds numbers . . . . .	45
3.28	Variation of the peak dominant frequency (normalised) with the Reynolds number for the QSDown case . . . . .	46
3.29	Snapshots of the TC system showing a change in the wavelength of WVF . . . . .	47
3.30	Close up of Figure 3.28, focussing on region 'B' . . . . .	47
3.31	Close up of Figure 3.28, focussing on region 'C' . . . . .	48
4.1	Variation of the particle to fluid density ratio ( $\rho_p/\rho_f$ ) and dynamic viscosity ( $\mu_s$ ) with volume fraction ( $\phi$ ) . . . . .	50
4.2	Snapshot and power spectrum of the spiral vortex flow for $\phi = 0.30$ . . . . .	51
4.3	Space-time plot of the spiral vortex flow for $\phi = 0.30$ . . . . .	52
4.4	Snapshot and power spectrum of the wavy spiral vortex flow for $\phi = 0.20$ . . . . .	53
4.5	Space-time plot of the wavy spiral vortex flow for $\phi = 0.20$ . . . . .	53
4.6	S-T plot of the IPS regime containing both types of spirals for $\phi = 0.20$ . . . . .	54
4.7	Complete transition map for $\phi = 0.10$ , QSDown . . . . .	55
4.8	The three interesting regions from Figure 4.9 are split up and shown here. . . . .	56
4.9	S-T plot for the entire QSDown experiment of $\phi = 0.10$ , QSDown . . . . .	57
4.10	S-T plot of MWVF + WSVF showing the wavy spirals forming in the latter half of the recording . . . . .	58
4.11	Spectra of the regimes MWVF and MWVF + WSVF . . . . .	58
4.12	S-T plots of the MWVF + WSVF and MWVF regimes. . . . .	59
4.13	Spectra of the MWVF + WSVF and MWVF regimes . . . . .	59
4.14	S-T plots of the TVF + TW and TVF + SVF regimes . . . . .	60
4.15	Spectra of the TVF + TW and TVF + SVF regimes . . . . .	60
4.16	Variation of the normalised dominant frequency (first peak from power spectrum) with the Reynolds number . . . . .	61
4.17	Snapshots of the TC system showing the change from 9 azimuthal modulated waves at $Re_i = 582$ to 8 wavy vortices at $Re_i = 617$ . . . . .	62
4.18	Snapshots of the TC system showing a reduction in number of azimuthal waves from 8 ( $Re_i = 811$ ) to 7 ( $Re_i = 866$ ) . . . . .	62
4.19	Snapshots of the TC system showing the change from wavy low wave amplitude flow at $Re_i = 942$ to a modulated high wave amplitude flow regime at $Re_i = 978$ . . . . .	63
4.20	Snapshots of the TC system showing the change from '4' ( $Re_i = 1384$ ) to '5' ( $Re_i = 1419$ ) . . . . .	63
4.21	Complete flow map showing all the transitions across volume fractions (QSDown) . . . . .	64
4.22	First onset of instability from Couette flow across all volume fractions . . . . .	65
4.23	Partial riblets seen in the S-T plot of $\phi = 0.15$ at $Re_i = 125$ . . . . .	66
4.24	S-T plot of $\phi = 0.25$ at $Re_i = 134$ showing the coexistence of both L and R type spirals . . . . .	67
4.25	Graphical representation of the types of spirals that appear in the experiments . . . . .	67
A.1	Correction of the offset error in the torque values . . . . .	71
A.2	Raw TTL signal, where each pulse corresponds to 36 degrees of the inner cylinder rotational frequency . . . . .	72
A.3	FFT of the raw TTL data . . . . .	72
A.4	The ratio of the actual frequency of rotation computed from the TTL data to the input vs the Reynolds numbers . . . . .	72
A.5	Convergence of the torque value for a single measurement showing that the mean torque is converged to 1% of its true mean within 10 seconds . . . . .	73

---

A.6	Determination of the wavelength of the flow from snapshots . . . . .	74
C.1	The disassembled setup showing the Iridin particles sticking to the wall surface . . . . .	77
C.2	Stearic acid solution prepared from Gillette shaving foam . . . . .	78
D.1	Shaker and sieve setup used to filter particles along with the microscope used for analysing particle size . . . . .	80
D.2	Density meter reading of the working fluid (without particles). . . . .	81
D.3	Temp calibration for the PT100 sensor with boiling water. Other sensors from the lab were used for reference. . . . .	81
D.4	Coupling connections and rubber coupling wearing . . . . .	82
D.5	Steps in setup disassembly . . . . .	82
D.6	Images of the setup with the labelled components. The filling hole is held in place by a screw. . . . .	84
D.7	Synchronised imaging measurements controlled by the Dell 7577 and ultrasound measurements performed by Amitosh. . . . .	84



# List of Tables

2.1	Parameters of the TC setup and their corresponding values . . . . .	18
2.2	Viscosity and Reynolds number dependence on temperature for a fixed rotational speed of 1 Hz	20
2.3	Density variation with temperature and its effect on both the neutral buoyancy and the settling time . . . . .	25
3.1	Table showing the different types of images recorded for each rotational frequency . . . . .	29
4.1	Comparison of the important dimensionless parameters between the present study and literature	50
B.1	The order of transition in all of the particle laden suspension experiments (QSDown) . . . . .	76



# Contents

<b>List of Figures</b>	<b>ix</b>
<b>List of Tables</b>	<b>xiii</b>
<b>1 Introduction</b>	<b>1</b>
1.1 Taylor-Couette flow: What is it and why does it fascinate? . . . . .	1
1.1.1 The stability criterion and Taylor vortex flow. . . . .	1
1.1.2 To wavy vortex flow, and beyond! . . . . .	4
1.2 Taylor-Couette flow with two rotating cylinders. . . . .	7
1.3 Flow visualisation. . . . .	9
1.4 Geometry and initial condition effects . . . . .	9
1.5 Particle-laden suspension studies. . . . .	11
1.6 Taylor-Couette flow with particles . . . . .	11
1.7 Research goals . . . . .	15
1.8 Organisation of the report. . . . .	15
<b>2 Experimental setup</b>	<b>17</b>
2.1 Geometry of the TC cell . . . . .	17
2.2 Measurement devices. . . . .	19
2.2.1 Imaging optics . . . . .	19
2.2.2 Temperature . . . . .	20
2.2.3 Torque measurement and rotation control. . . . .	21
2.3 Suspension and particles . . . . .	22
2.3.1 Working fluid and flow visualisation . . . . .	22
2.3.2 Particle properties and size distribution . . . . .	22
2.3.3 Suspension preparation . . . . .	24
<b>3 Single-phase flows: Validation</b>	<b>27</b>
3.1 Data processing. . . . .	27
3.1.1 Experimental test matrix. . . . .	27
3.1.2 Imaging . . . . .	28
3.1.3 Space-Time (S-T) plots. . . . .	29
3.1.4 Torque measurements . . . . .	31
3.2 Flow regimes in the Taylor-Couette system . . . . .	34
3.2.1 Laminar Couette flow . . . . .	34
3.2.2 Taylor Vortex Flow (TVF) . . . . .	35
3.2.3 Wavy Vortex flow (WVF) . . . . .	37
3.2.4 Modulated Wavy Vortex flow (MWVF/MWV). . . . .	39
3.2.5 Turbulent Taylor Vortices (TTV) . . . . .	42
3.3 Transition map . . . . .	43
3.3.1 S-T transition and hysteresis comparison . . . . .	43
3.3.2 Transition/state S-T analysis - QSDown . . . . .	44
3.3.3 Transition/state frequency analysis - QSDown. . . . .	46
<b>4 Multiphase flows</b>	<b>49</b>
4.1 Experimental parameters . . . . .	49
4.2 Flow regimes unique to particle-laden flow . . . . .	51
4.2.1 Spiral Vortex Flow (SVF) . . . . .	51
4.2.2 Wavy Spiral Vortex Flow (WSVF) . . . . .	52
4.2.3 Unstable regimes . . . . .	54

4.3	$\phi = 0.10$ , a case study . . . . .	55
4.3.1	WVF to MWVF to MWVF + WSVF . . . . .	58
4.3.2	MWVF + WSVF to MWVF to WVF . . . . .	59
4.3.3	TVF to TVF + TW to TVF + SVF . . . . .	60
4.3.4	Transitions between wave patterns . . . . .	61
4.4	Discussion on overall transition behaviour . . . . .	64
4.4.1	Destabilising effect of particles. . . . .	65
4.4.2	Effect of short experimental time . . . . .	65
4.4.3	Ribbon and spiral formation dependence on particle loading . . . . .	66
<b>5</b>	<b>Conclusions and recommendations</b>	<b>69</b>
5.1	Conclusions. . . . .	69
5.2	Recommendations . . . . .	70
5.2.1	Experiment . . . . .	70
5.2.2	Analysis and methodology. . . . .	70
<b>A</b>	<b>Data processing and analysis</b>	<b>71</b>
A.1	Determination of the torque offset . . . . .	71
A.2	TTL signal processing for $f_{in}$ determination. . . . .	71
A.3	Determination of experimental time - convergence of torque. . . . .	73
A.4	Determination of the wavelengths of wavy vortices . . . . .	73
<b>B</b>	<b>Multiphase flow regime classification</b>	<b>75</b>
<b>C</b>	<b>Flow visualisation alternatives</b>	<b>77</b>
<b>D</b>	<b>Setup operation and intricacies</b>	<b>79</b>
D.1	Experimental protocol . . . . .	79
D.2	Preparation of the suspension and particles . . . . .	80
D.2.1	Suspension . . . . .	80
D.2.2	Particles . . . . .	80
D.3	Maintaining neutral buoyancy in spite of global warming induced heatwaves . . . . .	80
D.4	Temperature calibration of lab sensors . . . . .	81
D.5	Setup disassembly . . . . .	82
D.6	Miscellaneous setup images . . . . .	84
	<b>Bibliography</b>	<b>85</b>

# 1

## Introduction

One look at the flow in the gap between two concentric cylinders is all it takes for physicists and engineers alike to have been intrigued for more than 300 years [1]. The beautiful flow structures that develop comprising of vortices, spirals and even herringbone-like structures are only small facets in this heavily investigated section of fluid dynamics. The Taylor-Couette setup gets its name firstly from Maurice Couette, who used it as a viscometer to further his rheological studies of various liquids. The stability of the flow in this system was scrutinised by G.I.Taylor in his classic paper [2] wherein the mathematical basis for the stability of this Taylor-Couette flow was formulated along with experiments.

This system has been the subject of intense research, both academic and application-oriented. In the 19<sup>th</sup> century, it was used to validate the Newtonian stress assumption in the Navier-Stokes equations and also gave further insights into the no-slip boundary condition, linear stability analysis and so on. Few reasons as to why it is so commonly used mainly are due to the closed and simple nature of the setup, the quality of flow visualisation and easy comparison/validation between experiments, numerical and analytical studies [3]. In addition to the academic applications, this setup itself is primarily used as a viscometer as well as Taylor-Couette bio-reactors with applications in the chemical industry [4, 5]. This chapter first delves into the basics of what the Taylor-Couette flow is and slowly gets into the motivation and research questions of this thesis.

### 1.1. Taylor-Couette flow: What is it and why does it fascinate?

#### 1.1.1. The stability criterion and Taylor vortex flow

Taylor-Couette (TC) flow refers to the flow in the annulus between two concentric cylinders. Independently, Couette and Mallock used Taylor-Couette setups for viscometry [1] in 1888. The nomenclature for the coordinates is as follows: axial direction is along the axis of the cylinder, azimuthal refers to the direction along the circumference of the cylinders and is curved in nature, radial refers to the direction along the radius of the cylinder. A snapshot of the system used for experiments in the lab for Aero and Hydrodynamics at TU Delft is shown alongside a schematic in Figure 1.1. The inner and outer cylinder radii are  $r_i$  and  $r_o$  respectively, the column height is  $L$ , the gap width  $d = r_o - r_i$  and the end height at both the top and bottom (assumed equal) is given by  $h$ . Two important parameters that are used to define this setup are the aspect ratio,  $\Gamma = L/d$  and the radius ratio,  $\eta = r_i/r_o$ .

The equations describing the flow are the simplified solutions of the Navier-Stokes equations in cylindrical coordinates  $(r, \theta, z)$  for infinitely long cylinders, commonly referred to as "Couette flow":

$$u_\theta = 0, \quad u_r = Ar + \frac{B}{r}, \quad u_z = 0$$

where  $u_r$ ,  $u_\theta$ ,  $u_z$  are the radial, azimuthal and axial velocity components. A and B are coefficients that depend on the geometry of the system and the rotational inputs of the system as:

$$A = -\Omega_i \frac{\eta^2 - \mu}{1 - \eta^2}, \quad B = \Omega_i \frac{r_i^2(1 - \mu)}{1 - \eta^2}$$

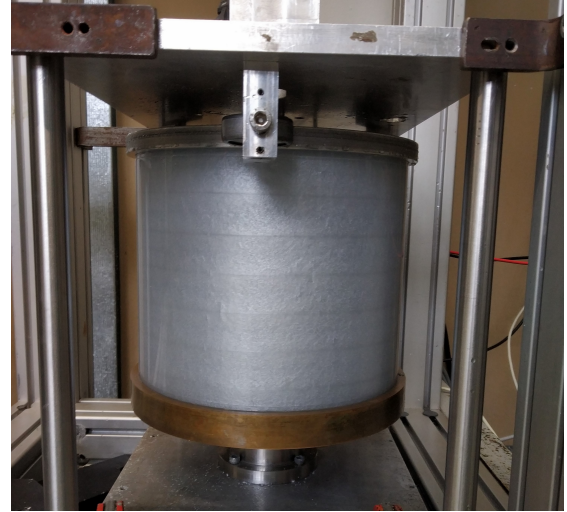
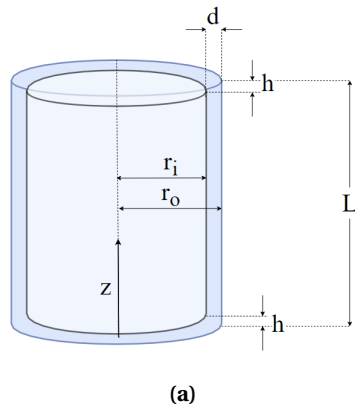


**Figure 1.1:** (a) Schematic representation of the TC system (front view) with dimensions and  $z$ -coordinate defined. (b) Picture of the Taylor-Couette system at the lab for Aero and Hydro-dynamics, TU Delft used for the current experiments

where  $\Omega_{i,o}$  are the rotational inputs given to the inner/outer cylinders and  $\mu = \Omega_o/\Omega_i$ . Given that the solution of this flow is symmetric about  $\theta$  and  $z$  and obtaining the known values of torque and angular velocities present, the viscosity of the fluid is given by the ratio of the global shear stress and shear rates. Couette and Mallock found that this gave a constant value below a critical shear rate, and that this constant value was more when only the outer cylinder was rotated. The equations describing the global quantities can be found in the review paper by Fardin et al. [6].

The stable form of the flow is referred to as cylindrical ‘Couette flow’ where there are no distinct flow features. For the configuration of a stationary outer cylinder and a rotating inner cylinder, instabilities set in after the rotational speed of the inner cylinder exceeds a certain critical limit. To understand why the instabilities creep in, the forces on the fluid during rotation have to be looked at. Two forces act simultaneously on a rotating fluid layer between two concentric cylinders. The centrifugal force that pushes the fluid away from the centre is balanced by the inward-directed pressure gradient. A disruption of this balance in the case of higher centrifugal forces will cause instabilities to set in the form of vortical structures. The fluid tends to arrange itself into counter-rotating toroidal vortices that fill the entire flow section, commonly referred to as Taylor vortices. They are visible as bands when the Taylor-Couette cell is looked at head-on, thus presenting a good case for visualisation. This state appears as alternating bands of light and dark, and this pair of counter-rotating vortices form such a pattern due to the presence of inflow and outflow boundaries. The inflow boundaries are darker and the outflow boundaries are bright, as seen from Figure 1.2, taken from the detailed book on TC flow by Chossat and Iooss [7].

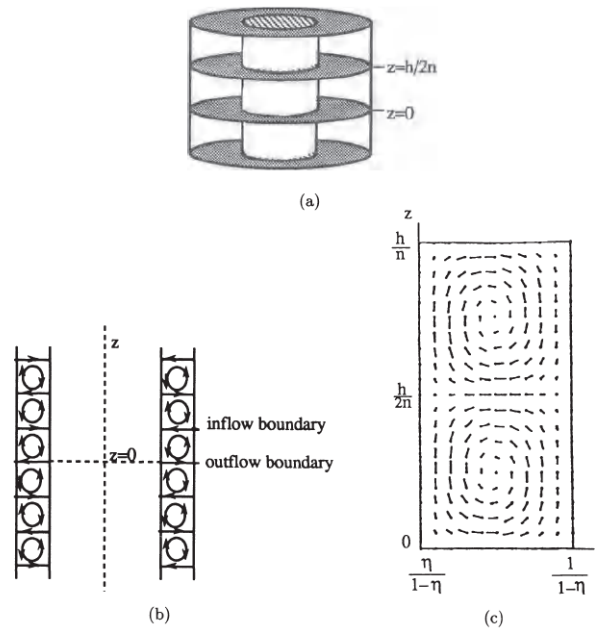


**Figure 1.2:** Taylor vortex flow, with the streamlines indicated along with the presence of inflow and outflow boundaries, from Chossat and Iooss [7]

The development of this instability was first explained by Lord Rayleigh, who devised a stability criterion that detailed "A circulation always increasing outwards . . . ensures stability " [8], given by :

$$\frac{d(rv)^2}{dr} = \frac{d}{dr}(r^2\Omega)^2 > 0$$

Applying the base solution for Couette flow in the stability criterion, for the same direction of cylinders' rotations,

$$\frac{\Omega_o}{\Omega_i} > \left(\frac{r_i}{r_o}\right)^2$$

This is illustrated in the stability diagram in Figure 1.3a. However, this indicates that for pure outer cylinder rotation, the flow is always stable. Also, if the case of a fixed outer cylinder and a rotating inner cylinder is taken, the centrifugal force decreases in the radial direction and the flow should always be unstable, which is not the case. The effect of viscous forces stabilising the flow was taken into account by Taylor in addition to the conditions imposed by Rayleigh. Taylor set to study the development of instabilities further as he found that the Mallock and Couette experiments did not seem appropriate to confirm Rayleigh's stability criterion. First, the equations describing the flow were subjected to small axisymmetric disturbances for stability analysis. The boundary conditions used by him did not consider the horizontal ends of the cylinder column (infinitely long cylinders) and to simplify equations further, a narrow gap approximation was used ( $\eta \rightarrow 1$ ). Fardin et al. [6] remarked: "Prandtl was the first to notice that Taylor's theoretical result for small gaps and stationary outer cylinders could be put approximately in the form":

$$\left(\frac{\Omega_i r_i d}{\nu} \sqrt{\frac{d}{r_i}}\right) \approx 41.2$$

The term on the left-hand-side is commonly referred to as the square root of the Taylor number (sometimes also as the Taylor number itself). This term was first used by Chandrasekhar [9], and it gives the ratio of the centrifugal (inertial) to the viscous forces.

$$\text{Ta} = \frac{4\Omega_i^2 d^4}{\nu^2} = \text{Re}_i^2 \frac{d}{r_i}$$

where  $\text{Re}_i$  is the inner cylinder Reynolds number of radius  $r_i$  and the TC gap width is  $d = r_o - r_i$ . The Reynolds numbers used to describe and classify the flow regimes are given by:

$$\text{Re}_i = \frac{\Omega_i r_i d}{\nu}$$

$$\text{Re}_o = \frac{\Omega_o r_o d}{\nu}$$

The stability criterion dictated by this Taylor number is illustrated in Figure 1.3b and this determines the onset of Taylor vortices in narrow gap TC flow. This is observed in the TC system, shown in Figure 1.4. This transition is characterised by a critical Taylor number ( $\text{Ta}_c$ ) or a critical Reynolds number ( $\text{Re}_c$ ).

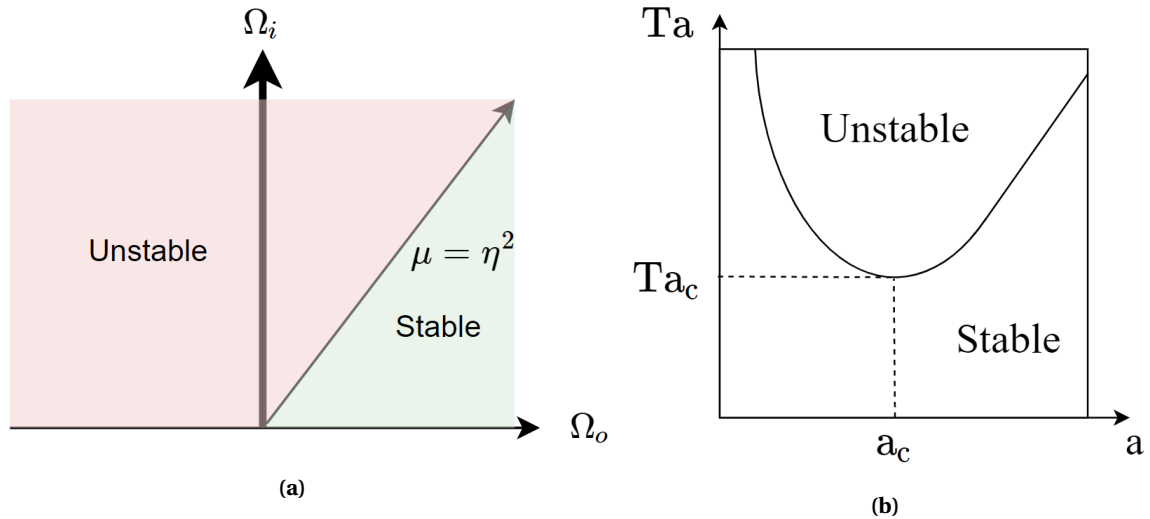


**Figure 1.3:** Illustrations of Rayleigh's stability criterion (a) and Taylor's stability criterion (b), adapted from Koschmeider [8]. The Rayleigh stability criterion was used as a base by Taylor to devise a comprehensive analysis for the Taylor-Couette system. The laminar Couette flow transitions to Taylor vortex flow at the critical Taylor number,  $\text{Ta}_c$ . The Taylor number is plotted as a function of the non-dimensional wave number of the flow, ' $a$ '.

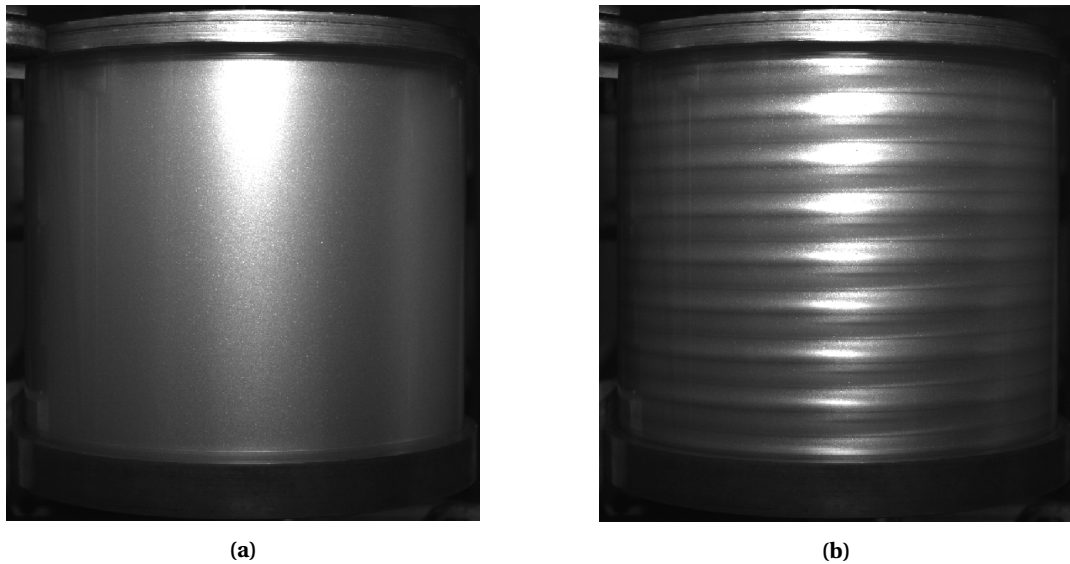


**Figure 1.4:** Transition of the analytically well defined laminar Couette flow to the Taylor vortex flow in the current setup, described by the critical  $\text{Ta}_c$  in Figure 1.3b

### 1.1.2. To wavy vortex flow, and beyond!

When the Reynolds number is increased beyond the appearance of stable Taylor vortices, the flow develops a "waviness"; to the Taylor vortex flow, a wave is superimposed in the azimuthal direction. A comprehensive

study of these wavy vortices can be found in the work of Coles [10]. A snapshot of this regime can be seen in Figure 1.5b. This regime occurs after exceeding the critical Reynolds number by a certain value, which depends on the geometry of the setup. The distinguishing feature of Taylor vortex flow is that it is associated with a critical wave-number  $a_c = kd$ , where  $k$  is the axial wave number of the flow. The beauty of these wavy vortices, as shown by Coles [10] is, its state of non-uniqueness. Depending on the path taken for a particular experiment, he showed that there could be as much as 20 different states at a particular Reynolds number. This implied significant hysteresis, as shown by the state transition map when the outer cylinder is at rest, in Figure 1.5a. Xiao et al. [11] studied the effect of acceleration on wavy vortex flow. They found that even though the wave amplitude was not strongly affected, the wavelengths of wavy vortices and wave speed asymptote to a constant value as a function of acceleration rate.

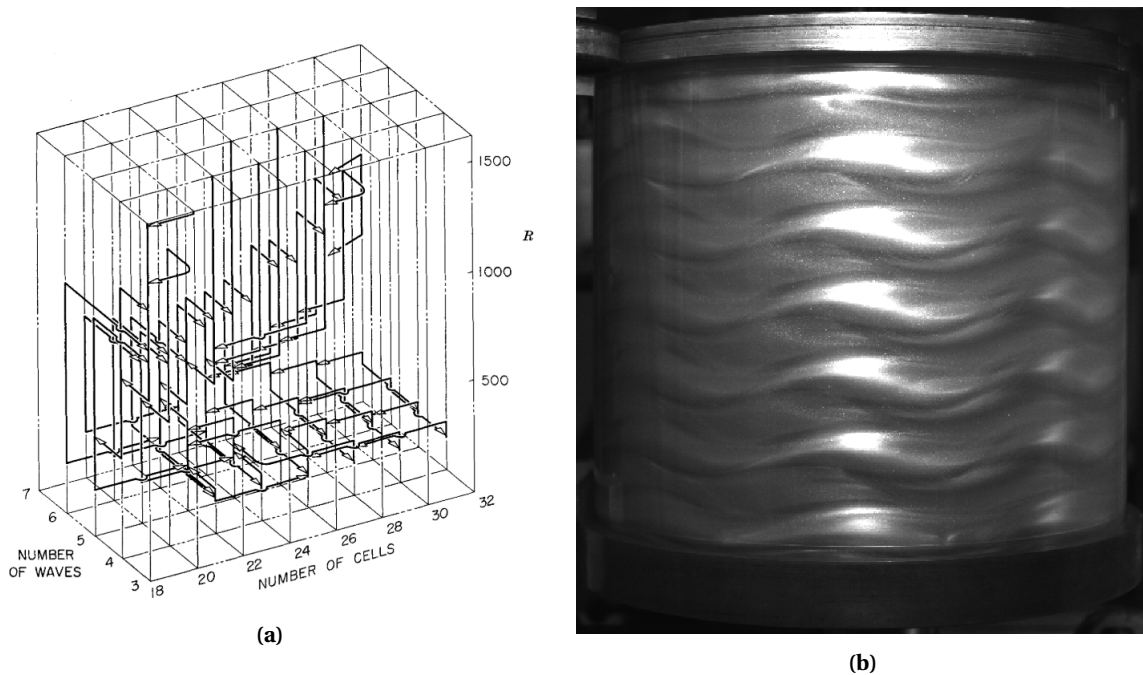


**Figure 1.5:** (a) State transitions for wavy vortex flow, outer cylinder at rest. ( $\eta = 0.847$ ,  $\Gamma = 27.9$ ) For a fixed geometry and fluid patterns, the multiple hysteresis loops are presented here, taken from Coles [12] (b) Wavy vortex flow in the current TC setup, at  $Re_i = 200$

Beyond the wavy vortex flow, the work done by Fenstermacher et al. [13] is very clear in indicating the existence of wavy vortex flow with multiple temporal frequencies. Using laser-Doppler measurements to obtain spectra of the radial velocity component, it was seen that after a certain point, a second sharp component appeared in the spectrum. This signified the appearance of modulated waves, which was studied in detail by Gorman and Swinney [14]. As the laser-Doppler technique is a single point measurement, the spatial character of the flow cannot be captured, so they used an elaborate mirror setup to take snapshots of the TC flow from all viewing angles. This helped in identifying what the second frequency component stood for, and to characterise this modulation. They found the modulation referred to a periodic flattening of the vortex boundaries, as shown in Figure 1.6. The state of these waves was defined by two numbers, 'm' and 'k'. 'm' signifies the number of azimuthal waves and 'k' refers to the nature of the wave flattening. If they all flatten in phase,  $k = 0$ , else  $k \neq 0$ . The modulations for the state 5/0 to 5/2 is shown in Figure 1.6 along with their corresponding spectra. The 5/0 state refers to 5 azimuthal waves in the system with all the waves in phase while the 5/2 state points to the existence of 5 azimuthal waves with the flattening 2 waves apart.

A different type of modulation was also later identified by Zhang et al. [15], wherein the flow had a non-propagating oscillatory mode, which they identified by the change in light intensity. The modulation described by Andereck et al. [16] in their regime map contained a wave in the axial direction drawn by tracing the crests of the waves in each band along the cylinder axis. While it was thought that the existence of mixed-mode states could be attributed to long geometries, the work of King and Swinney [17] shows evidence of these distorted wave patterns that persisted for  $\Gamma \leq 30$ . This also supports the fact that the modulations seen

are not a transient state associated with long geometries.

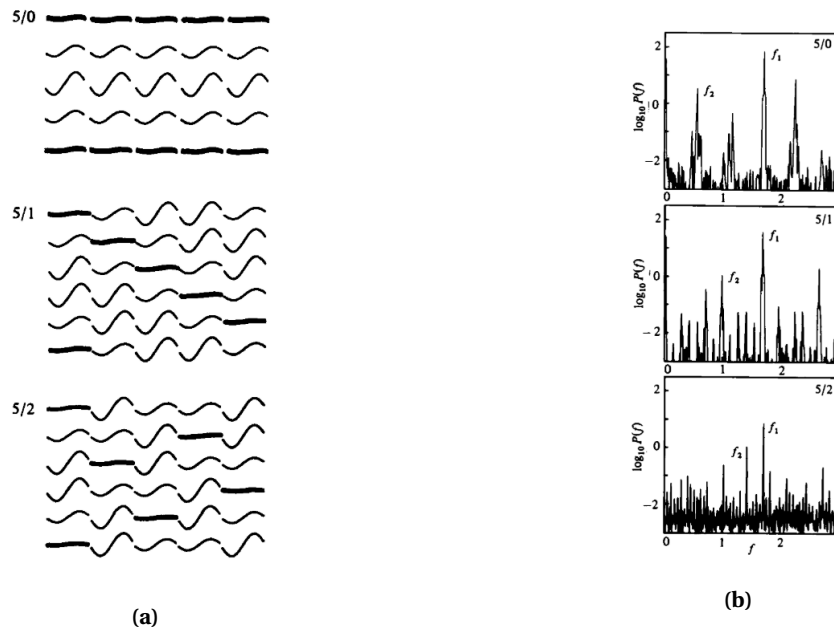


**Figure 1.6:** Modulated wavy vortex flow observed by Gorman and Swinney [14] showing (a) the flattening of the vortex boundaries with the progression of time, which is downwards. The different types of modulations in a five-wave pattern in a reference frame rotating with the waves is represented. (b) The spectra corresponding to the flow states having two distinct peaks, the others being linear integer combinations of the two

Beyond the modulated wave regime, a broad peak is observed in the spectrum, which tends to grow in magnitude. This ‘chaos’ development in the flow was used to classify new regimes such as chaotic wavy vortices and wavy turbulent vortices. Turbulence starts to set in the flow at higher values of Reynolds number wherein the flow starts to lose some of its organisation. This causes turbulent Taylor vortices to persist at higher Reynolds numbers, where only the axial bands remain and each vortex band is filled by turbulence, losing all of the ‘waviness’. Even higher Reynolds numbers cause featureless turbulence, but that is not covered in this literature review. The detailed classification of single-phase flow for pure inner cylinder rotation based on the spectral analysis of light intensity is shown in Figure 1.7. The regimes are defined by Dutcher and Muller [18] based on the number of distinct spatial or temporal frequencies obtained from the power spectrum to get the azimuthal wave frequency and the axial bands of the system. This is used as a basis for comparing the single-phase flows in the current study. For even higher Reynolds numbers and a deeper look into turbulence, a detailed review by Grossman et al. [19] is recommended. They also present an adapted version of Andereck et al.’s [16] flow map, shown in Figure 1.8.

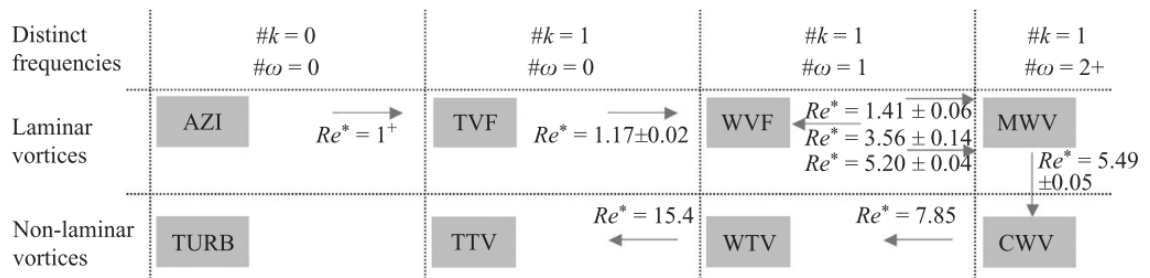


**Figure 1.7:** Transition map for inner cylinder rotation based on distinct spatial ( $\#k$ ) and temporal ( $\#\omega$ ) frequencies of the flow, taken from Dutcher and Muller [18] ( $\eta = 0.912$ ,  $\Gamma = 60.7$ ). New regime names used here are : AZI - Couette flow and TURB - featureless turbulence.

## 1.2. Taylor-Couette flow with two rotating cylinders

Andereck et al. [16] detailed all the different flow regimes observed for multiple cases of inner and outer cylinder rotational rates, shown in Figure 1.8. The detailed flow map covers a wide range of inner and outer cylinder Reynolds numbers. They observed both axisymmetric and non-axisymmetric flow structures, the latter occurring between two axisymmetric flow regimes.

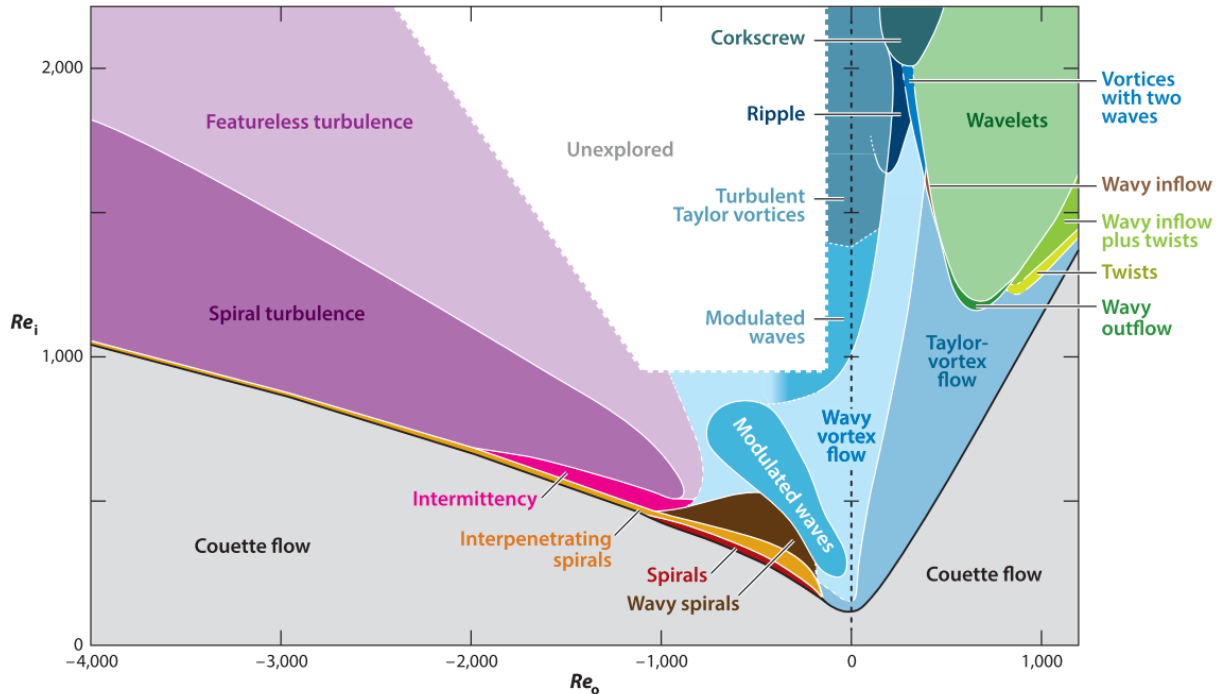


**Figure 1.8:** The Taylor-Couette flow map adapted from [16] by Grossman et al. [19] for a wide range of inner and outer cylinder Reynolds numbers

Flow regimes that were not seen for the case of pure inner cylinder rotation such as spirals and herringbone structures were present for counter-rotating cylinders. They described a region named ‘Transition region’ where multiple flow regimes such as intermittent turbulent spots, wavy interpenetrating spirals and modulated Taylor vortices were competing for stability. They found that even though the spectra of the Interpenetrating-Spiral (IPS) regime indicated an orderly spatial structure, the spectra showed that the regime itself was developing in a non-periodic manner. These interpenetrating spirals are also unstable when waves occur simultaneously in the TC system, thus causing a wavy IPS regime. A snapshot of laminar spirals, both upward and downward moving is shown in Figure 1.10. A study of fluid-particle path in non-axisymmetric TC flow by Ashwin and King [20] details the motion of the fluid particles in a spiral vortex flow, as illustrated in Figure 1.9. Multiple TC single-phase flow studies have extended beyond the range of Reynolds numbers for two rotating cylinders shown in Figure 1.8. This combines numerical and experimental work, summarised in Figure 1.11 taken from Grossman et al. [19].

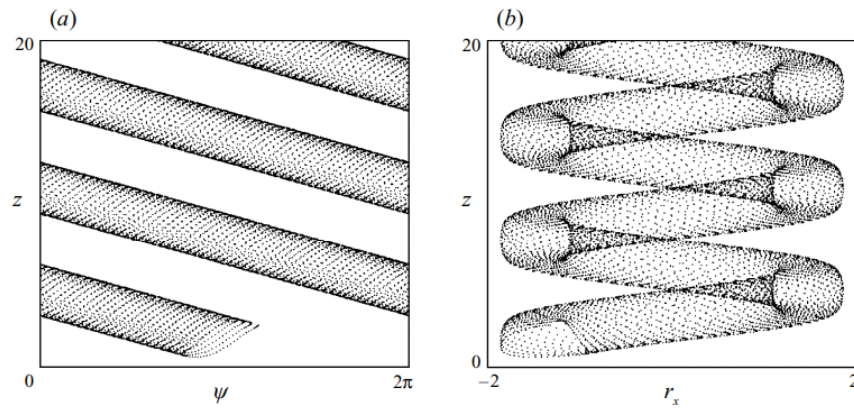


**Figure 1.9:** A single particle trajectory within spiral flow shown in (a) the axial-azimuthal plane and (b) the axial-radial plane, taken from Ashwin and King [20]

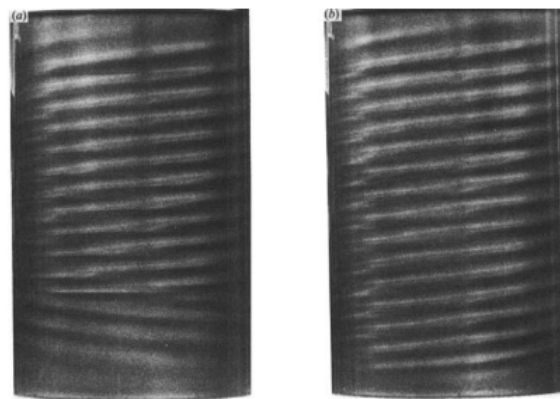


**Figure 1.10:** (a) Separate laminar spirals and (b) single laminar spiral for the condition of counter rotation, as observed by Andereck et al. [16]

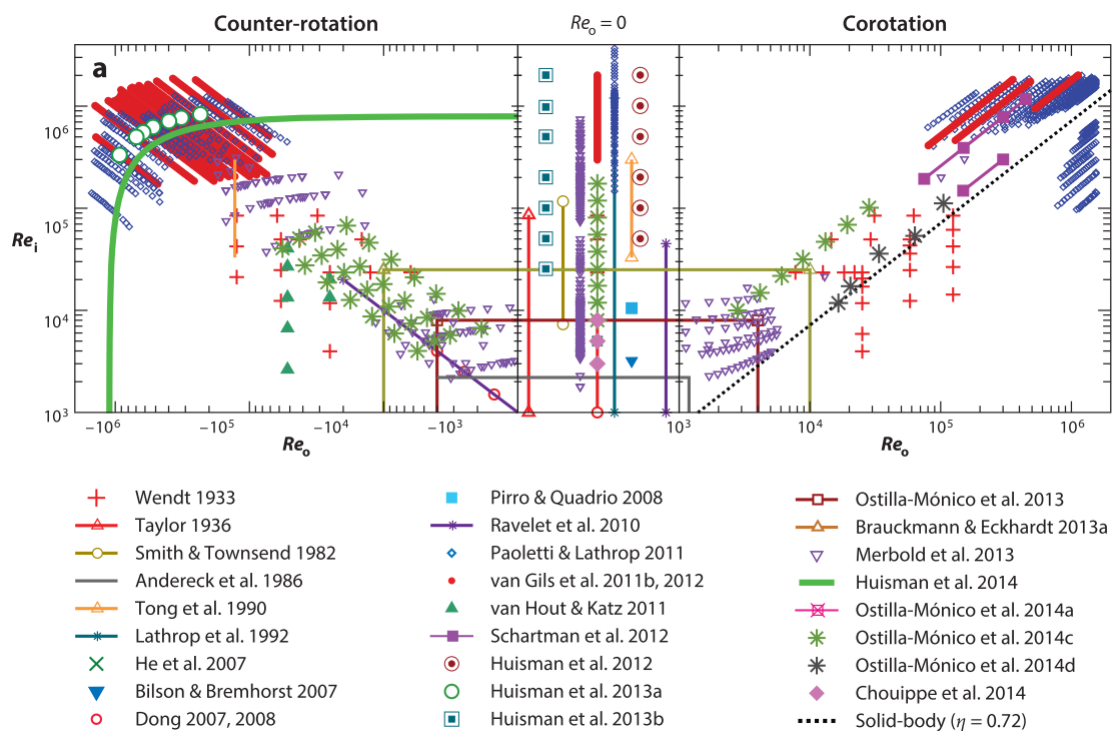


**Figure 1.11:** Explored parameter space based on Reynolds numbers for TC experimental and numerical works. Solid body rotation line for  $\eta = 0.72$  is included. Detailed description of works in this figure is present in Figure 3 of Grossman et al. [19].

### 1.3. Flow visualisation

The flow regimes presented in Figure 1.8 were observed reproducibly by flow visualisation using 2 % by volume Kalliroscope particles in water. This method of visualising the flow was followed in [10, 21, 22]. The basic principle is that these particles align themselves with the streamlines of the flow, thus giving an idea of the flow structures. This is especially useful in a closed system like the Taylor-Couette setup, where detecting the flow structures in all the directions is of primary importance. Mutabazi et al. [23] studied the application of Particle Image Velocimetry (PIV) to the TC flow. Multiple velocimetry techniques such as laser-Doppler [13], ultrasound [24] have been used to extract quantitative information from the TC system. While each technique has its own set of uses, information obtained through visualising flakes was compared to PIV in Mutabazi et al. [23].

Small anisotropic particles can be used to obtain quantitative information from the flow. They align with the streamlines of the flow and Abcha et al. [21] verified that for pure inner cylinder rotation, the flakes gave a sense of the radial component of the velocity, which was in agreement with the numerical simulations of Gauthier et al. [25]. In the work of Gauthier et al. [25], the motion of a tri-axial ellipsoid in general 3-D flows was studied and they found that in TC flow, the particles were not "pasted" on the flow and the observed light was due to reflections from the rotating particles. Abcha et al. [21] mention that the radial component is larger in magnitude than the axial component in pre-turbulent flows, and that the method has not been tested to determine velocity components with the onset of turbulence. They confirm the already existing analysis of Savas [26], who concluded that the flow visualisation flakes are suitable for the determination of quantitative information from the flow. However, they do not recommend using the particles to visualise low amplitude high shear rate flows. Such waves are not studied in this report.

### 1.4. Geometry and initial condition effects

Linear stability analysis of the Taylor-Couette system assumes that the cylindrical columns are of infinite length. The finite length of the systems has effects on the system that can be seen at sub-critical values of the Taylor number. When the Taylor number is increased from the laminar Couette regime, the horizontal end caused circulation results in the formation of a vortex pair close to the end(s), called 'Ekman vortices/cells'. Ekman circulation due to the no-slip condition at the outer cylinder causes a radial motion to penetrate the system in the radial-axial plane as Ekman cells. If the column is sufficiently long, the effect of the horizontal ends is not felt in the middle parts of the system, where the onset of instabilities predicted by stability theory is met. Thus, the infinite column approximation of the stability analysis is met only when the columns are long enough. The mechanism of Taylor vortex formation is shown in Figure 1.12, where the end effects show the development of vortices well before the critical value of transition.

From the work of Alziary and Grillaud [28], the effect of the ends was explained clearly in a numerical study. They also showed that "by using different initial conditions it was possible to obtain, for the same problem, several steady-state solutions differing by the number of cells". From the work of Gul et al. [29] on the current setup, the aspect ratio and setup geometry have a significant role in the hysteresis of the system and they indicated a change in the flow dynamics. An important point to note is that if the aspect ratio of the system is not an even integer value, the vortex formation from either end of the system might match improperly, as observed by Park et al. [30]. Ultimately, the vortices formed are all of the same size, except those at the ends (Koschmeider [8]). In the current experiments, the aspect ratio is 22 and the effects of the ends are absent from the middle section. As summarised by Koschmeider [8], for aspect ratios larger than 10, the onset of instability and super-critical vortices can be described by studies of infinitely long cylinders.

The approximation used in the stability analysis of Taylor [2] was that of a narrow gap, where the gap width would be much smaller than the inner cylinder radius.

$$d = r_o - r_i \ll r_i \text{ or } \eta \rightarrow 1$$

The stability for a wide gap TC system was initially studied by Chandrasekhar [9] for  $\eta = 0.5$ . The value of the critical Taylor number for all radius ratios was determined by Kirchgassner [31]. The critical Taylor number increased with an increase of  $\eta$  (wide gap). Burin [32] aimed to reduce the Ekman circulation (Figure 1.13) in wide gap systems by implementing end rings so that the wide gap flows could have a radial distribution of circumferential velocity that resembled the narrow gap solution.

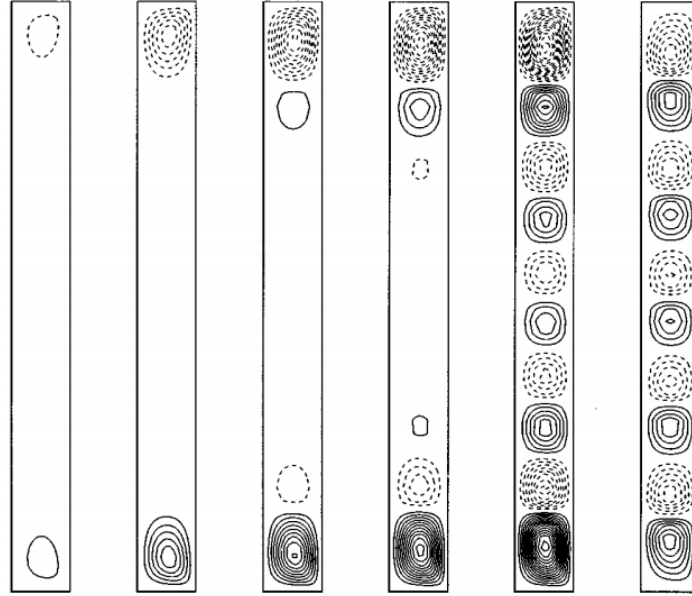


**Figure 1.12:** Development of the isothermal TC flow, taken from Dah-Chyi Kuo et al. [27] ( $\eta = 0.5$ ,  $\Gamma = 10$ ). Reynolds numbers from left to right are 30, 50, 60, 65, 70 and 100. Notice the development of Ekman cells at the ends before the onset of fully Taylor vortex flow.

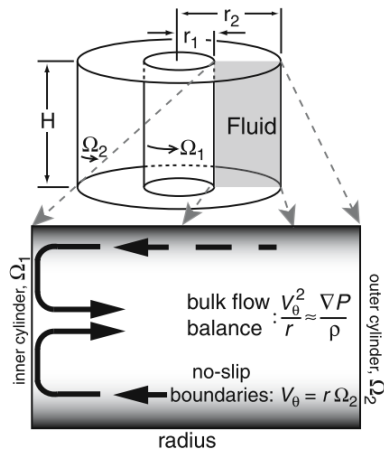


**Figure 1.13:** Schematic showing the end cap boundary inflow that causes Ekman circulation in wide gap TC systems, taken from Burin et al. [32]

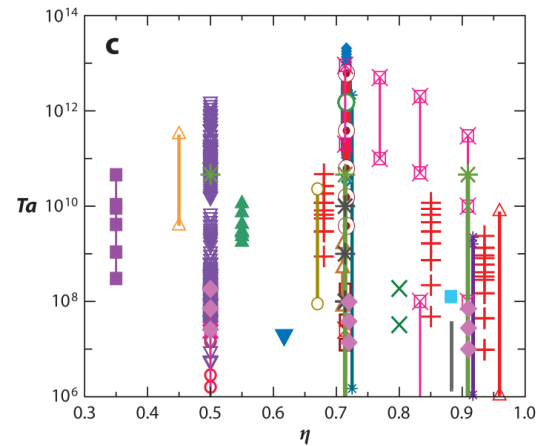


**Figure 1.14:** Classification of TC experiments by the radius ratios and Taylor numbers covered, taken from Grossman et al. [19]. For legend, see Figure 1.11

The radius ratio ( $\eta = 0.917$ ) of the current setup lies in the range of commonly used values in past experiments, as seen from the works of Tokgoz [33] and Grossman et al. [19]. The various experiments performed across different radius ratios are shown in Figure 1.14 with the corresponding Taylor number ranges covered. Studies by Ostilla et al. [34, 35] catalogued the dependence of the turbulent TC flow on  $\eta$ . They found that the radius ratio had a significant role in optimal angular velocity transport. For smaller gaps, (larger  $\eta$ ), the optimal transport of angular velocity was found to be more efficient and an increase in the value of bulk velocity was observed with an increase in  $\eta$ . The results they obtained were in line with those obtained by Ostilla et al. [35] for narrow gaps. However, they leave the question of larger gaps TC flows open for further investigation.

## 1.5. Particle-laden suspension studies

The attention of flow physicists turned to multiphase flow within the already complex Taylor-Couette problem. Before that, the phenomenon of particles migration in suspensions was observed in pipe flow by Segre and Silberberg [36]. They found that in Poiseuille pipe flow, the particles migrated to an equilibrium radial position at  $r = 0.6R$ ,  $R$  being the pipe radius. This position is midway for simple shear flows and both these were confirmed theoretically by Ho and Leal [37]. They determined that the migration was caused by the non-linear inertial terms in the Navier-Stokes equations that contributed to a lateral force (induced by sphere surface stresses). This was extended to the Taylor-Couette system and the results of Halow and Wills [38] showed that the particles migrated to an equilibrium position around the midpoint of the annular gap. The study of Segre and Silberberg [36] was extended by Matas et al. [39] where they studied the effect of inertial migration on the transition to turbulence for different particle loadings. They found that their results agreed with Segre and Silberberg [36] and also the predictions of asymptotic theory (Ho and Leal [37]) but found deviations for larger particle sizes. They associate this to the size of the particles as the condition for the particle Reynolds number ( $Re_p \ll 1$ , calculated based on the effective suspension viscosity) was not met. The sub-critical transitions observed by them was attributed to fluctuations triggered by the particles. The particle loading was also kept low such that particle-particle interactions would not be a factor. An example of the "Segre-Silberberg annulus" from Matas et al. [39] is shown in Figure 1.15.

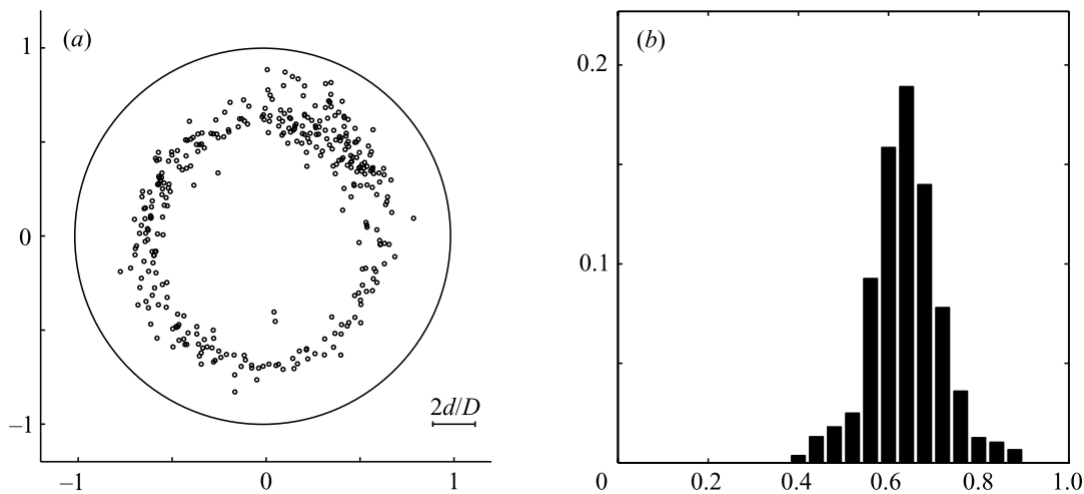


**Figure 1.15:** Particle distribution in pipe flows (a) over a cross section (b) shown as the histogram of the probability distribution function for  $Re = 67$  and  $d/D = 9$

## 1.6. Taylor-Couette flow with particles

As the Taylor-Couette system has proven to be an ideal testing ground for understanding transition phenomena, particle effects on transition piqued the interest of fluid physicists. An analytical study by Ali [40] predicted that for dilute suspensions, the addition of particles caused the destabilisation of the circular Couette flow for a non-Brownian suspension. Experiments by Dherbecourt et al. [41] showed that regardless of flow regime, the addition of particles ( $\phi \leq 0.08$ ) significantly enhanced mixing in Taylor-Couette flow. A particle migration study by Majji and Morris [42] detailed the effect of particle migration in Couette flow and Taylor Vortex flow. They found that in Couette flow, the migration to an equilibrium position near the middle of the annulus was due to the competing flow shear gradient and wall interactions (Figure 1.16). For TVF, the additional vortex motion caused the particles to move to circular equilibrium regions in each vortex, shown in Figure 1.17.

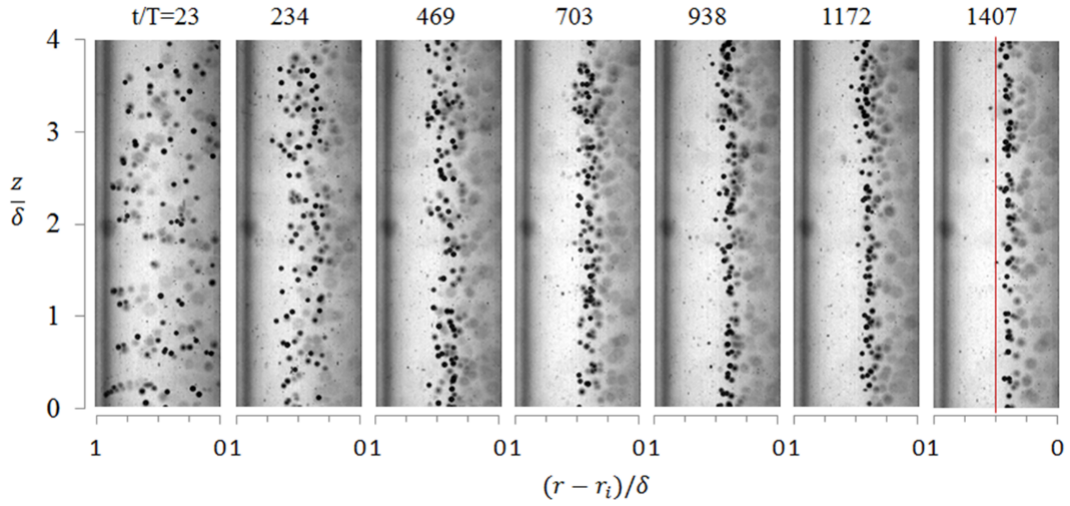


**Figure 1.16:** Particle migration in TC flow at  $Re = 83$  in the  $r$ - $z$  plane for  $\eta = 0.877$ ,  $\Gamma = 20.5$ ,  $\delta = d$ , from Majji and Morris [42]. Out-of-plane particles are seen as lighter blurred spots.

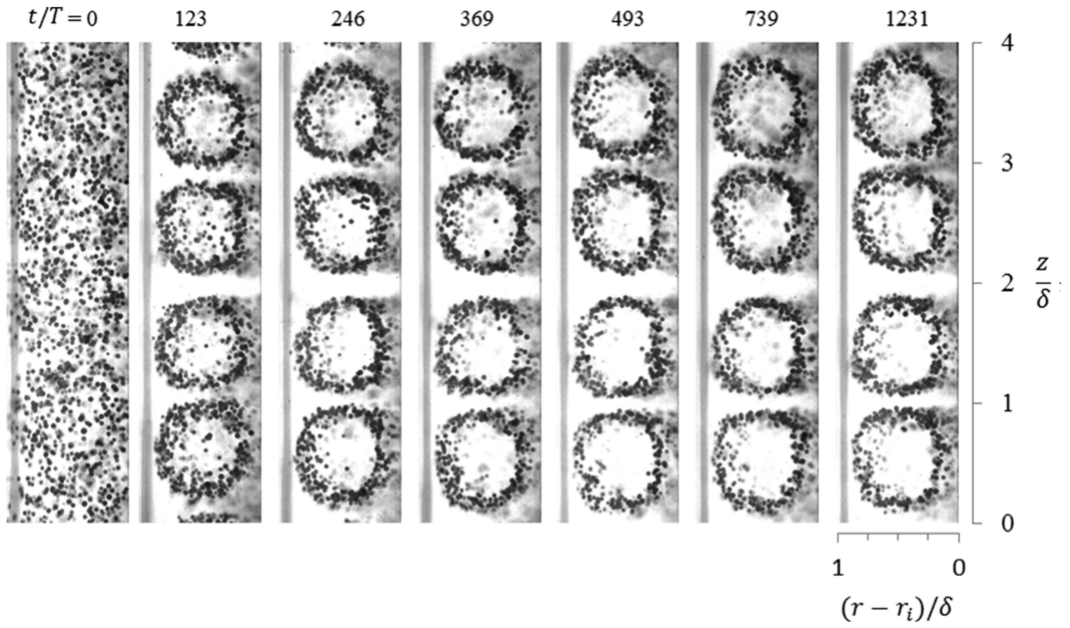


**Figure 1.17:** Particle migration in TVF at  $Re = 145$  in the  $r$ - $z$  plane for  $\eta = 0.877$ ,  $\Gamma = 20.5$ ,  $\delta = d$ , from Majji and Morris [42].

The effect of particle loading on the flow transitions of a TC system was characterised by Majji et al. [43]. For a stationary outer cylinder and a rotating inner cylinder, they studied the effects of non-Brownian particle loading (two different sizes) on a density matched suspension. The primary effect they found is the destabilising effect on the circular Couette flow with the onset of earlier transition. They also observed several non-axisymmetric flow states not seen in single-phase flow with pure inner cylinder rotation. The flow states were characterised by visualisation aided by the use of space-time plots of the reflected light intensities. The reduction in critical Reynolds number due to the effect of increased particle size for the transition from Couette flow is shown in Figure 1.18.

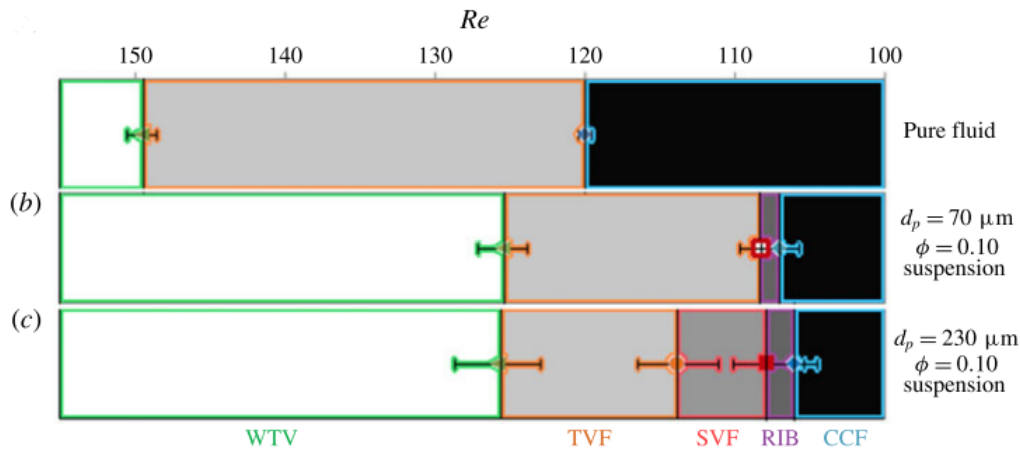


**Figure 1.18:** Transition map comparing single phase flow (top) with the cases of increasing particle diameter but same particle loading. The onset of the first transition (from right) is quicker when particles are present.

In addition to the earlier transition from Couette flow, they also notice the emergence of several non-axisymmetric structures, not observed for a stationary outer cylinder in single-phase flows. These states have been observed by Andereck et al. [16] for counter-rotating cylinders, but not for  $Re_0 = 0$ . Some of the states observed were spirals, ribbons and wavy spiral vortices. The space-time plots of these spirals and ribbons are shown in Figure 1.19. They also conducted a stability analysis of the spirals and postulated that the ribbon structures were formed as a result of the merging two oppositely inclined spirals, also shown in Figure 1.20.

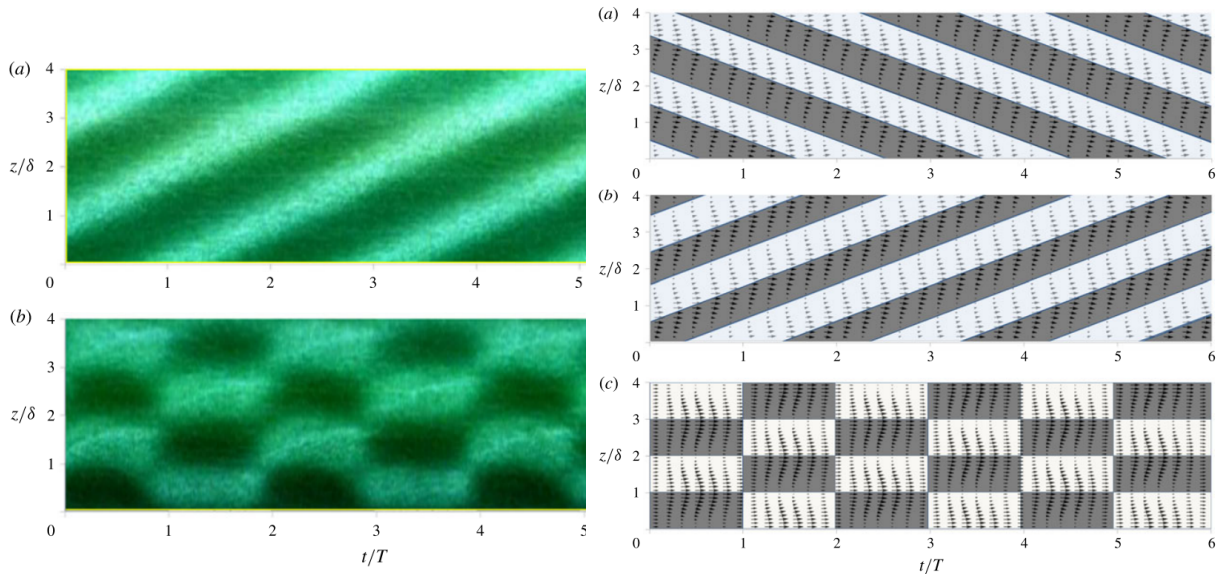


**Figure 1.19:** Space-Time plots of (a) spiral vortex flow ( $Re = 106.7$ ) and (b) ribbons ( $Re = 106.6$ ) for  $\phi = 0.10$  and particles of size 230 microns. The time scale  $T$  is for one full rotation of the inner cylinder, from Majji et al. [43].

**Figure 1.20:** Space-time diagrams of (a) L-spirals (b) R-spirals (c) ribbons constructed from velocity fields using linear stability analysis for pure inner cylinder rotation. The R-spiral and ribbon plots are the same as those shown in Figure 1.19, taken from Majji et al. [43].

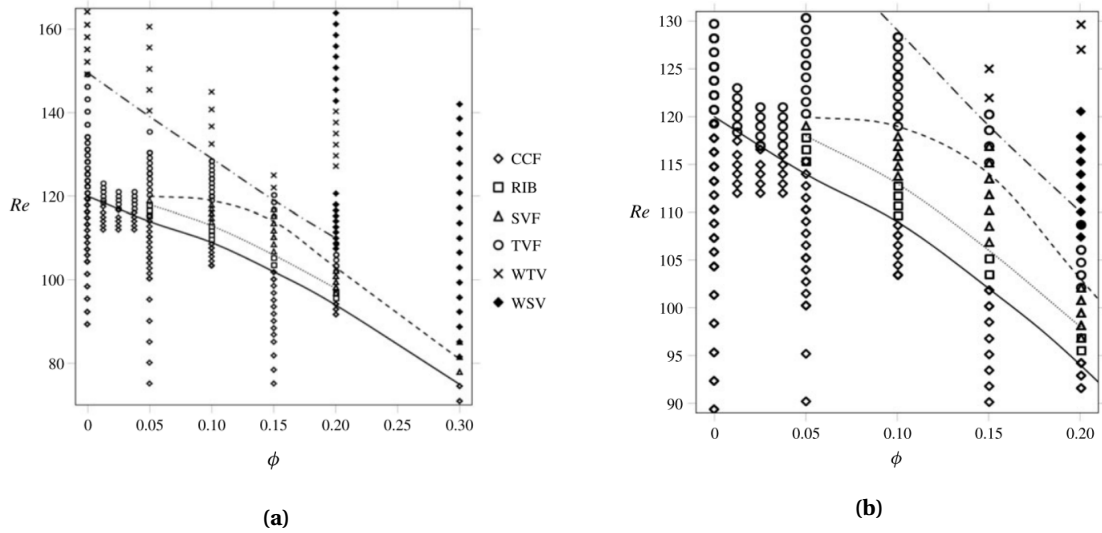


**Figure 1.21:** (a) Flow map for all the observed transitions in the experiments of Majji et al. [43] (b) Close up of (a) to show the non-axisymmetric structures clearly.

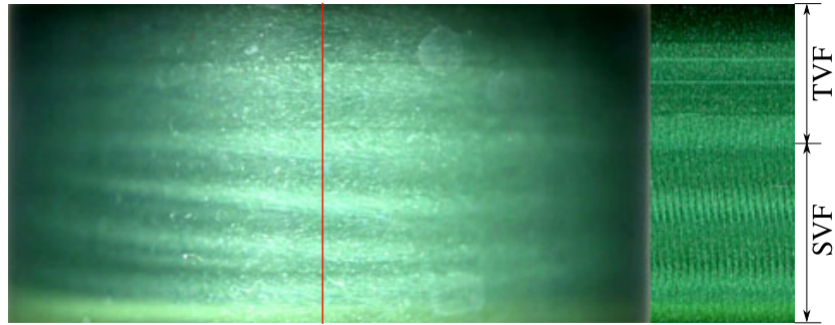


**Figure 1.22:** Coexisting Taylor vortex flow (top half of snapshot) and spiral vortex flow (lower half of the cylinder) with the corresponding space-time diagram for  $Re=117$ ,  $\phi = 0.20$ , from Ramesh et al. [44]

A consolidated flow map for the transitions up to a particle volume fraction of 30% is shown in Figure 1.21. Several non-axisymmetric states were observed for their geometry ( $\Gamma = 20.5$ ,  $\eta = 0.877$ ) and their appearance indicates a qualitative alteration of the system by the particles. A recent study by Ramesh et al. [44] set out to validate and extend the work of Majji et al. [43] by trying to answer how the particles influenced the mean azimuthal velocity and fluctuation kinetic energy. They also arrived at a flow-map similar to Figure 1.18, and found good agreement qualitatively with the experiments of Majji et al. [43]. However, they do not observe ribbon structures, and they attribute their absence of the effect of a smaller aspect ratio ( $\Gamma = 11$ ,  $\eta = 0.914$ ). They also observe coexisting states where two regimes coexist, as shown in Figure 1.22 where the Taylor vortices are present along with spirals. From the refractive-index-matched PIV measurements, they also remarked that the nature of suspension Taylor vortices was structurally different from those in a Newtonian fluid of the same effective viscosity.

## 1.7. Research goals

The two studies that have investigated the effect of particle loading [43, 44] in suspension Taylor-Couette flow have obtained qualitatively similar results but have different flow transitions. Due to the varying nature and order of flow regimes with the addition of particles, it is imperative to study the system with the current experimental setup and characterise the flow behaviour. Both the studies mentioned have covered a small range of Reynolds numbers ( $Re_i < 200$ ) to observe the non-axisymmetric structures in detail, leaving the question of flow transitions at higher Reynolds numbers unanswered. The main research goal of the current project is:

**"What is the effect of particle loading on the flow transitions of a Taylor-Couette system for a wide range ( $0 \leq Re_i \leq 2700$ ) of Reynolds numbers?"**

To answer the main research question, the following sub-questions are also set:

- Can the single-phase flow transitions be classified based on flow visualisation?
- What effect do the particles have on the primary transition from Couette flow and at higher Reynolds numbers?
- If non-axisymmetric structures are observed, how does their appearance vary with volume fraction?

Practical restrictions on the current Taylor-Couette setup limited the experiments performed to a single particle size and type ( $d_p = 619\mu m$ , PMMA), a narrow-gap and fairly large aspect ratio geometrical configuration ( $\eta = 0.917$ ,  $\Gamma = 20.2$ ) with only one rotational condition ( $Re_o = 0$ ).

## 1.8. Organisation of the report

The report are organised as follows:

- Chapter 2 contains the details of the experimental setup that is used and the experimental procedure for both single and multi-phase flows.
- Chapter 3 is can be divided into two halves: the first half details the data processing techniques used to characterise the observed flow phenomena. The latter half contains the characterisation of flow regimes and validation of the current experiments with previous works in single-phase flow. A flow transition map is constructed and the regime changes are analysed in detail.
- Chapter 4 contains the results of the particle-laden suspension studies and also incorporates the discussion on the nature of flow transitions. The new regimes that appear due to the addition of particles are characterised based on flow visualisation. A flow map is constructed for  $0 \leq \phi \leq 0.40$  and the case of  $\phi = 0.10$  is analysed extensively for all the shifts between regimes.
- Chapter 5 summarises the main outcomes of the analysis along with recommendations for future work.



# 2

## Experimental setup

The extensively studied Taylor-Couette (TC) setup at the Lab for Aero and Hydrodynamics, TU Delft [29, 33, 45] was utilised for the current experiments. The system consists of two coaxial, independently rotating cylinders where the fluid is present in the annulus between the inner and outer cylinders. The schematic of the experimental setup is presented in Figure 2.1.

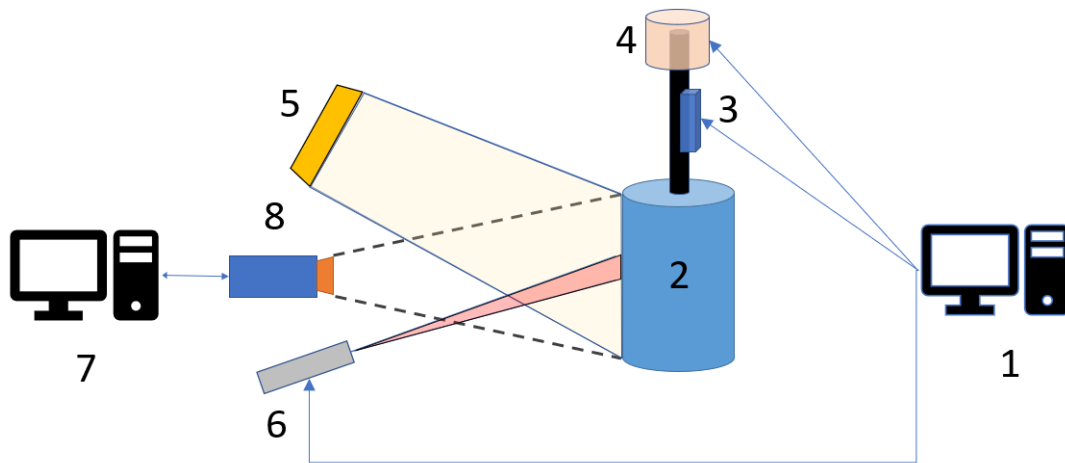


**Figure 2.1:** Schematic overview of the experimental setup: 1. Computer interfaced to a DAQ, controlling the motor, temperature sensor, cylinder rotation and torque sensor. 2. TC cell 3. Torque sensor 4. Motor controlling inner cylinder rotation 5. LED light 6. IR temperature sensor 7. Computer interfaced with a frame grabber and PTU controlling the camera 8. Camera

The entire setup is controlled by two computers. The computer labelled 1 in Figure 2.1 controls the cylinder rotation through a motor driving unit. It also controls the data acquisition (DAQ) of the torque and temperature sensors. The second computer (labelled 2 in Figure 2.1) controls the visualisation part of the experiment. It houses a frame grabber and is interfaced with the camera through a Programmable Timing Unit (PTU). Each part of the setup is explained in the following sections.

### 2.1. Geometry of the TC cell

The inner and outer cylinders are made of Perspex and the upper cylinder cover is made of aluminium, with a drilled hole for filling and emptying the system. To fill the system with fluid or with a particle-laden suspension, a peristaltic pump is used to transfer the viscous solution from the prepared stock to the cylinder and the same is done for emptying it also. The outer cylinder base is made of brass and the inner cylinder is painted black on the inside for better visualisation. The disassembled inner and outer cylinder can be seen in Figure Figure 2.3. A schematic is shown in Figure 2.2 with the relevant geometrical parameters' nomenclature.

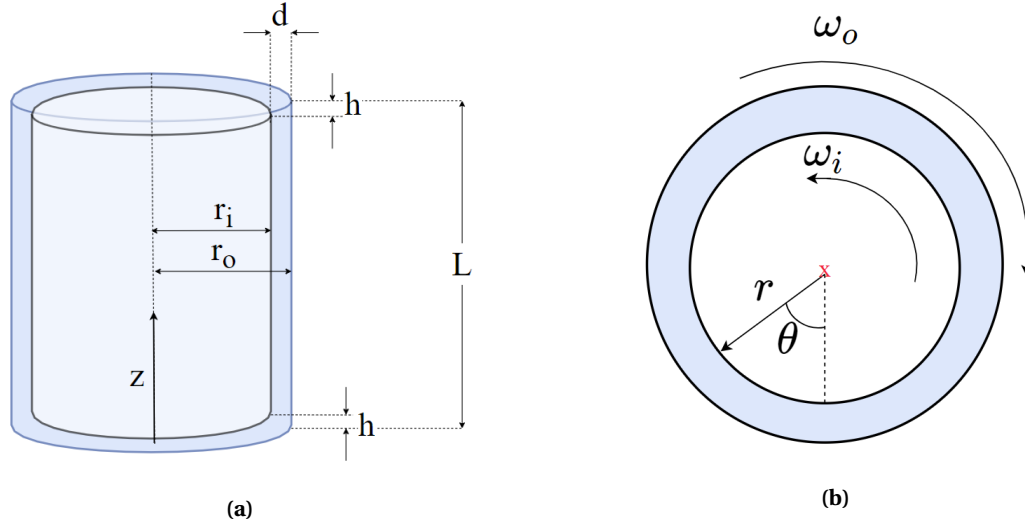


**Figure 2.2:** (a) Front view of the TC system with the fluid in the region shaded blue (b) Top view of the TC cell with the working fluid (shaded blue) and the axis (red cross) indicated. The coordinate system is represented by the labels  $r$ ,  $\theta$  and  $z$ .

When the system is filled with the working fluid, there are gaps between the cylinders at the top and bottom. These are assumed to be equally distributed, the gap width being 2 mm at the top and bottom. The important dimensions of the setup are presented in Table 2.1. In all the experiments discussed in this thesis, the outer cylinder is held stationary and the inner cylinder is rotated at an angular rate of  $\Omega_i$ , based on an input rotational frequency from the motor,  $f_i$ .

The annular gap width is the difference in the radii between the cylinders ( $d$ ), and here it is 10 mm. The gap between the top of the inner and outer cylinder (assumed to be the same at the bottom) is called as the von-Karman (v-K) gap, which is 2 mm for all the experiments and denoted by 'h'.

**Table 2.1:** Parameters of the TC setup and their corresponding values

Parameter	Symbol	Value
Inner cylinder radius	$r_i$	110 mm
Outer cylinder radius	$r_o$	120 mm
Outer cylinder length	$L$	220 mm
Inner cylinder length	$L_i$	217.6 mm
von-Karman gap	h	2 mm
Radius ratio	$\eta = r_i/r_o$	0.917 [-]
Aspect ratio	$\Gamma = L/d$	22 [-]



**Figure 2.3:** Outer (left) and the inner cylinder (right) after the setup has been dismantled.

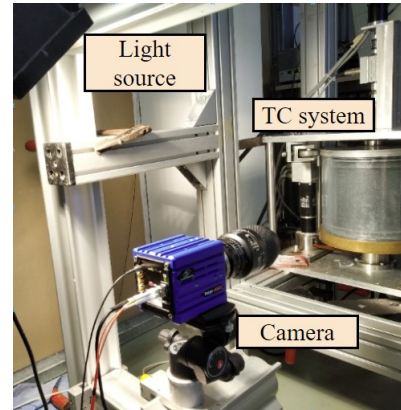


**Figure 2.4:** Camera and lights directed at the TC system.

## 2.2. Measurement devices

### 2.2.1. Imaging optics

The primary method of studying the flow physics in this thesis is by visualising the flow structures through simple imaging. This was achieved using a Lavision Imager sCMOS 16-bit camera with both full sensor size and a cropped Field Of View (FOV) to accommodate higher frame rates. The full FOV has a window size of 2160 pixels  $\times$  2560 pixels with a pixel size of  $6.5 \times 6.5 \mu\text{m}^2$ . For all the experiments, a 50 fps full FOV still image and cropped images at 100 fps were recorded. A Nikon 35 mm lens ( $f_{\#} = 4$ ) was used and the camera calibration and focussing were performed on the outer cylinder surface. The FOV is a rectangular window along the axis of the cylinder, covering an area of  $28.1 \times 23.7 \text{ cm}^2$ , as seen in Figure 2.5. The resolution in the axial direction is 9 pixels/mm.

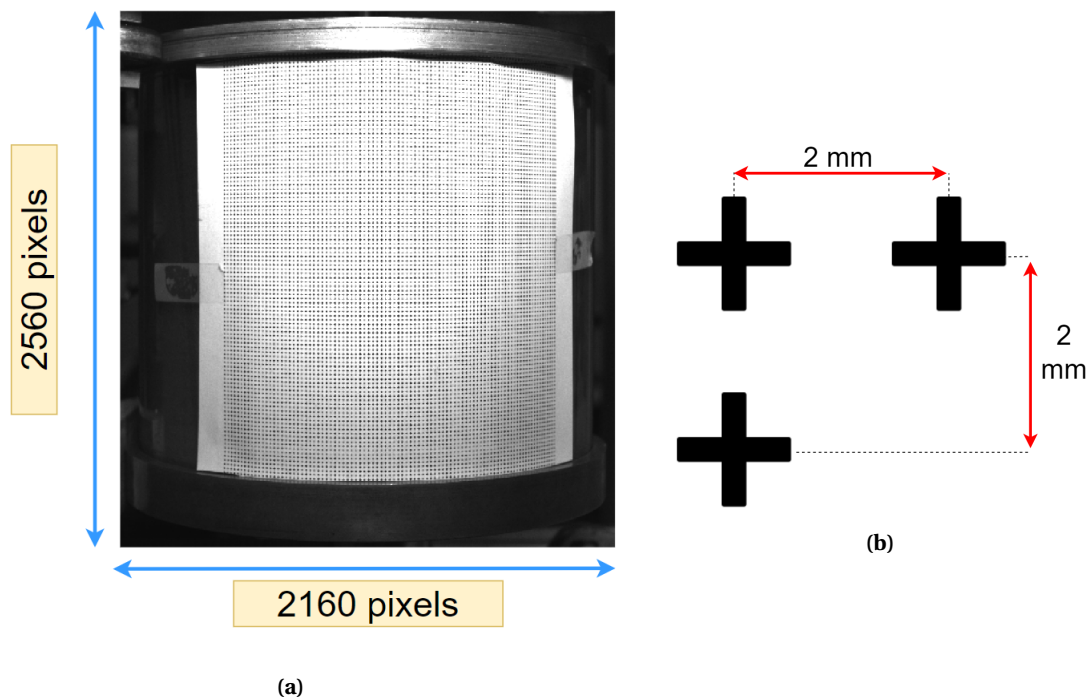


**Figure 2.5:** (a) Calibration grid pasted on the outer cylinder surface (b) Grid spacing used in the calibration

A printed grid pasted on the outer cylinder was used to resolve distances primarily in the axial direction through a scaling factor. The grid consists of plus signs 2 mm apart in the horizontal and vertical directions.

The mounted camera after calibration is shown in Figure 2.4 and the corresponding calibration grid positioned for imaging is shown in Figure 2.5. The FOV contains a curved surface in the form of the outer cylinder surface and so the centre line of the image is aligned with the axis of the cylinder. This is done to avoid the effect of cylinder curvature and the processing of the data obtained from the centre line of the image is explained in chapter 3. The exposure of the lens was 1500  $\mu s$  for all the experiments. The camera had a firmware defect that caused artefacts to dominate the captured images for lower exposure times than 1500  $\mu s$ , thus limiting the lowest value of exposure time that could be set even with sufficient lighting.

To image the TC cell, a powerful LED panel was mounted above the camera at an oblique angle. The reason for an oblique angle of illumination is that the direct illumination causes too many reflections and the best compromise between proper illumination and least reflections on the cylinder surface was to angle the light source from above. This is similar to the illumination followed by Majji et al.[43]. The inner cylinder was painted black on the inner surface to further improve the image quality and the TC cell was shielded to avoid reflections.

### 2.2.2. Temperature

TC setups with highly accurate temperature control have a water/oil bath surrounding the TC cell that maintains the temperature throughout the experiment by taking away the heat at a controlled rate [16, 18, 43, 46]. This is ideal, but the implementation necessitates modifications to the setup that are not pragmatic in the current TC system. In the work of Tokgoz [33] and Gul et al. [29] on the same setup, the experiments were kept short and/or the temperature differences between the experimental runs were only around 0.5°C. However, the current experiments had many cases where temperature difference between the start and end of an experimental run was as high as 7°C. This results in a significant variation of the fluid Reynolds number due to a change in the fluid properties associated with the temperature change, as shown in Table 2.2. The percentage changes in Reynolds numbers are reported in Table 2.2 for steps of 5°C.

**Table 2.2:** Viscosity and Reynolds number dependence on temperature for a fixed rotational speed of 1 Hz

Temperature [°C]	Viscosity [ $m^2s^{-1}$ ]	Reynolds number [-]	Reynolds number change [%]
20	2.41e-5	287	-
25	1.87e-5	367	27.87
30	1.47e-5	470	28.07

The temperature of the fluid is measured before and after each experimental test using a PT100 sensor. This was calibrated with a bath of ice water and boiling water along with other pre-calibrated temperature sensors to get a calibration curve. The basis of this project is flow transitions and for their classification the Reynolds number at which the transition occurs must be known at least to some degree of accuracy. This means that the fluid temperature has to be known throughout the experiments, not only at the beginning and end. To obtain the fluid temperature as a function of time, a ‘Calex Pyropen’ Infra-Red (IR) sensor was used. This measured the temperature of outer cylinder wall, set to an emissivity of 0.86 to match the material of the outer cylinder wall. The IR temperature as a function of time was used to get the continuous fluid temperature based on the PT100 initial and final values, as shown in Figure 2.6

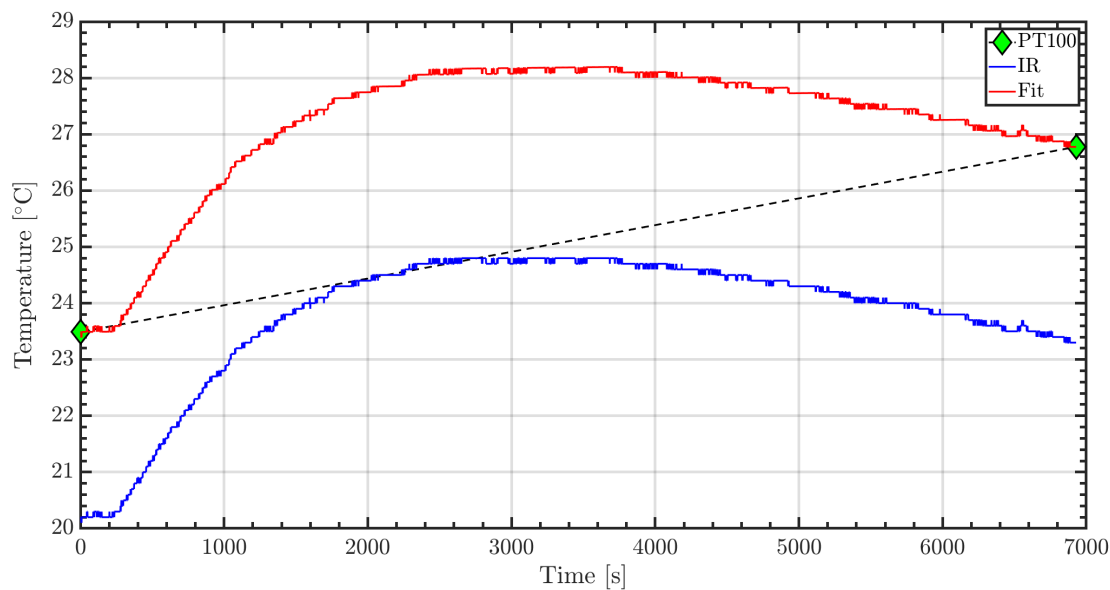


**Figure 2.6:** Estimated fluid temperature as a function of time based on the wall temperature (IR), based on which the instantaneous viscosity and Reynolds number are obtained.

### 2.2.3. Torque measurement and rotation control

The torque sensor (HBM T20WN, 2 Nm) is coupled to the shaft of the inner cylinder and gives instantaneous torque readings in Volts as a function of time, sampled at 2000 Hz. The torque readings are calibrated with an offset based on a linear fit of the laminar regime torque curve, as followed by Greidanus et al. [45, 47], the procedure for which is shown in section A.1. The sensor has a least count of 0.01 Nm and readings below 0.05 Nm are considered less reliable.

The torque sensor measures the torque along the whole length of the inner cylinder shaft, and so the contribution of the v-K gaps (von-Karman) were accounted for. From the detailed studies of [45, 47], the v-K contribution of the ends in the current setup is approximately 50% for the range of Reynolds numbers of interest. This is taken as a starting value and in subsection 3.1.4 and the exact v-K contribution for the present setup is calculated based on the torque values.

The inner and outer cylinders are independently connected to motors (Maxon model 249028) and the rotational input for the cylinder is given as a frequency, either manually or through a MATLAB script. For the current experiments, the outer cylinder is held stationary and the instantaneous values such as cylinder rotational speed and torque are obtained by interfacing the sensors with a Data Acquisition system (DAQ). The input programs to control the whole TC cell were pre-programmed employing LABView. The rotational input given to the system differs from the actual rotational frequency of the cylinders. The actual frequency of rotation is obtained with the help of a TTL pulse counter. This gives a fixed number of pulses for one rotation of the cylinder and this true frequency is used to calculate the Reynolds number of the TC cell, the procedure for which is explained in section A.2.

## 2.3. Suspension and particles

### 2.3.1. Working fluid and flow visualisation

To obtain a wide range of Reynolds numbers covering the major transitions of flow regimes for only the rotation of the inner cylinder, a water-glycerol mixture was used. The choice of the working fluid to cover transitions was closely associated with the choice of the particles. This is because the neutrally buoyant suspension density is the density of the corresponding working fluid for single-phase flows, to provide a common basis for comparison. A water glycerol mixture containing 67.6% of glycerol by volume was prepared from filtered water and 'Glycerol s.g. 1.23' from BOOM. The method used to arrive at the proportion of 67.6% by volume for the working fluid can be found in subsection 2.3.3.

The glycerol-water mixture is transparent and since the measurement technique was primarily optical, pearlescent pigment particles were also added. In TC experimental setups, anisotropic particles are added to visualise single-phase flow because they align themselves with the streamlines and give a good representation of the flow without affecting it when added in correct quantities. The most common particles used for visualisation are Kalliroscope flakes [16, 21, 46], but the worldwide production of these particles came to a halt in 2014 [48]. The properties of these particles and their effect on the TC flow were characterised by Dominguez-Lerma et al. [22]. These particles tend to affect the Taylor Vortex Flow (TVF) regime by introducing a non uniformity in the vortex widths. They attribute it to a concentration gradient of these particles in the axial direction, but this should not be a factor affecting the flow in the current set of experiments. This is because the current setup has a much smaller aspect ratio comparatively (22 compared to 71) and so the particles are added in very low concentrations (0.1 % compared to 0.3 %) and more importantly, there was no non-uniformity observed in the width of the Taylor vortices in the axial direction. For the current experiments, 'Iridin silver pearl 100' (Titanium dioxide coated mica platelets) particles were added and they have been used previously in the Taylor Couette experiments of [49–53]. These particles have a specified size of 10-60  $\mu\text{m}$  and a density of 2.8-3.0 g/cc. Stearic acid crystals were also tried out based on the work of Daniel Borrero-Echeverry et al. [48], albeit unsuccessfully and the detailed explanation is presented in Appendix C. To avoid the effect of these particles on the flow, they were added in proportions of 0.1% by mass of the solution in line with the above references. This is a conservative choice but was implemented as the visualisation was more than adequate even with this concentration of particles.

### 2.3.2. Particle properties and size distribution

The particles used were 'PMMA powder - Acrylic, Injection moulding grade' obtained from GoodFellow with a specified maximum particle size of 600 microns and density of 1.19 g/cc. These particles were specifically chosen mainly due to the range of Reynolds numbers that could be covered with their corresponding neutrally buoyant suspension. A large number of particles were close to 600 microns and so the entire batch of particles was sieved to first have a rough distribution of size between 560 and 600 microns. To estimate the distribution of the particle sizes in the sieved batch, they were analysed using a microscope. The calibration was performed by using a grid to obtain a scaling factor to get a pixel to mm conversion of 6.57 pixels/mm.

The particles are not opaque and so the particle sizes could not be found straightforwardly from Matlab, rather it had to be done manually by identifying particles. Another reason for doing this is because many particles are not spherical and this leads to improper identification of particles in the images. For the non-spherical particles, the major axis (in the case of an ellipse) is taken as its 'diameter' and that is why in the size distribution of particles, particles almost twice as large as the mean particle diameter exist. An image taken in the microscope is shown in Figure 2.7a and the used calibration grid is shown in Figure 2.7b.

As the light passes through a lens system, the diffraction spot error is present, causing an airy disk around a particle, leading to an overestimation in its size. This diffraction-limited spot diameter and related formulae to calculate actual particle size are given in [54, 55]:

$$d_{\text{diff}} = 2.44 f_{\#} (M + 1) \lambda$$

$$f_{\#} = 1 / (2 \cdot \text{NA}) = 12.5$$

where  $f_{\#}$  is the f-number of the lens (Nikon Objective M x 1.0/0.04),  $\lambda$  is the wavelength of the illuminating light source (white light), NA is the Numerical Aperture of the lens (NA = 0.04) and M is the magnification of the lens used (M = 1). As white light was used, an average wavelength of 545 nm was chosen, for which the diffraction-limited spot diameter is 33.24  $\mu\text{m}$ . This is still within the acceptable error of particle size as there

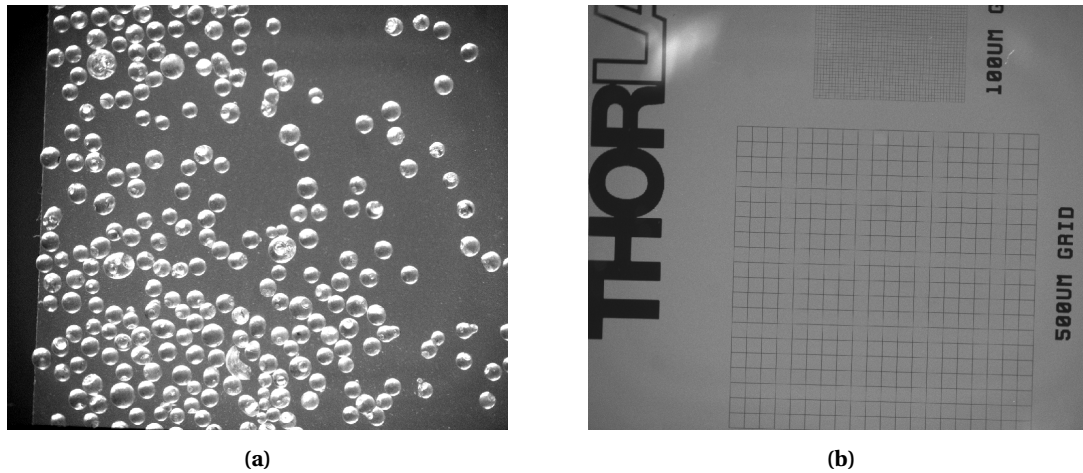


**Figure 2.7:** (a) Raw microscope images of PMMA particles (b) Calibration grid from Thorlabs used to get a scaling factor.

is a wide distribution of sizes in the samples tested. The overestimated diameter of the particle ( $d_t$ ) observed from the images is given by:

$$d_t = \sqrt{(Md_p)^2 + d_{\text{diff}}^2}$$

from which the particle's actual size ( $Md_p$ ) is estimated. The mean particle diameter obtained from this for 675 samples after the correction was  $619 \mu\text{m}$ . The distribution of the particle size is presented in Figure 2.8 utilising probability and cumulative density functions. A Kernel fit is used in Figure 2.8a to fit a curve over the histogram of particle size distribution and this is used to get the probability values.

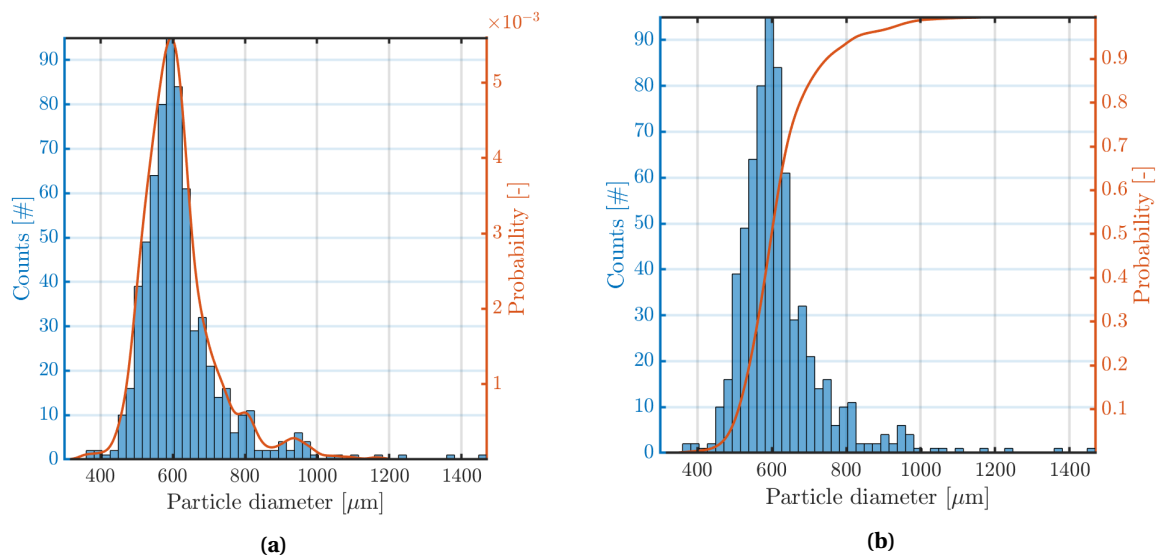


**Figure 2.8:** (a) Probability Density Function (PDF) and (b) Cumulative Density function (CDF) of the particle size with the Counts (samples) on the left y-axis and the probability on the right y-axis as a function of the particle diameter (x-axis). A Kernel fit is used over the diameter data in (a), presented in the form of a histogram in both (a) and (b).

The number of samples required for the convergence of particle diameters was determined by using the Full Width Half Maximum (FWHM) as well as the mean particle diameter values, both non dimensionalised and plotted as a function of the sample number in Figure 2.9. The FWHM is obtained by calculating the width of the distribution curve at the points where it is 50% of its peak value. The y-axis contains the normalised

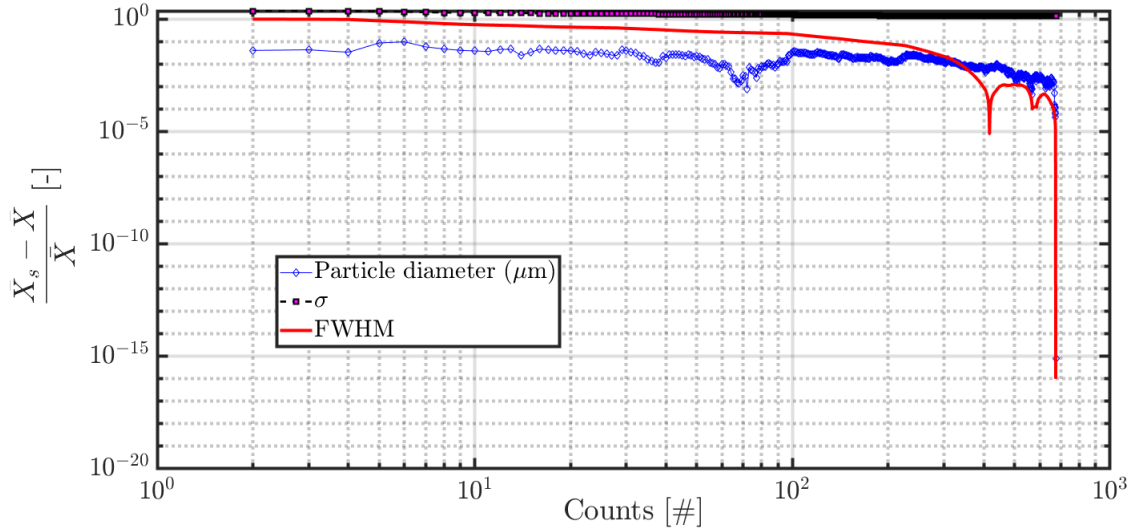


**Figure 2.9:** Convergence of the particle diameter and Full Width Half Maximum (FWHM) of the fitted normal distribution (not shown) represented by the dimensionless change in mean in the y axis as a function of the sample count in the x-axis. Convergence is taken when the y-axis value goes below 1% and here the samples required for convergence is 200

values of both parameters calculated as:

$$X_{\text{Normalised}} = \frac{\bar{X}_s - \bar{X}_n}{\bar{X}_n}$$

where  $\bar{X}_n$  is the mean of the parameter across all samples and  $\bar{X}_s$  is the mean calculated till sample 's' seen in the x-axis of the figure. When the normalised mean drops below 1% on the y-axis, the convergence criteria is deemed sufficient. This occurs for roughly 200 samples and so the mean particle diameter for 645 samples is taken as the particle diameter (619  $\mu\text{m}$ ) in all the subsequent sections.

### 2.3.3. Suspension preparation

The suspension was prepared using the sieved particles and the glycerol-water mixture along with Iridin flakes. In addition to the above, 0.1g per 100 ml of the solution of Tween-20 surfactant was added to lower the surface tension and properly wet the particles. The method for the detailed preparation of the suspension can be found in section D.2. Various combinations of the suspension were tested to check for neutral buoyancy and the suspension with a density of 1187.5  $\text{kg}/\text{m}^3$  was chosen as the working fluid as the particles remained suspended in the solution overnight. This can be seen in the very high value of sedimentation velocity, reported in Table 2.3.

After the suspension was prepared, the particles that lingered at the top were removed and the remaining 'good' particles were used for all the tests. Many particles had voids inside them, making them lighter, as seen in 2.3.2. In addition to this error in particle density, significant temperature changes affected the density of the system and hence the neutral buoyancy, as shown in Table 2.3. In spite of the temperature variations, the sedimentation velocity of the particles is relatively low that they are much longer than the duration of a recording (30 seconds). The lack of neutral buoyancy is evident at lower Reynolds numbers and experiments where the quasi-steady ramps are increasing from rest, quantified based on settling time. The settling time is calculated from the Stokes' law for the terminal velocity of a sphere falling in a fluid.

$$v_{\text{sed}} = \frac{g d_p^2 (\rho_p - \rho_{\text{sol}})}{18\mu}$$

In the above equation, the sedimentation velocity is calculated from the density of the particles ( $\rho_p$ ) and solution ( $\rho_{\text{sol}}$ ), the solution dynamic viscosity ( $\mu$ ), particle diameter ( $d_p$ ) and the acceleration due to gravity ( $g$ ). The settling time is taken as the time taken for a single particle to settle 10 cm, which is approximately

half of the cylinder length. The values of settling time for different densities of the solution are presented in Table 2.3.

In the same vein, the system is sheared up and the solution is allowed to settle for at least 20 minutes before the start of each experimental run. However, there are cases where the sedimentation time of the particles is of the order of magnitude of the waiting time, mainly due to extreme temperatures. The residual motions in the fluid after shear do not die down even after a few hours but after the experiments are started from low rotational frequencies, the rotational input of the system is the dominant driving force for the particle motion. During the experiments, the suspension density was maintained by the periodic monitoring of its density (adding glycerine/water in required quantities) using an Anton paar DMA 5000 density meter.

**Table 2.3:** Density variation with temperature and its effect on both the neutral buoyancy and the settling time

Temperature [°C]	Viscosity [m <sup>2</sup> s <sup>-1</sup> ]	Density [kg/m <sup>3</sup> ]	% of particle density	Sedimentation velocity [m/s]	Time taken to settle 10 cm [hours]
20	2.41e-5	1187.5	99.96	3.64e-6	7.63
25	1.87e-5	1184.5	99.71	4.71e-6	0.842
30	1.47e-5	1181.5	99.45	7.78e-5	0.357



# 3

## Single-phase flows: Validation

The first half of this chapter contains aspects of data processing that deal with extracting qualitative and quantitative information from the TC system. Based on the data obtained, various flow regimes in this setup are classified and described in the single-phase flows section of this chapter. This not only provides a basis for comparing the particle-laden suspension cases but also helps in establishing the parameter space of this experiment to compare with other famous works over the years.

### 3.1. Data processing

The data acquired from the system can be divided broadly into two groups: imaging and torque measurements. Before the methods of processing the data are explained, a small section on the experimental matrix is described.

#### 3.1.1. Experimental test matrix

For all the cases of single-phase flow, two types of experiments were conducted, called 'QSup' (Quasi-Steady up) and 'QSDown' (Quasi-Steady down). Both experiments were quasi-steady runs where the frequency of the inner cylinder rotation was increased in predetermined steps. The experimental run where the steps increased from rest to the maximum frequency is called 'QSup' and the reverse case was called 'QSDown'.

The purpose of conducting two quasi-steady experiments was get an idea of the hysteresis response of the TC system. From the observations of Gul et al. [29] on the same setup, the hysteresis observed could have been due to the system geometry, but its occurrence was attributed to a "genuine change in the flow dynamics". This also affects particle-laden flows, where there are clear differences in the boundaries of transition and this will be explained later, in 4.

For the single-phase flows, the test matrix ranges from 0 Hz (rest) till the maximum safe limit of the motor rotational frequency, 6 Hz. To avoid damaging the torque sensor, the safe limit for the torque was set to be 8 Nm. The Reynolds number range covered is not the same for QSup and QSDown, as the corresponding same frequencies of both the runs are conducted at different temperatures. The steps are finer from 0 Hz (rest) till 1 Hz, with a step size of 0.05 Hz/step. The steps are coarser after 1 Hz and remain constant at 0.1 Hz / step till 6 Hz (maximum).

#### QSup

These experiments are conducted from rest till the maximum rotational frequency of the motor that is within safe limits of operation (for the torque sensor). As the flow is started from rest, the system needs to be well mixed before each run. This is because the Iridin pigments added for flow visualisation are heavier than the fluid and if the system is started without pre-mixing, these pigments are settled at the bottom and take time to completely spread throughout the system. To avoid this, the system is sheared at a high shear rate for some time (approx. 5 min) till the Iridin is well mixed and the motor is then switched off.

The experiments are started after around 20-30 minutes to allow the residual motions to die down. This is not sufficient for all the motions to die down, but this is deemed sufficient based on the fact that the vortices disappear from the imaging sections and the entire TC cell seems laminar from the outside. For QSup, the

first measurement is the rest case for 90 seconds and the measurements start from 0.1 Hz, for which the speed is held constant for 90 seconds.

### QSDown

The QSDown measurements start from 6 Hz (maximum) and end with the TC cell at rest. As the experimental run starts with a high rotational input, additional time for dispersing Iridium is not required. Similar to QSU<sub>p</sub>, the first measurement is 90 seconds of no rotation to calibrate the offset (if any) for the motor. To facilitate proper mixing, after rest, the maximum input (6 Hz) is given for 5 minutes before the quasi-static steps are commenced. Each rotational frequency is maintained for 90 seconds, same as the QSU<sub>p</sub> experiments.

For both the above types of experiments, at the end of the test matrix, a rest case for 90 seconds is run to double-check if the system has maintained a constant offset throughout the experiment. In many cases, there was a slight offset change and this shift was noticeable sometimes in the middle of a measurement. In all the cases, the actual frequency of rotation differed from the given input. To calculate the Reynolds number of the flow, the TTL pulse counter was used to get the actual frequency of rotation. The two cases are represented in Figure 3.1. The times shown in the figure are excluding the acceleration time taken to reach each step. The motor has an acceleration rate of 0.05 Hz/s.

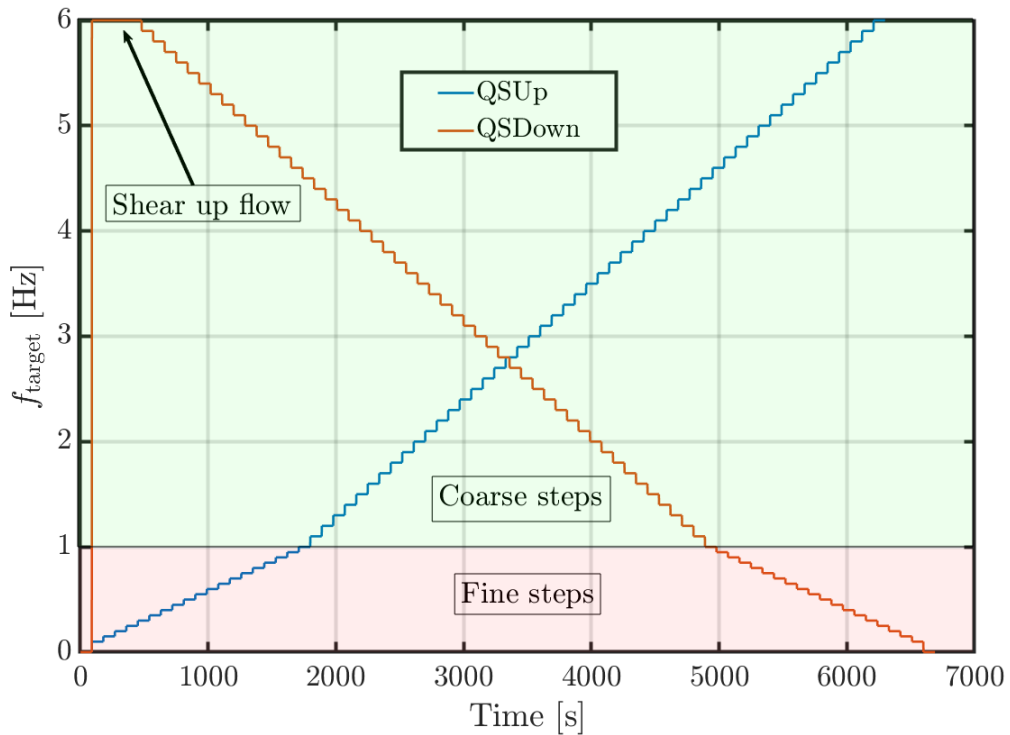


**Figure 3.1:** Representation of the two experimental runs: QSU<sub>p</sub> and QSDown. The time stopped at each rotational frequency is 90 seconds, with the shear up for QSDown indicated separately. Acceleration between the frequencies is not included in this plot and the frequencies indicated here are the targeted frequencies of rotation, not the achieved frequencies. The steps are finer up to 1 Hz and coarse then on till 6 Hz.

### 3.1.2. Imaging

For all the experimental cases, the images captured by the camera are processed in two stages. First, they are exported from the DAVIS 10.0.5 software to the more usable '.tif' format. Secondly, the frames stored as '.tif' files still contain a large amount of data and so the useful information is extracted from these images and stored as an array. This is done in MATLAB and the resulting files are compact and have a '.mat' file format. This process flow is presented in Figure 3.2.

Two types of images are taken within the 90 seconds of a single measurement: A shorter recording at 50 fps for the full FOV and a longer recording for a cropped FOV at 100 fps. The shorter recording is done to get a

snapshot of the entire TC cell for a given rotational frequency while the longer recording contains the actual data that is processed further to make space-time plots.

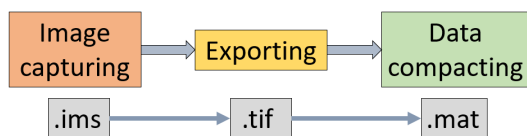


**Figure 3.2:** Data processing steps starting from image capture till the extraction of useful data shown alongside the corresponding file formats

**Table 3.1:** Table showing the different types of images recorded for each rotational frequency

Frame rate [s <sup>-1</sup> ]	Recording duration [s]	Number of images	FOV [pixels × pixels]
50	0.2	10	2160 × 2560
100	30	3000	200 × 2560

### 3.1.3. Space-Time (S-T) plots

One of the primary methods of characterising the flow in this report is by utilising Space-Time (S-T) plots. These plots are obtained by the following method, also illustrated in Figure 3.3:

- The centre line of the captured images is extracted and stored as a vector
- This contains the information of the pixel intensity at a given point in time
- This process is repeated for all the images for a given recording
- The vectors are concatenated to form an S-T plot. This gives the pixel intensity of the centre line of all the images as a function of time

Before obtaining the S-T plots, the images have to be corrected for the angular illumination source, which causes a gradient in illumination intensity across the image in the axial direction. To correct for this gradient, the following steps were followed:

- A laminar flow case was taken as a template mainly because there were no distinct flow features
- For one horizontal line across the image, a mean pixel intensity value was obtained
- This was repeated across the whole image to obtain an axial profile of mean pixel intensities
- All the images were divided by this correction profile and this produced the gradient corrected images which were used to get the S-T plots

This is also extended to the space-time plots of all the cases based on the laminar flow measurement of a single case. In spite of this, the top 5.5 mm of the TC cell is not well defined as the shadow of the top lid covers that region. This results in almost no light from that region hitting the camera sensor. Nevertheless, this does not affect the quality of the rest of the image and since this is limited to a very small region, this was neglected in processing. This is more apparent in the cases where there are distinct flow features such as Taylor vortices.

### Spectral analysis of the S-T plots

The method used to quantify the features from the captured images is through the analysis of the generated S-T plots (subsection 3.1.3). The quantifiable parameters are the frequencies, both along with the space and the time axes. The pixel intensities are considered along a line (direction depends on the choice of spatial or temporal frequencies) and the data is transformed using a Fast Fourier Transform (FFT). The squared amplitude of the power spectrum is plotted on a log-log scale which gives the spectrum with the amplitude on the y-axis and the frequency on the x-axis. The peaks of this power spectrum are found and this gives the dominant frequencies of the signal. Differentiating between the peaks to determine actual dominant frequencies and harmonics was done manually. The same procedure was followed for obtaining both the spatial and temporal dominant frequencies. All the flow regimes presented in the second half of this chapter are defined based on their dominant frequencies or lack thereof.

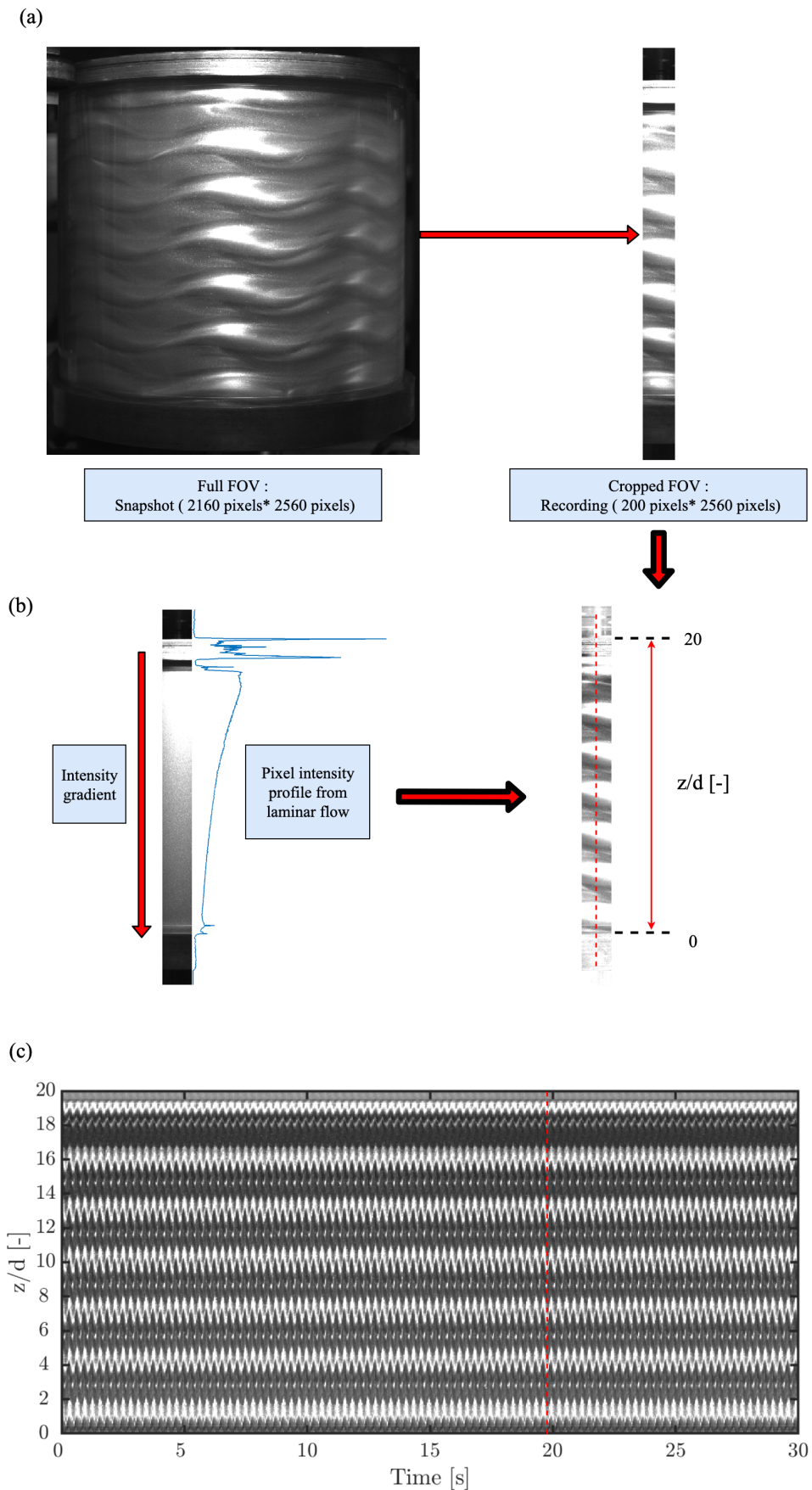


**Figure 3.3:** Steps followed to process the images: (a) The two FOV captured during each measurement run with 2160 and 200 pixels recorded in the horizontal axis. (b) Gradient correction procedure: the pixel intensity profile across the axial direction of laminar flow is taken as the correction vector to obtain the intensity corrected cropped FOV. (c) The S-T plot obtained from the single red line across the whole measurement duration for the Wavy Vortex Flow (WVF) regime.

### 3.1.4. Torque measurements

The torque on the inner cylinder is measured along with readings from the actual rotational frequency from the TTL counter. Both of these are sampled at 2000 Hz and the continuous readings throughout the experiments are averaged in blocks to get values at each rotational frequency. It should be noted that the torque is measured along the whole length of the inner cylinder shaft and not only in the middle section. This results in the v-K gap contributions adding up in the measured torque values. This is corrected by introducing a v-K correction factor obtained from the skin friction plots.

The torque on the inner cylinder was measured during all the experiments simultaneously while capturing images. Multiple single-phase experiments have delved into the torque analysis mainly for drag reduction and torque scaling [45, 47, 56–59]. In the current experiments, the torque curves are used for validating the system and identifying the first transition from laminar Couette flow to the Taylor vortex flow (refer section 3.2). Three commonly presented parameters are compared to validate the torque measurements and the first transition in the current TC cell.

#### Dimensionless torque

The torque is commonly represented in a dimensionless form by ‘ $G$ ’ [59–61] as:

$$G = \frac{T}{\rho_l \nu^2 L}$$

where  $T$  is the torque in Nm obtained after converting the voltage from the sensor using a calibration curve,  $\nu$  is the fluid viscosity in  $\text{m}^2/\text{s}$  and  $\rho_l$  is the fluid density in  $\text{kg}/\text{m}^3$ . The torque readings in Volts from the sensor were calibrated to adjust for an offset error which caused a non-zero torque value at rest. The method employed for this can be found in section A.1. The first transition of the flow is captured when there is a shift in the slope of ‘ $G$ ’ when plotted against  $Re_i$ . This is captured for both QSup and QSDown, as shown in Figure 3.4a.

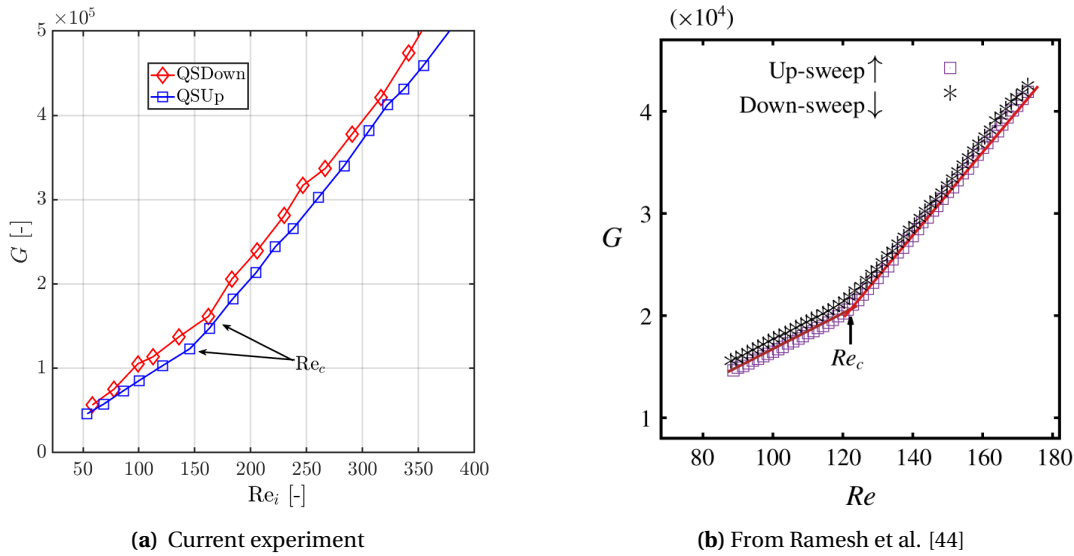


**Figure 3.4:** Variation of dimensionless torque ( $G$ ) with the Reynolds number ( $Re_i$ ) showing the first transition from laminar Couette flow to Taylor Vortex flow. The difference in the values for QSup and QSDown is due to hysteresis. The plot on the right shows the same parameters from the experiments of [44]

The first transition is captured well in the current experiment for both QSup and QSDown. The critical Reynolds number ( $Re_c$ ) is different for both due to the hysteresis present in the system, but they both are higher than the values around 120 found by [16, 43, 44]. This difference can be attributed to the different initial conditions and setup geometries.

### Nusselt number

Studies have related the phenomena of Taylor-Couette flow and Rayleigh-Benard convection, "that which is driven by a temperature difference between a bottom and top plate in the gravity field of the Earth" [58]. The non-dimensional heat flux is the Nusselt number  $Nu$ . In the work of [58], they introduce a new analogy between the two flows and obtain a Navier-Stokes based definition of the transport current  $J^\omega$ , which is given by:

$$J^\omega = \frac{T}{2\pi\rho l}$$

Following the same definition for 'J', the laminar transport term is given by :

$$J_{\text{lam}}^\omega = 2\nu r_i^2 r_o^2 \frac{\omega_i - \omega_o}{r_2^2 - r_1^2}$$

where  $\omega_o = 0$  for pure inner cylinder rotation. The ratio of both these transport terms gives the Nusselt number for the TC flow.

$$Nu^\omega = \frac{J^\omega}{J_{\text{lam}}^\omega}$$

From [58], this quantity "measures how effective the transverse convective angular velocity transport is in terms of purely molecular transverse transport". When this is plotted against the Reynolds number, the first transition is captured when the curve slopes away from 1. This is also well captured for single-phase flows, as shown in Figure 3.5.

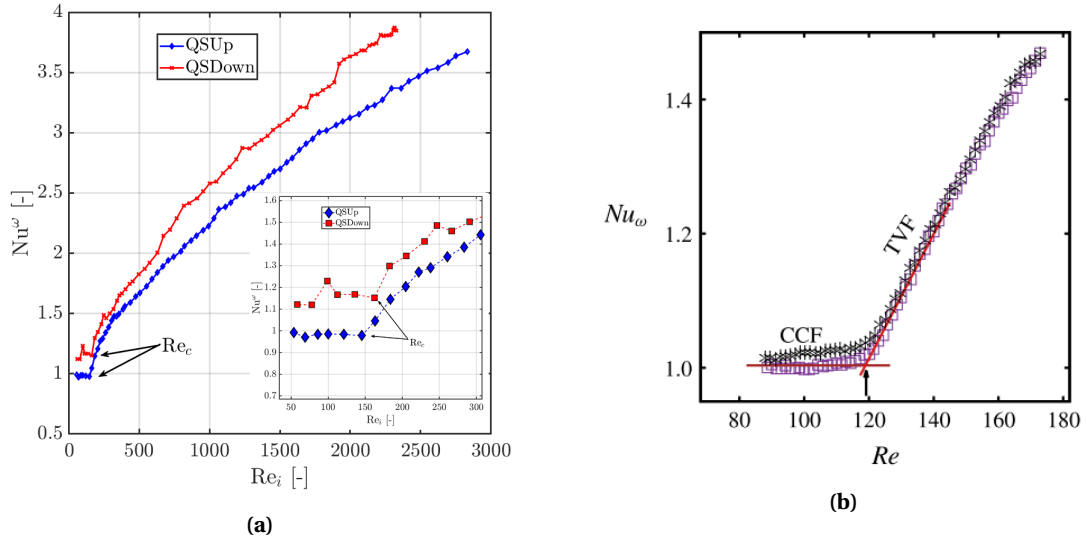


**Figure 3.5:**  $Nu^\omega$  variation with  $Re_i$  showing the first transition from laminar Couette flow to Taylor Vortex flow for (a) the current experiments and (b) from Ramesh et al. [44]. The difference in the values for QSup and QSDown is due to hysteresis. The plot on the right shows the same parameters from the experiments of Ramesh et al. [44]

From Figure 3.5, the agreement is very good for the case of QSup, and even though there is a visible difference in the curves due to hysteresis, the QSDown experiment also agrees qualitatively with the critical Reynolds number.

### Friction factor

Another parameter to quantify the torque in the TC cell is the skin friction coefficient, also referred to as the friction factor. The skin friction coefficient is defined as the ratio of the wall shear stress to the dynamic pressure (Ravelet et al. [62]). The simplified expression for the friction factor is given by:

$$c_f = \frac{Td^2}{\pi\rho_l r_i^2 L t Re_s^2 \nu^2}$$

This is compared to the laminar skin friction coefficient curve, where the friction factor has a  $Re_s^{-1}$  dependence, where  $Re_s = 2Re_i / (1 + \eta)$  is the shear Reynolds number, as defined by Dubrulle et al. [63] for pure inner cylinder rotation.

$$c_{f,\text{lam}} = \frac{2}{\eta Re_s}$$

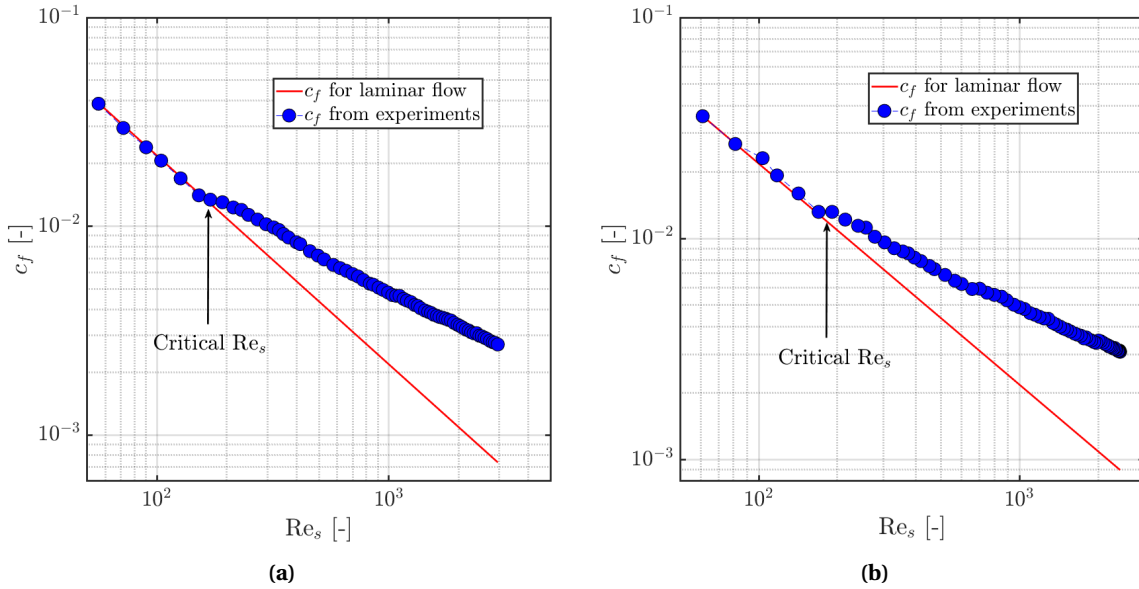


**Figure 3.6:** Skin friction coefficient  $c_f$  plotted as a function of shear Reynolds number,  $Re_s$  for (a) QSUp and (b) QSDown. The point where the experimental results deviate from the laminar friction factor corresponds with the appearance of Taylor vortices.

From Figure 3.6, the point where the curve diverges from the analytical laminar line corresponds with the appearance of the first instability. This is due to the emergence of Taylor vortices, which are described in subsection 3.2.2.

#### Determination of the v-K contribution to torque

The TC cell has a finite length and the effect of this is reflected as a contribution to the torque. Detailed experiments have been conducted on the same TC cell to quantify the contribution of the end effects on the torque [29, 33, 45, 47, 62]. The torque contribution from the v-K gaps was approximately 50 % for the experiments conducted prior. Using that as a base, the skin friction curve (Figure 3.6) was adjusted by trial and error to find at which v-K factor the curve fit well on the laminar flow line. This gave a v-K contribution of 51%. This was set as a constant for all the experiments, including the multiphase flow cases. The reason for the small difference from prior experiments can be attributed to the fact that the TC cell for the current tests used a steel top cover rather than the brass lid which was used earlier. Nevertheless, the contribution is almost the same as prior experiments on the same system.

## 3.2. Flow regimes in the Taylor-Couette system

The flow in a TC system undergoes several transitions and these have been classified in detail by many experimentalists over multiple decades. In this report, definitions have been borrowed from the most common description of regimes, but a few regimes have also been either combined/unmentioned. These distinct states are classified here either by their appearance, symmetry about the cylinder axis, waviness (frequencies) or the lack of distinct features. All the regimes shown below are for the QSDown experiment, except for Turbulent Taylor Vortices (TTV).

### 3.2.1. Laminar Couette flow

In the sub-critical ( $Re < Re_c$ ) range of Reynolds numbers, the flow does not exhibit any distinct features and is laminar throughout the system, as seen in Figure 3.7. The fluid follows the cylinder rotation and this regime is also referred to as "Laminar Couette flow".

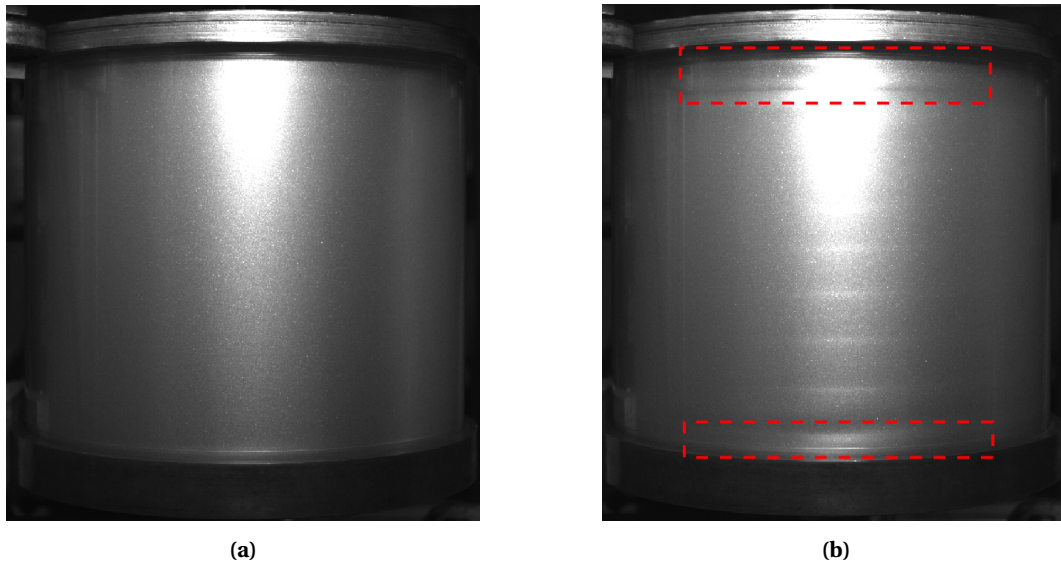


**Figure 3.7:** (a) Snapshot of the laminar TC flow ,  $Re_i = 58$  (b) laminar Couette flow ( $Re_i = 136$ ) with end effects causing Ekman cells to form from both ends, marked by red boxes

It is to be noted that the gap between the ends of the inner and outer cylinders can cause a circulation due to which an instability can arise, even when the bulk of the flow is laminar. To eliminate these, the TC cell should be infinitely long or the independently rotating end rings have to be used, as in Burin [32]. These are termed as Ekman vortices/cells, as seen in Figure 3.7 and even though they may be present, the overall flow is still termed as laminar in this report, as has been the general practice. This end geometry caused flow has been described in detail by Andereck et al. [16], who termed this flow as Azimuthal Laminar flow. They observed this phenomenon until  $Re_i = 100$  for pure inner cylinder rotation. However, the effect of this is limited in larger aspect ratio setups and is absent when Taylor vortices set in. In the current TC cell, they do not affect most of the TC cell axially, with one or two vortex bands from the edges usually being the norm. The effect of these Ekman cells are quantified in the torque measurements, explained in subsection 3.1.4.

This regime is defined by the absence of any distinguishing features and this is reflected by the lack of any dominant spatial or temporal frequency, shown in Figure 3.8. The S-T plot (Figure 3.9) also shows a plain flow field, as is expected from this laminar flow.

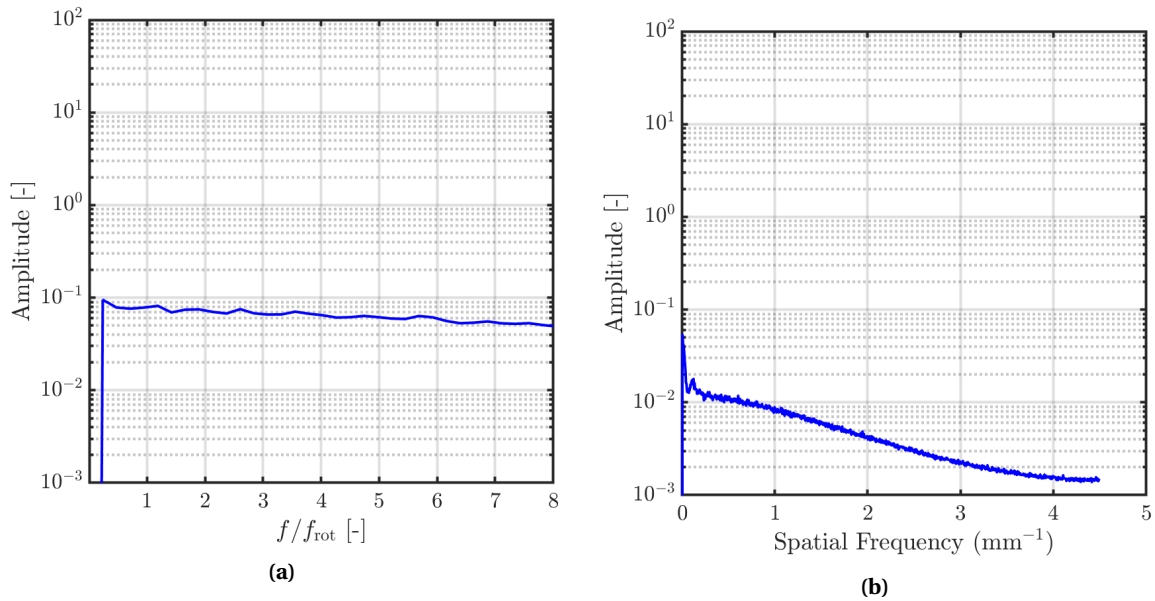


**Figure 3.8:** Power spectrum of the S-T plot with the (a) temporal frequency and (b) the spatial frequency showing a lack of dominant frequencies in both plots.

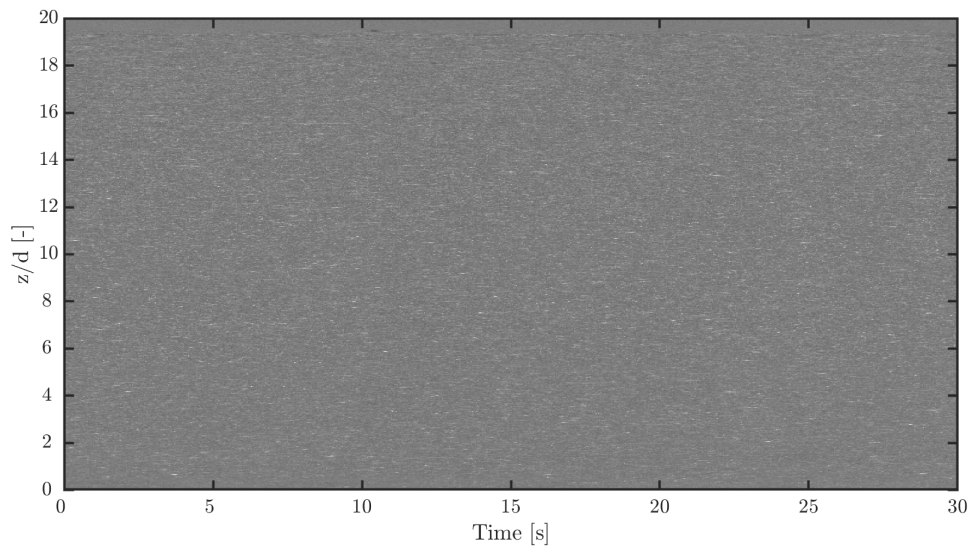


**Figure 3.9:** S-T plot of the laminar Couette flow regime ( $Re_i = 58$ ) in the current TC cell. There are no defining features of the flow visible over time.

### 3.2.2. Taylor Vortex Flow (TVF)

After the laminar flow regime, the flow undergoes a primary bifurcation to reach the Taylor Vortex Flow (TVF) regime. The Reynolds number at which the flow transitions to this regime is termed in this report as the critical Reynolds number ( $Re_c$ ) for transition. The whole flow arranges itself into Taylor vortices in the axial direction, wherein the flow rolls upon itself in the radial-axial plane. The whole axial section is filled with pairs of counter-rotating vortices, causing the alternating bright (outflow) and dark (inflow) bands to appear. A schematic depicting the flow is shown in Figure 3.10b and the corresponding regime in the current experiments is shown in Figure 3.10a.

The power spectrum of this regime shows a clear spatial frequency  $f_{sp}$  which corresponds to the bands forming along the cylinder axis, as seen in Figure 3.11. The spatial frequency is thus a measure of the 'axial wave-

number' of the system. The power spectrum of the temporal frequency shows only a peak corresponding to the frequency of the cylinder rotation ( $f_{rot}$ ). This could arise probably due to the reflection of light from the outer cylinder surface, observed also by Andereck et al. [16]. The defining features of this regime are thus a single spatial frequency and no unique temporal frequency.

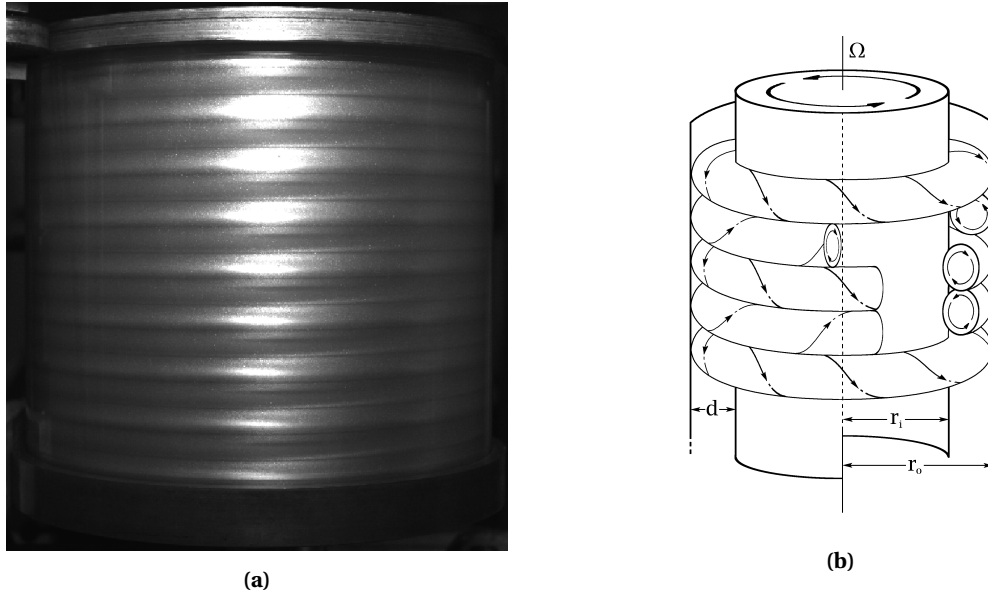


**Figure 3.10:** (a) Snapshot of the Taylor vortices occupying the whole TC cell,  $Re_i = 182$  (b) Schematic representation of Taylor vortices in the TC system, reproduced from Lueptow [3]

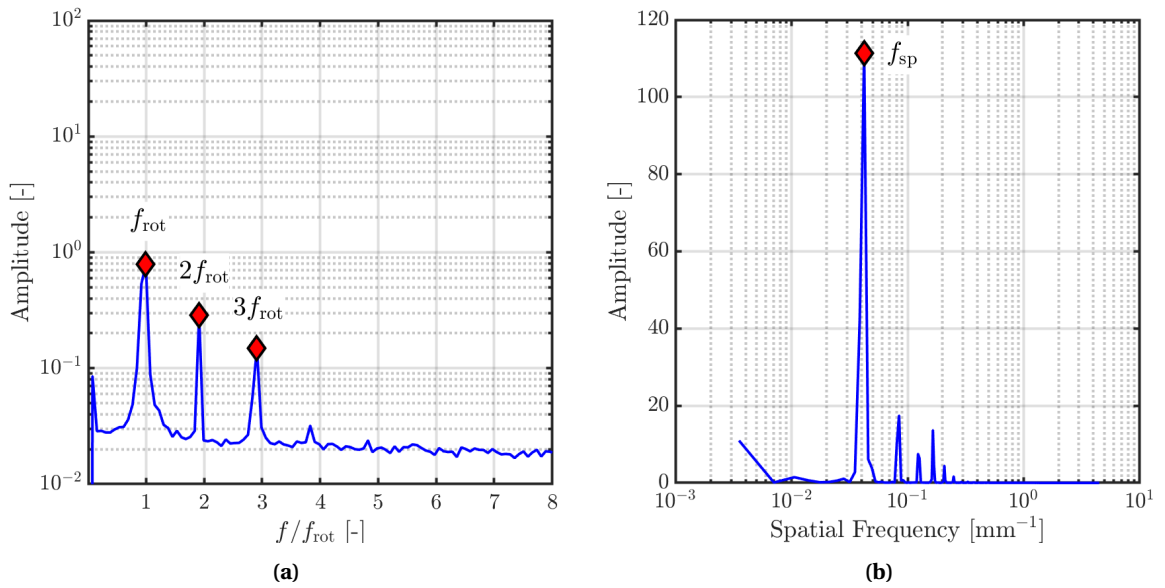


**Figure 3.11:** Power spectrum of the S-T plot with the (a) temporal frequency and (b) the spatial frequency showing only a dominant spatial frequency. The peak seen in the temporal case corresponds to the frequency of the inner cylinder rotation ( $f_{rot}$ ) at  $Re_i = 182$ .

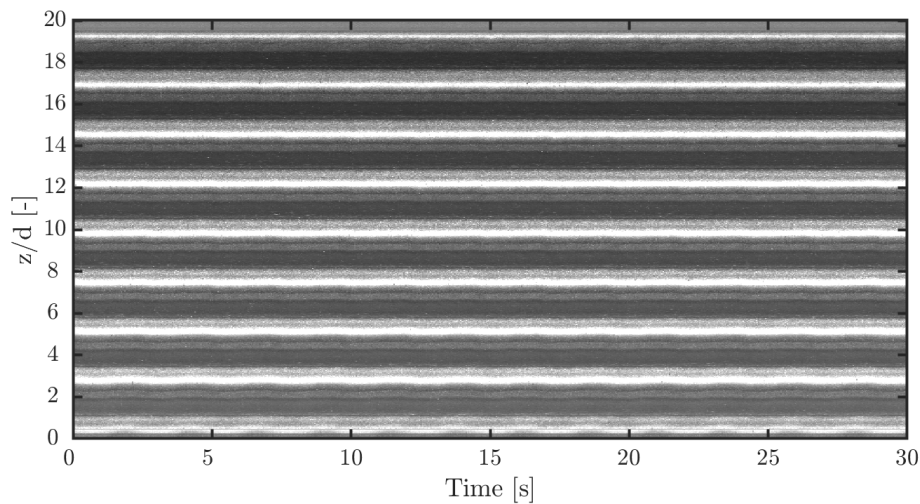


**Figure 3.12:** S-T plot of the TVF regime in the current TC cell at  $Re_i = 182$ . There is a spatial frequency but there are no temporal frequencies.

### 3.2.3. Wavy Vortex flow (WVF)

Beyond the TVF regime, the system transitions to Wavy Taylor Vortex Flow. The Taylor rolls become wavy in the azimuthal direction and their motion can be visualised as they move along the circumference of the outer cylinder. The presence of a wave frequency is used to classify this regime as it is only represented qualitatively as WVF, not based on a fixed value of wave frequency. From Gorman and Swinney [14], this regime is characterised by a single frequency  $f_1$ , which is the frequency of the travelling azimuthal waves passing a point of observation (camera) in the laboratory. This is seen clearly in the captured snapshot of the TC cell (Figure 3.13) and the representation of these vortices in Figure 3.13b, from [3].

This frequency is marked in the spectrum taken from the S-T plots (Figure 3.14), as the peaks indicate one distinct spatial and one distinct temporal frequency. The temporal frequency is visible in the S-T plots as the frequency of the waves across the time axis. The other peaks marked in the spatial frequency plot correspond to the linear integer combinations of the cylinder rotational frequency and the dominant frequency.

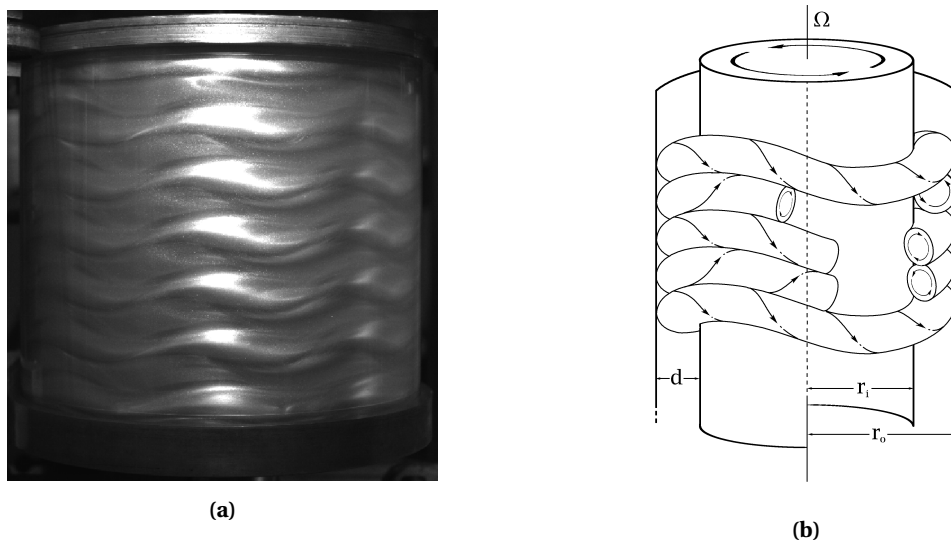


**Figure 3.13:** (a) The Wavy Vortex Flow regime, seen occupying the whole TC system at  $Re_i = 452$  (b) Representation of counter rotating Wavy Taylor vortices, reproduced from Lueptow [3]

The wave frequency changes based on the rotational input of the inner cylinder and this is visible from a

spectral analysis of the captured images.

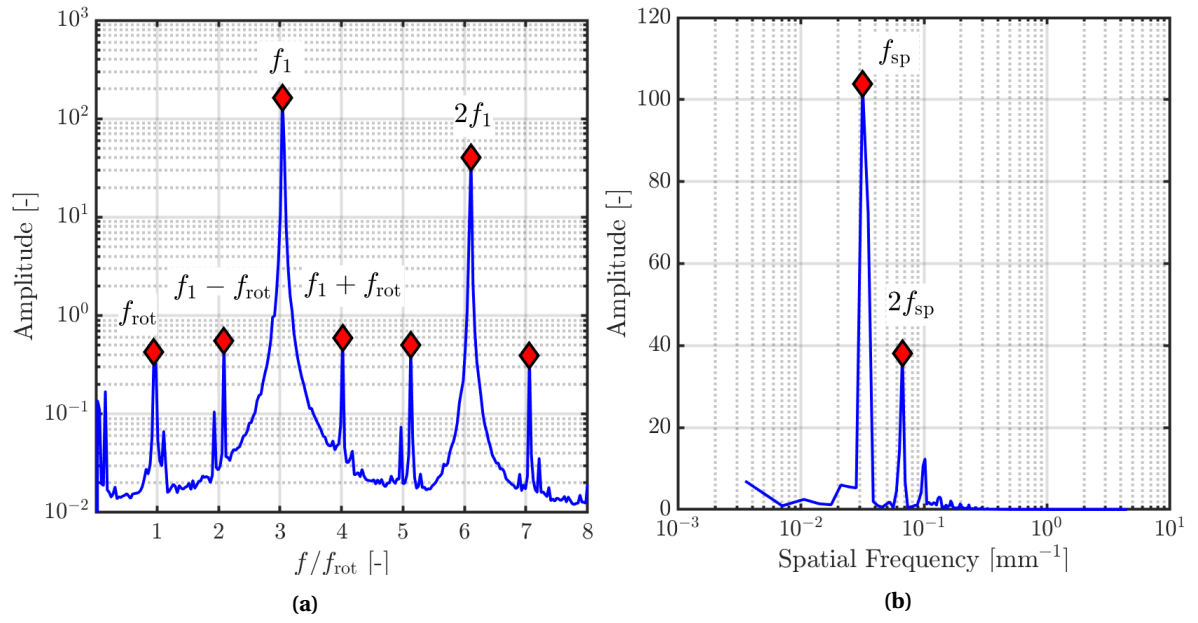


**Figure 3.14:** Power spectrum of the S-T plot with (a) the temporal and (b) the spatial frequencies showing one distinct peak frequency in each. The dominant temporal frequency of the waves is labelled as  $f_1$  and the other peaks correspond to linear integer combinations of  $f_{rot}$  and  $f_1$ .

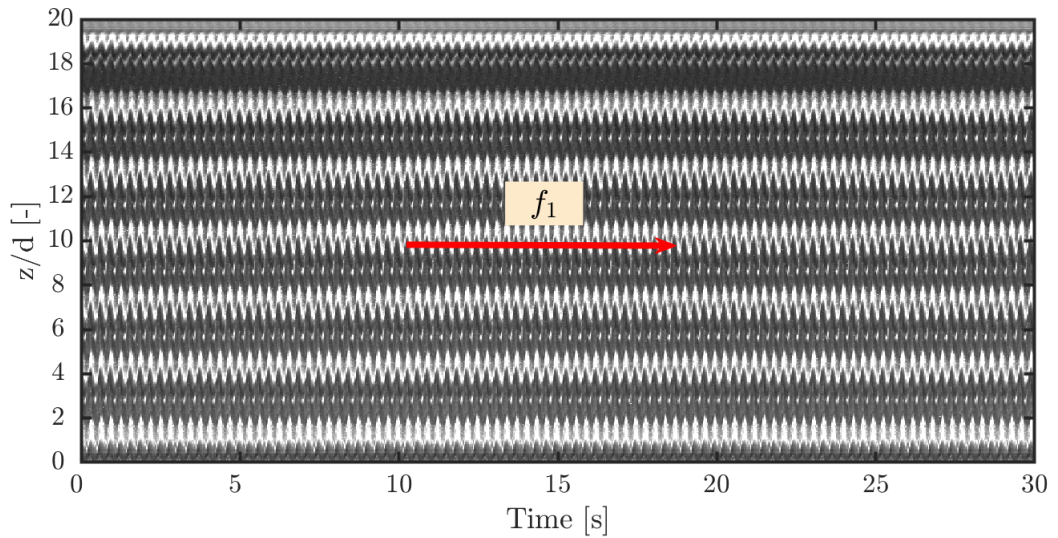


**Figure 3.15:** S-T plot of the WVF regime ( $Re_i = 452$ ) in the current TC cell. There is a spatial frequency and a temporal frequency (marked) that define the flow.

### 3.2.4. Modulated Wavy Vortex flow (MWVF/MWV)

After the WVF regime, there appears a second frequency component in the flow, a picture of which is shown in Figure 3.16. These ‘modulations’ are characterised by either the “broadening of the spectral peak associated with a single temporal frequency or the appearance of multiple distinct dominant temporal frequencies”, as defined by Dutcher and Muller [18]. The latter is shown in 3.17.

These modulations were studied in detail by Gorman [14] as the modulations varied with both the amplitude and frequency of azimuthal waves. In addition to this, the secondary frequency value also varies with the number of azimuthal waves, just like WVF. This regime tends to be relatively unstable in the sense after the MWVF has been established, the next transition is back to WVF before the onset of turbulence. A detailed classification has been made, where the transition back to WVF is labelled as WVF2 and the second appearance of MWVF is labelled MWVF2 by Dutcher and Muller [18]. In this report, this regime is universally called MWVF and its reappearance is also labelled MWVF. This is because the step size is relatively large and so the transition between these regimes is not captured in all the cases. The difficulty is classifying this regime is mainly in identifying the individual peaks in the spectrum.



**Figure 3.16:** Snapshot of the TC cell with modulated waves at  $Re_i=1233$

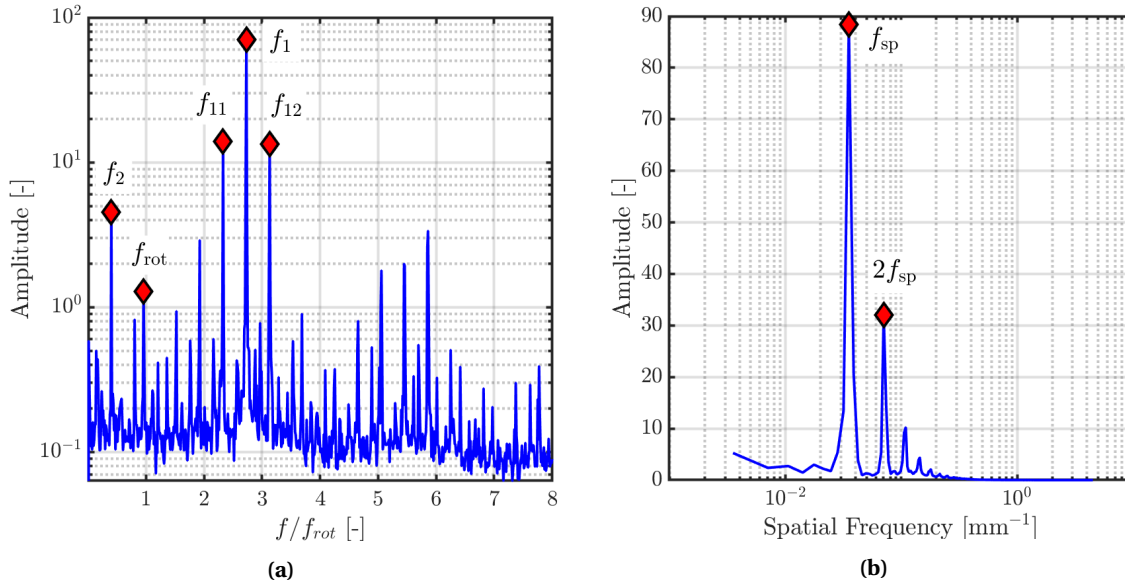


**Figure 3.17:** Power spectrum of the S-T plot with the (a) temporal frequency and (b) spatial frequency showing one dominant spatial frequency but multiple dominant temporal frequencies, which is the defining characteristic of this regime. The frequency of wavy vortices that persists is  $f_1$ , while the new component that causes the modulation is  $f_2$ . This results in the peaks  $f_{11} = f_1 - f_2$  and  $f_{12} = f_1 + f_2$  for  $Re_i=1233$ .

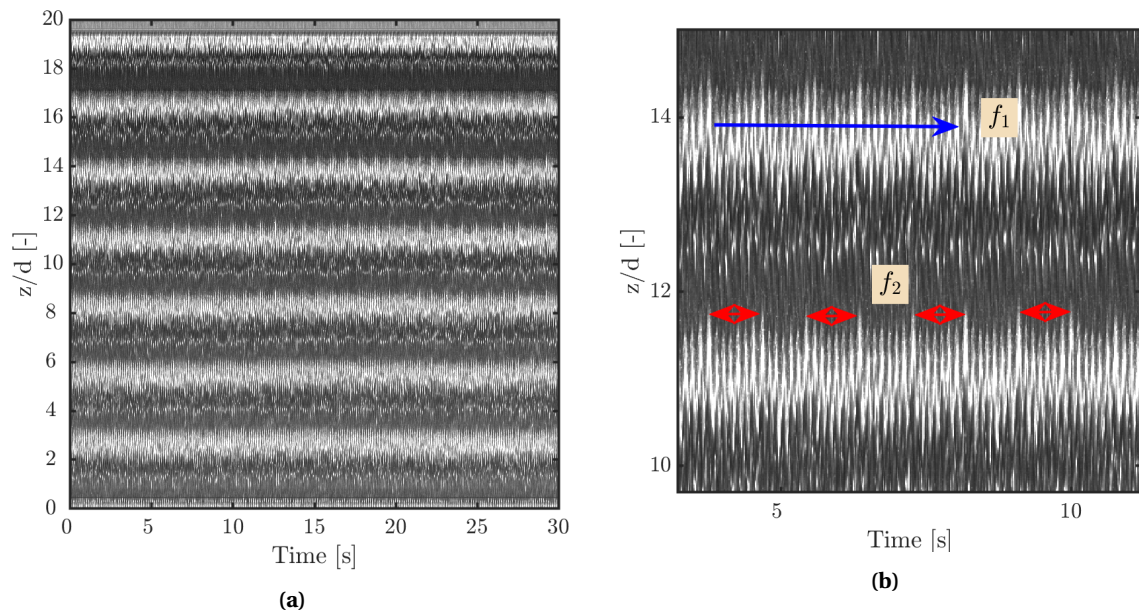


**Figure 3.18:** (a) S-T plot of the MWVF regime in the current TC cell. There is an additional temporal frequency which emerges in the flow when compared to WVF. (b) A closeup of (a) is shown to indicate the two frequencies that are present in the flow for  $Re_i=1233$ .

### CWV and WTV

The appearance of transients or chaos in the snapshots only increases the complexity of classification in the MWV regime. Two new regimes lie between modulated waves and completely turbulent Taylor vortices, and these are the Chaotic Wavy Vortex (CWV) and the Wavy Turbulent Vortex (WTV) regimes. The classification is made mainly to compare with the transition map of Dutcher and Muller [18] (Figure 1.7) for single-phase flows.

As the Reynolds number is increased from modulated waves (after the switching between MWVF and WVF), the spectrum starts to become noisier due to the development of chaos in the system. This is reflected in the spectrum (Figure 3.19a) by the increase in noise and the reduction in the amplitude of the earlier peaks. There are multiple temporal dominant frequencies, but from the S-T plot (Figure 3.20a) the frequencies are difficult to isolate.

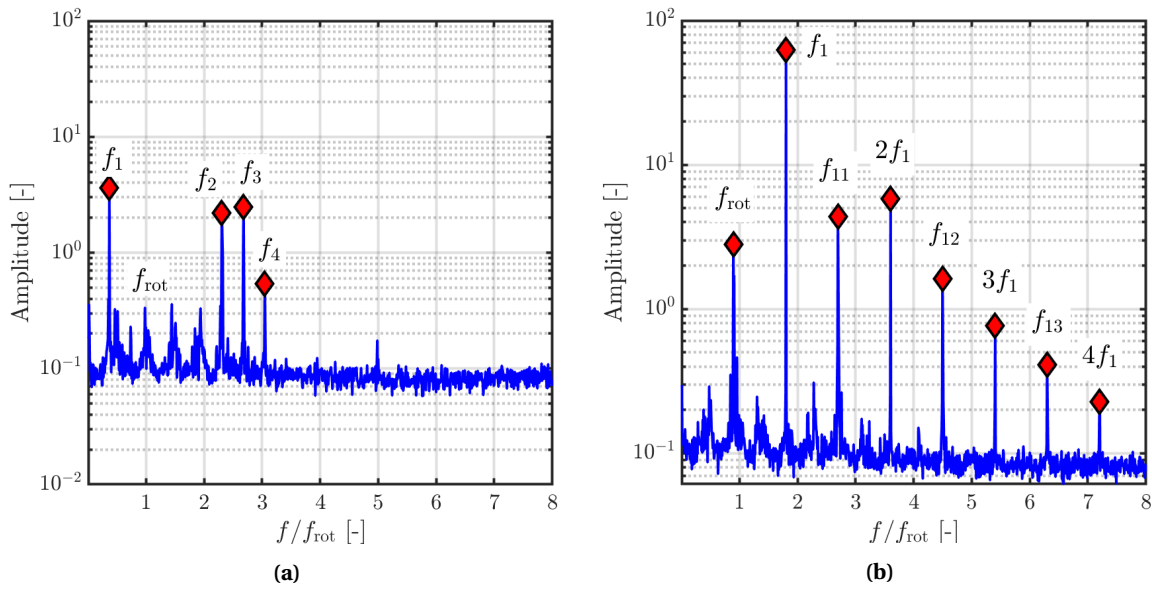


**Figure 3.19:** Spectral plots of temporal frequency for (a) Chaotic Wavy Vortices (CWV) at  $Re_i = 1804$  and (b) Wavy Turbulent Vortices (WTV) at  $Re_i = 2039$ . The CWV spectrum has multiple frequencies that are dominant, similar to MWVF but with an increase in low amplitude noise. The WTV regime occurs after CWV and it contains one distinct dominant frequency in the spectrum.

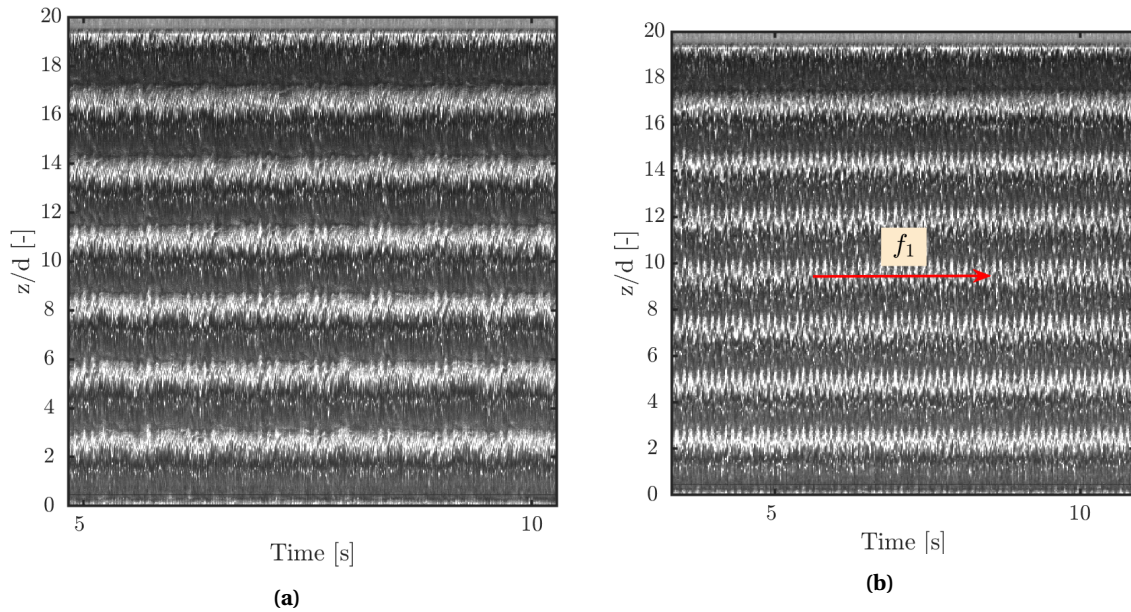


**Figure 3.20:** S-T plots of (a) CWV which does not seem to have a well defined periodicity temporally and (b) WTV, which has a distinct wave frequency  $f_1$  even with the presence of chaos in some bands.

After the CWV regime, the flow gets some of its organisation back as the modulations seem to disappear both from the S-T plot (Figure 3.20b) and the spectrum (Figure 3.19b). This regime is called Wavy Turbulent Vortices (WTV) and is spectrally similar to WVF with one difference, the presence of noise. This is also visible in the S-T plot, where the waves are distinguishable, but the presence of the so-called chaos is evident.

### 3.2.5. Turbulent Taylor Vortices (TTV)

After the WTV regime, turbulence sets in. The waviness that defined the flow disappears and the whole TC cell has turbulence within the Taylor bands (Figure 3.22a). This results in the flow having only one spatial frequency and no temporal frequency, as seen in Figure 3.21 and Figure 3.22b. Interestingly, this regime only appears for the QSup trial. This could be because the Reynolds numbers attained for the QSup experiment were much higher than the QSDown experiment due to temperature differences.

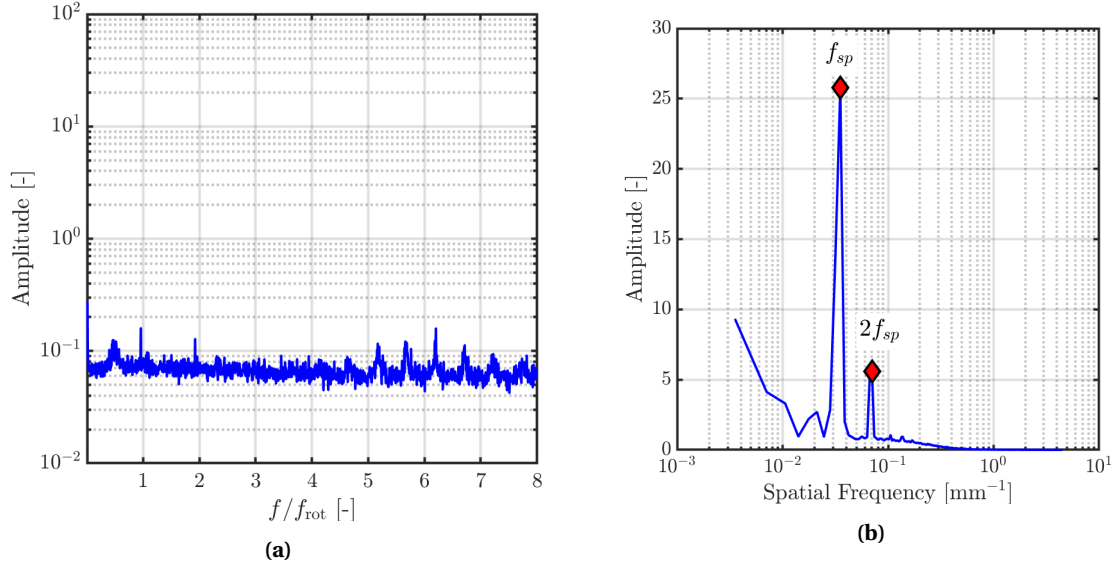


**Figure 3.21:** Power spectrum of the S-T plot with the (a) temporal frequency and (b) spatial frequency. There is no dominant temporal frequency while there is a distinct spatial frequency ( $Re_i = 2833$ )

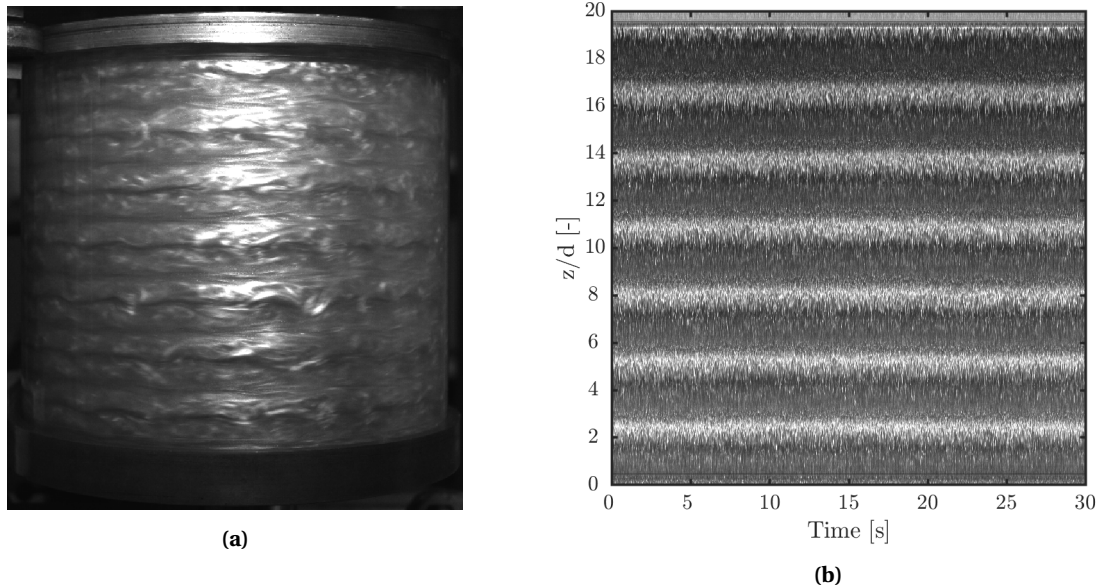


**Figure 3.22:** (a) Snapshot of the TC cell with the turbulent Taylor vortices (b) S-T plot of the TTV regime in the current TC cell at  $Re_i = 2833$  in the QSup experiment. The flow resembles TVF with the difference being that the Taylor bands contain turbulence within them.

### 3.3. Transition map

The different flow regimes observed in section 3.2 have been studied in great detail in the past. However, it necessary to classify the regime map for this TC system due to the intrinsically different nature of the Taylor-Couette flow for different setups. For each separate system, due to the changes in geometry, there will be a quantitative difference in what is observed and in addition to this, there is an effect of the route taken to achieve a flow state (hysteresis, refer to Coles [10] for an idea of the uniqueness of the states for TC flow). To understand and classify the regimes and provide a basis to compare multiphase flows with, a schematic is presented in this section.

#### 3.3.1. S-T transition and hysteresis comparison

From the regime classification of the QSup and QSDown trials, there is significant hysteresis present, as shown earlier with the transition between regimes. The transition map of the QSup and QSDown experiments is shown in Figure 3.23. The order of transition between the regimes is qualitatively almost the same. There is an extra WVF-MWVF switch in the QSUP case and two important changes are present: while the QSup case does not have the WTV regime before transitioning to TTV, the TTV regime is absent in the QSDown experiments. The range of Reynolds numbers covered for both the experiments are different, and no two Reynolds numbers are the same for both experiments. This majorly explains the hysteresis with respect to the regimes, but the step size in the current experiment is too coarse for an accurate quantitative hysteresis analysis to be done.

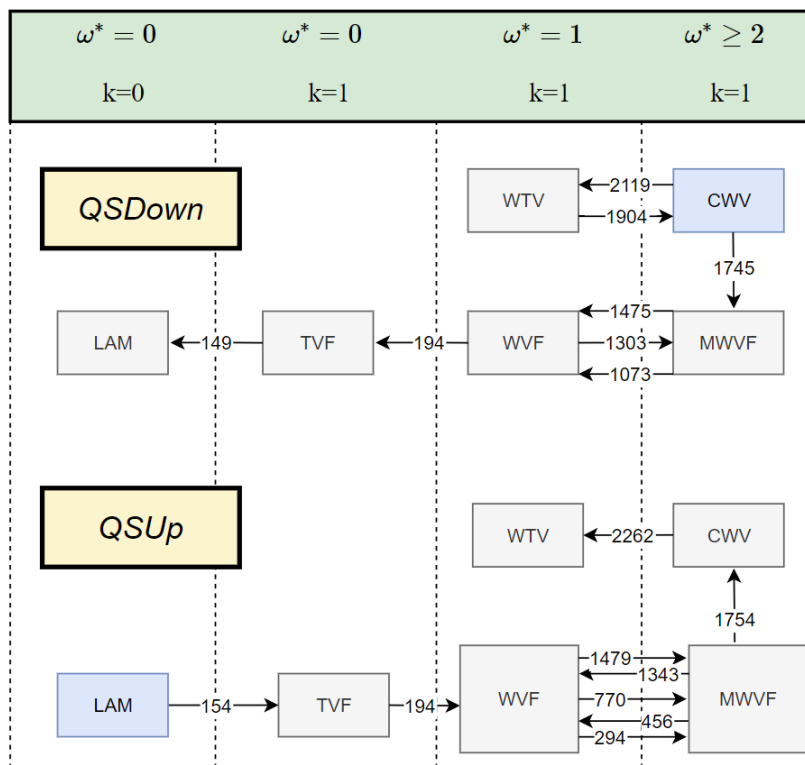
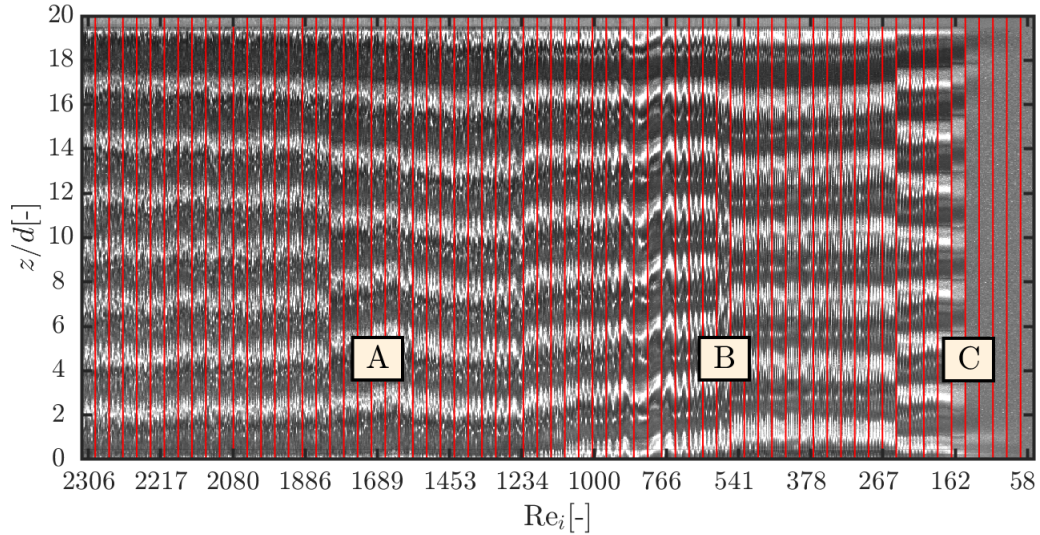


**Figure 3.23:** Transition map for the QSDown and QSup experiments. The start of the experiment is indicated by the blue box in each case and the Reynolds number at which transition occurs between the regimes is represented. The regimes are categorised based on the number of distinct spatial frequencies ( $\omega^*$ ) and distinct temporal frequencies ( $k$ ), based on the descriptions of the regimes provided in earlier sections.

The transition map is organised such that the regimes are also represented based on their power spectra. The temporal frequencies are labelled  $\omega^*$  and the spatial frequencies (axial wave number) by  $k$ . At higher Reynolds numbers for the current experiments, the temporal frequencies are highest and both  $\omega^*$  and  $k$  are zero for laminar Couette flow. To explain some of the transitions in detail, the QSDown case is considered for further analysis.

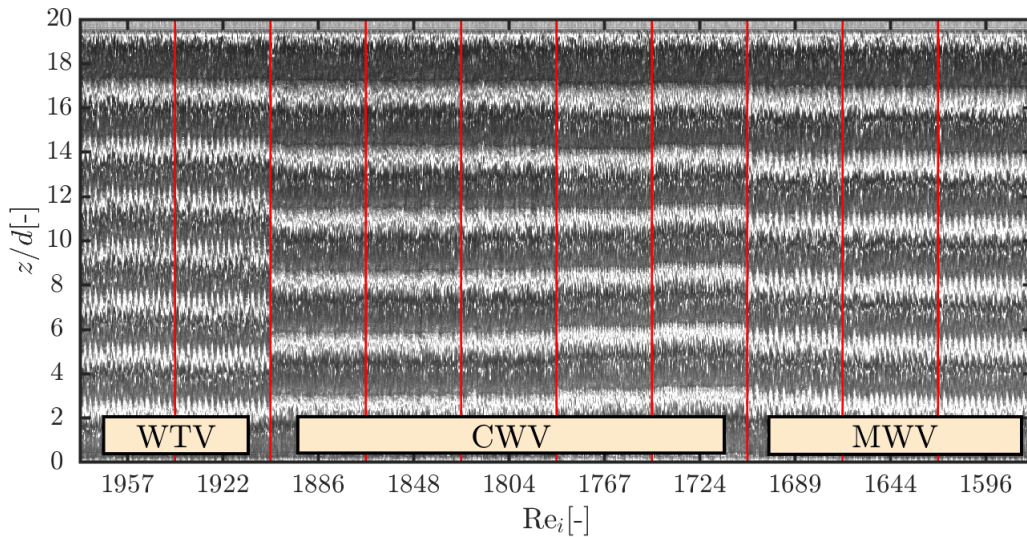
### 3.3.2. Transition/state S-T analysis - QSDown

For the single-phase results presented, to get a better picture of the transition behaviour, a consolidated S-T plot is presented in Figure 3.24. Here, two seconds of each S-T plot of every 30-second measurement is cropped and stitched over the entire range of the experimental run. Each separate experiment is demarcated by red vertical lines. This gives an overall idea of the transitions in the experiment and to analyse this further, three regions are shown in detail.



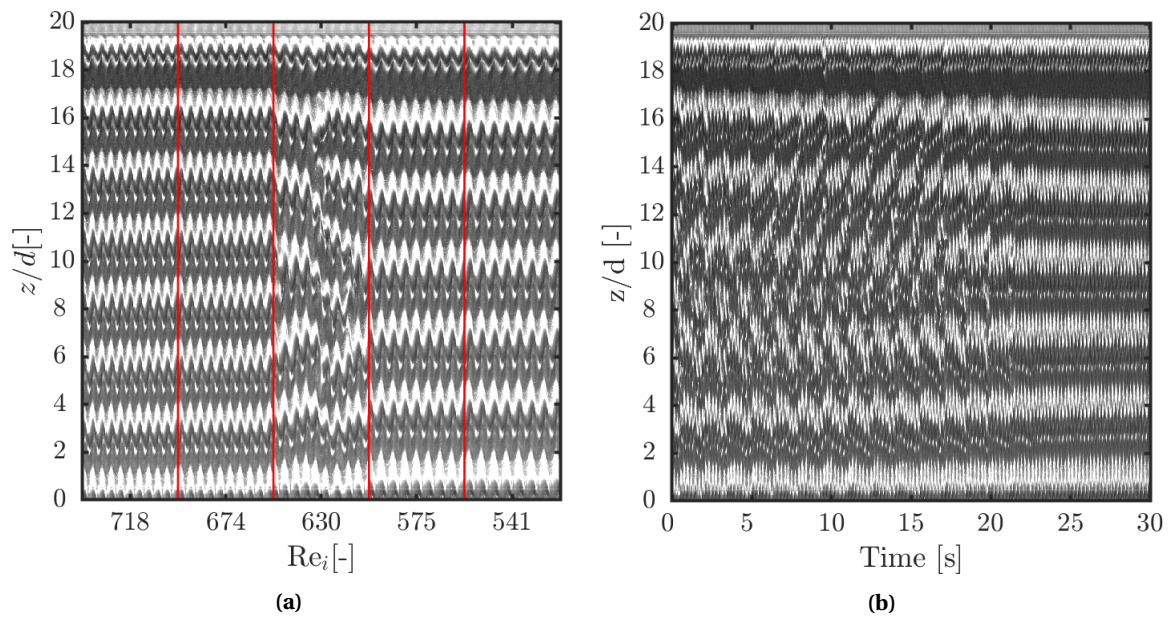
**Figure 3.24:** S-T plot of the entire QSDown experiment. For representation, two seconds of the 90-second S-T plot of every individual measurement is plotted here, separated by red lines. Three regions marked are analysed further.

A



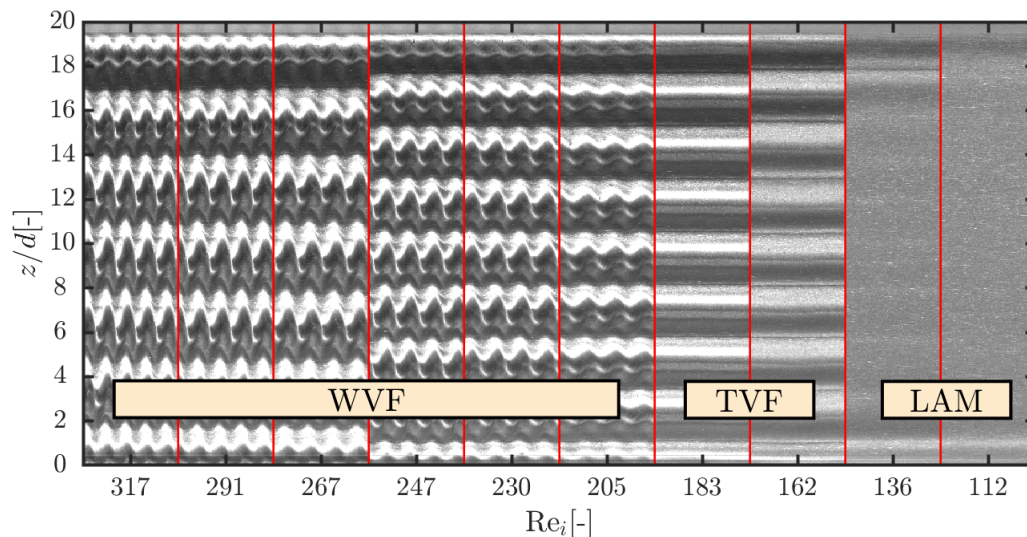
**Figure 3.25:** Close-up of region 'A' in Figure 3.24. There are two changes in flow regime: first, the emergence of chaos from WTV and then the switch to MWVE, where there are multiple distinct temporal frequencies.

In Figure 3.25, the two interesting transitions are highlighted. From left to right (experimental order), the flow transitions from WTV to CWV and finally to MWVE. The chaos in the CWV regime is clearly seen, while the other two regimes have a distinct periodicity to them. The multiple temporal frequencies in the MWV regime are not visible in this 2 second window, and this is not explained further as it has the same type of modulations shown in subsection 3.2.4.

**B**

**Figure 3.26:** (a) Close-up of region 'B' in Figure 3.24. There is no regime change in this set of Reynolds numbers, but the measurement of  $Re_i = 630$  shows transients that occur between regimes of shifting axial wave number. (b) S-T plot of  $Re_i = 630$  showing the development of the transients, seen in (a). These transients stabilise near the end of the recording.

This region is highlighted mainly because there is no transition in flow regime, as all the regions are WVF but the S-T plots seem to indicate otherwise for  $Re_i = 630$ . There are transients in the flow probably because the flow exhibits a reduction in spatial frequency, thus causing the number of axial bands to reduce. When the full S-T plot of  $Re_i = 630$  is observed (Figure 3.26), the transients disappear and it might be that a change in the number of axial bands takes a longer time to stabilise.

**C**

**Figure 3.27:** Close-up of 'C' in Figure 3.24 showing three regimes within this range of Reynolds numbers. The WVF loses its periodicity to form TVF, which transitions to laminar Couette flow.

From Figure 3.27, multiple transitions are occurring in this lower range of Reynolds numbers. The flow transitions from wavy vortices, loses its temporal periodicity to become Taylor vortices at  $Re_i = 183$  and finally transitions to laminar Couette flow at  $Re_i = 136$ . Even within the WVF regime, there is a change in the number of axial waves, from  $Re_i = 267$  to  $Re_i = 247$ .

### 3.3.3. Transition/state frequency analysis - QSDown

The spectral plots shown for all the regimes give a good idea on the state of the flow system. Using the peak dominant frequency in each regime normalised by the rotational frequency, the transitions are classified. This is shown in Figure 3.28, where the changes in frequency values correspond to change of state, regime or both.

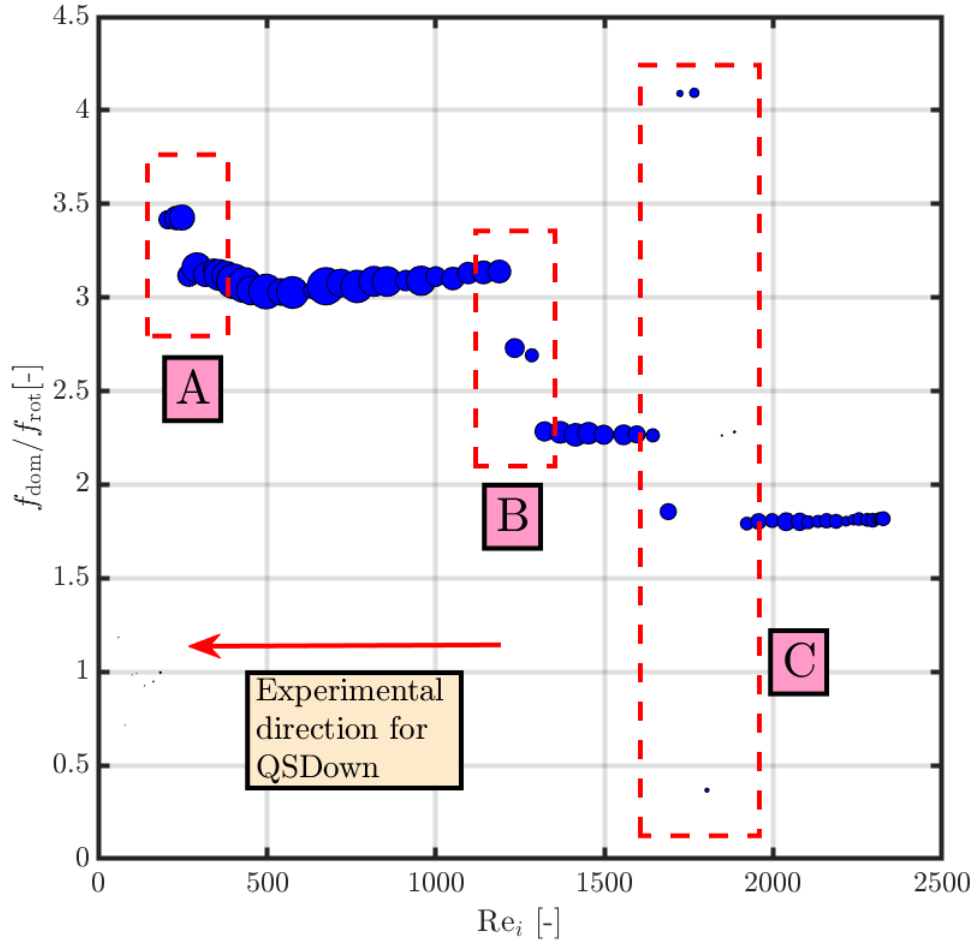


**Figure 3.28:** Variation of the peak dominant frequency (normalised) with the Reynolds number for the QSDown case. The regions indicated by A,B and C are analysed further to explain the reason for the change in  $f_{\text{dom},1}/f_{\text{rot}}$ . The marker size indicates the amplitude of the dimensionless frequency ratio  $f_{\text{dom},1}/f_{\text{rot}}$ .

For the changes in dominant frequencies shown in Figure 3.28 for the QSDown case, the transition map is as follows: The flow is laminar up to the critical Reynolds number, ( $Re_c = 149 \pm 13$ ), where the first transition to TVF occurs. The error is mainly due to the step size of each measurement. When  $Re_i$  changes from 136 to 162, the transition from the laminar regime to TVF occurs. The transition is determined as the mean Reynolds number between the two measurement points, with an error of half the step size. Even though the experiment is a QSDown trial, the transitions below are explained from left to right.

#### A

The appearance of the first big marker in Figure 3.28 corresponds to the appearance WVF at  $Re_i = 194 \pm 11$ , or  $Re_i/Re_c = 1.3$ . This is because the WVF is the first regime after laminar Couette flow to have a distinct

temporal frequency. Within 'A', there is a step down around  $Re_i = 238 \pm 8$ , and this is due to a change in the number of azimuthal waves, even though the flow is still WVF. The change can be seen in the snapshots of the system, and the number of azimuthal waves reduces from 8 ( $Re_i = 246$ ) to 7 ( $Re_i = 266$ ). The number of waves is found by comparing the snapshot of the flow with the calibration image. From the conversion using a scaling factor, the number of waves around the TC system is obtained, to a reasonable degree of accuracy for WVF. The snapshots are shown side by side in Figure 3.29, where even a cursory glance can detect a reduction in the number of waves (increase in wavelength). After the step down, the flow then transitions to MWVF without a change in  $f_{dom,1}/f_{rot}$ .

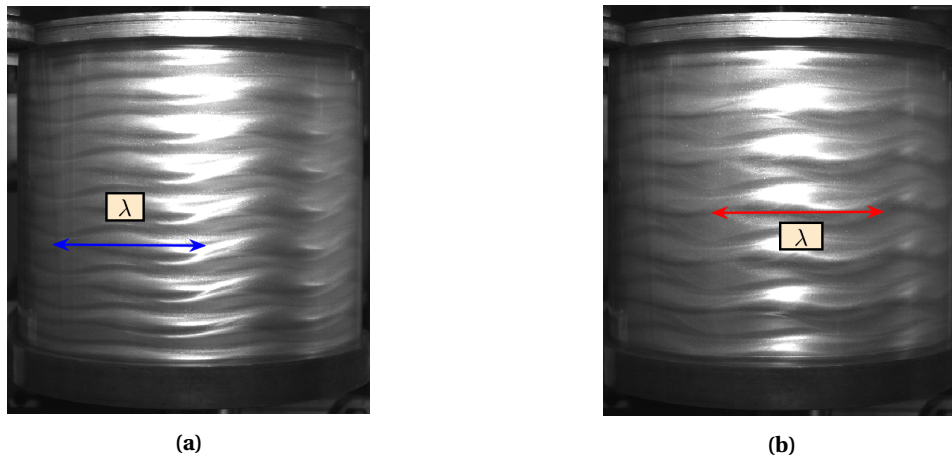


**Figure 3.29:** Snapshots of the TC system showing a change in the wavelength of WVF resulting in a reduction in the number of azimuthal waves from (a)  $Re_i = 246$  to (b)  $Re_i = 266$

**B**

The two steps in region 'B' are due to a change in the flow regime. The modulated waves change back to WVF for two measurements, as seen in Figure 3.30 and then another switch back to MWV causes the second step down.

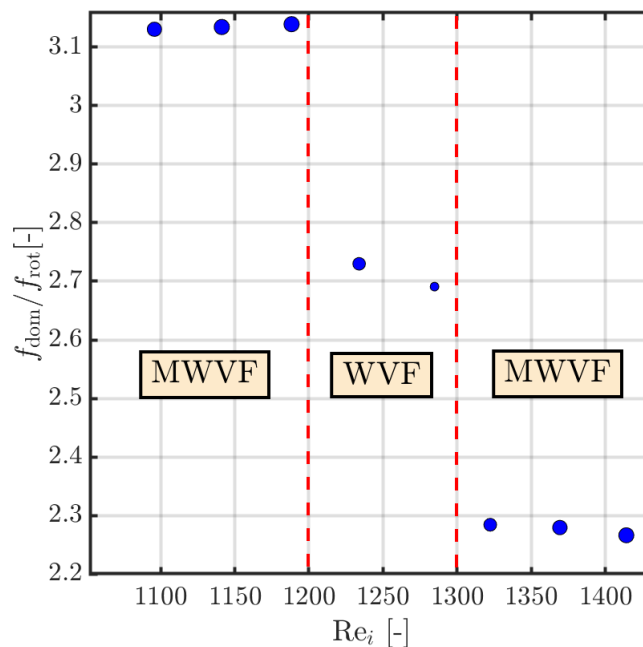


**Figure 3.30:** Close up of Figure 3.28, focussing on region 'B' and showing that the step change in  $f_{dom,1}/f_{rot}$  is caused by transition to different regimes.

**C**

The emergence of noise/chaos in the system causes a significant reduction in the amplitude of  $f_{\text{dom},1}/f_{\text{rot}}$ , hence the small size of the markers. The flow shifts from MWVF to CWV around  $\text{Re}_i = 1745$  and the presence of chaos in the system is reflected by the very low value of  $f_{\text{dom},1}/f_{\text{rot}}$  (small marker size). An increase in Reynolds number causes the flow to have a distinct temporal frequency again, and this is the WTV regime.

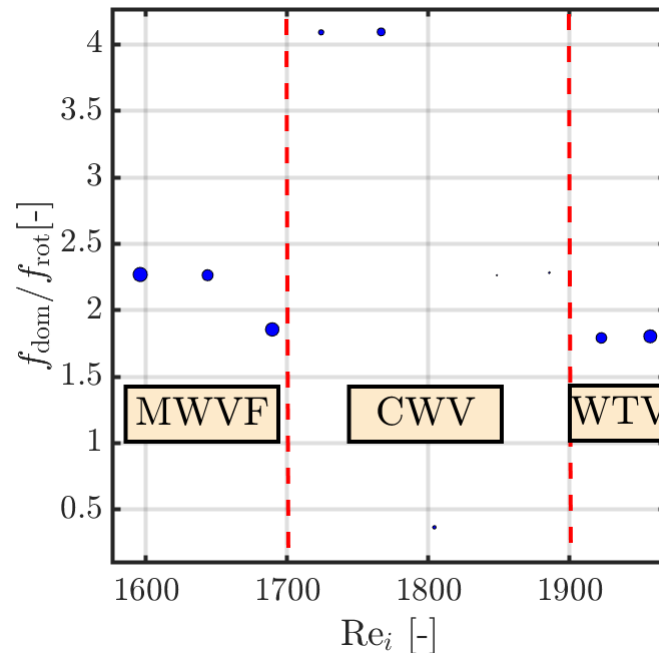


**Figure 3.31:** Close up of Figure 3.28, focussing on region ‘C’ and showing that the step change in  $f_{\text{dom},1}/f_{\text{rot}}$  is caused by transition to different regimes. The emergence of chaos causes a diminishing value of  $f_{\text{dom},1}/f_{\text{rot}}$ , indicated by small markers.

The single-phase flow analysis not only serves as a validation for the system, it also gives an idea of the limitations present in the current measurement method. Overall transition behaviour of the flow can be deduced and the regimes present can be determined in a holistic sense. However, hysteresis and shorter experimental time (90 seconds for each rotational frequency) result in an overall qualitative analysis of the flow phenomena in the TC system, not a microscopic quantitative analysis of each transition.

# 4

## Multiphase flows

The primary research question of the current thesis assignment is to understand how the flow responds to the addition of particles in the established single-phase flow of the TC system. The new flow phenomena that occur due to multiphase flow are described along with the observed flow transitions. This chapter initially contains the results summarising the entire multiphase flow campaign on the TC cell. The complete experimental parameters along with the observed results and discussion are presented. The latter half of the chapter takes a closer look at a single case of multiphase flow detailing the flow regimes and some interesting transitions that occur in the TC system.

### 4.1. Experimental parameters

When particles are added to the system, they should ideally be ‘neutrally buoyant’ and the method for their preparation was described in subsection 2.3.3. However, during the addition of particles to the system some fluid was lost and when the temperature effects were included, this neutral buoyancy was affected. Their effect on the sedimentation velocity and viscosity were presented in subsection 2.3.1. To catalogue the density variation across all the experiments, the variation of the suspension to the particle density is shown in Figure 4.1. The particle density is considered to be  $1188 \text{ kg/m}^3$  based on the time they stayed suspended in the fluid of same density. The ratio of the annular gap to the mean particle diameter is  $\alpha = d/d_p = 16.15$ . The volume fraction was varied from 0 till 40%, in steps of 5%. Even though wetted (particles rinsed in water) PMMA particles were added to the TC cell (Weight of wet particles =  $1.3 \times$  weight of dry particles based on weight comparisons), the volume fraction was calculated based on the dry particles present in the system. The TC cell had 1785 ml of fluid and weighed approximately 2118 g at the time of measurement.

The effect of the particles on the flow is first classified by two dimensionless numbers: the Stokes number and the particle Reynolds number. The Stokes number is classically defined as the ratio of the particle response time to the fluid time in a flow. A low Stokes number ( $St < 0.1$ ) is ideal when the particles in a suspension are to behave like tracers (follow the streamlines of the fluid) and when the Stokes number is high, the particle motion is dominated by inertia. The particle Reynolds number gives the ratio of particle inertia to the viscous forces that surround the fluid. A high particle Reynolds number indicates an increased effect of particle inertia.

$$\text{Re}_p = \frac{\rho_f \dot{\gamma} d_p^2}{4\mu_s} \quad \text{St} = \frac{m_p \dot{\gamma}}{3\pi\mu_f d_p}$$

where  $\dot{\gamma}(r) = 2\omega_i \frac{r_i^2 r_o^2}{r_o^2 - r_i^2} \frac{1}{r^2} [\text{s}^{-1}]$  is the shear rate,  $m_p$  and  $d_p$  are the particle mass and diameter respectively, and  $\rho_f$ ,  $\mu_s$  are the fluid density and dynamic viscosity respectively while  $\mu_f$  is the liquid viscosity. The particle motions in the system are intuitively non-Brownian, and this is confirmed by a high value of the Peclet number, which gives the ratio of the advective to the diffusive transport rate.

$$\text{Pe} = \frac{6\pi\mu_s d_p^3 \dot{\gamma}}{k_B T} \sim O(10^{10})$$

where  $k_B = 1.38 \times 10^{-23} \text{ m}^2 \text{ kgs}^{-2} \text{ K}^{-1}$  is the Boltzmann constant and T is the temperature, taken as 293 K. The high order of the Peclet number confirms the non-Brownian particle motion.

The values of these non-dimensional numbers are summarised in Table 4.1 along with the corresponding values used in the works of [43, 44] wherein the adapted values are all taken from Ramesh et al. [44]. The values shown correspond to their setup geometry, which is also specified in the table.

**Table 4.1:** Comparison of the important dimensionless parameters between the present study and works of Majji et al.[43], Ramesh et al.[44]

Parameter	Majji et al.[43]	Ramesh et al. [44]	Current experiments
$Re_p$ [-]	$O(10^{-6})$	$O(10^{-5})$	$O(10^{-2})$ ( $\dot{\gamma}_{min}$ ) to 1.87 ( $\dot{\gamma}_{max}$ )
$St$ [-]	$O(10^{-6})$	$O(10^{-4})$	$O(10^{-3})$ ( $\dot{\gamma}_{min}$ ) to 0.41 ( $\dot{\gamma}_{max}$ )
$Pe$ [-]	$O(10^{11})$ and $O(10^9)$	$O(10^8)$	$O(10^{10})$
Aspect ratio, $\Gamma$ [-]	20.5	11	22
Radius ratio, $\eta$ [-]	0.877	0.914	0.917
Gap width, $d$ [mm]	7	1.5	10
Particle diameter, $d_p$ [ $\mu\text{m}$ ]	230 and 70	40	619
$d/d_p(\alpha)$ [-]	30 and 100	37.5	16.2
Max. particle loading, $\phi$ [-]	0.30	0.25	0.40

From Table 4.1, due to the wide range of shear rates (inner cylinder rotational rates) used, the criteria for the other two dimensionless numbers vary significantly. At low shear rates, the Reynolds and Stokes numbers are very low, comparable to the values in [43, 44]. However, for shear rates closer to the maximum, both the particle Reynolds number and Stokes number are high, indicating significant particle effects on the flow. A high particle Reynolds number implies that the inertia of the individual particles is high. This, along with a higher Stokes number ( $St > 0.1$ ) results in the particles not following the flow and thus inducing significant particle-particle interactions at increased volume fractions and shear rates.

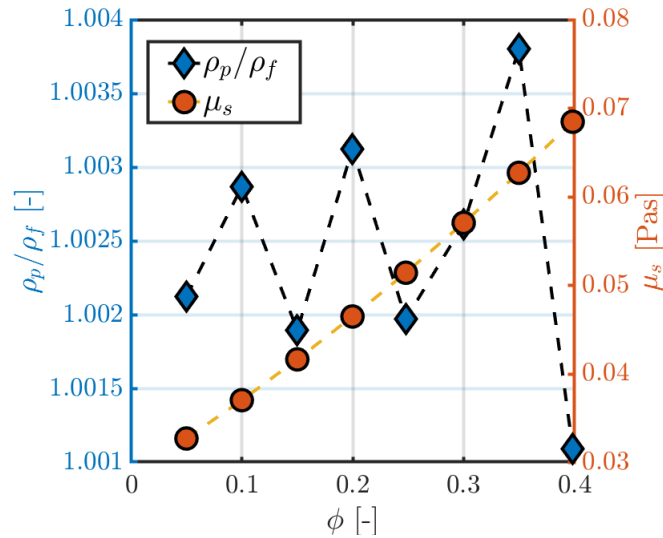


**Figure 4.1:** Variation of the particle to fluid density ratio ( $\rho_p/\rho_f$ ) and dynamic viscosity ( $\mu_s$ ) with volume fraction ( $\phi$ )

Figure 4.1 shows the variation of the dynamic viscosity and dimensionless density as a function of the particle volume fraction. For the calculation of the Reynolds number in all the suspension cases, the effective suspension viscosity based on the Kreiger model is used due to its effectiveness over a larger range of volume fractions (Guazzelli and Pouliquen [64], with  $\phi_c = 0.585$ ).

$$\mu_s = \mu_f [1 + (5\phi/4)/(1 - \phi/\phi_c)]^2$$

Another reason for the variation of solution density is due to the periodic addition of particles. As wetted particles were added, water that entered the system reduced its density. Even though this effect was accounted

for by the addition of extra glycerine, minor differences in density matching were unavoidable. In all the experiments, as seen in Figure 4.1, the particles were slightly heavier than the fluid and this effect was compounded by temperature, wherein there was a reduction in fluid density. An important point to note is that in all the suspension experiments, the Iridium flakes were added for flow visualisation. The refractive indices of the fluid (water-1.33, glycerine-1.473) and the particles (PMMA - 1.49) are close in value which leads to poor visualisation of the flow structures. This issue was resolved by the addition of the Iridium particles as the major flow features were the primary aspect of visualisation, not the individual particles.

## 4.2. Flow regimes unique to particle-laden flow

The addition of particles to the working fluid causes the emergence of new flow regimes that are unique to particle-laden suspensions for the case of pure inner cylinder rotation. Similar to the section on single-phase flows, some of these regimes are described below in detail.

### 4.2.1. Spiral Vortex Flow (SVF)

One of the most prominent differences between the single-phase flows and suspensions is the appearance of spirals for pure inner cylinder rotation. Spirals are characterised by their angular orientation to the axis of the cylinder (Taylor vortices are perpendicular to the axis of the cylinder). A snapshot of pure Spiral Vortex Flow (SVF) is shown in Figure 4.2a for  $\phi = 0.30$ . In the corresponding S-T plot, (Figure 4.3), the inclination of the spirals is clearly seen.

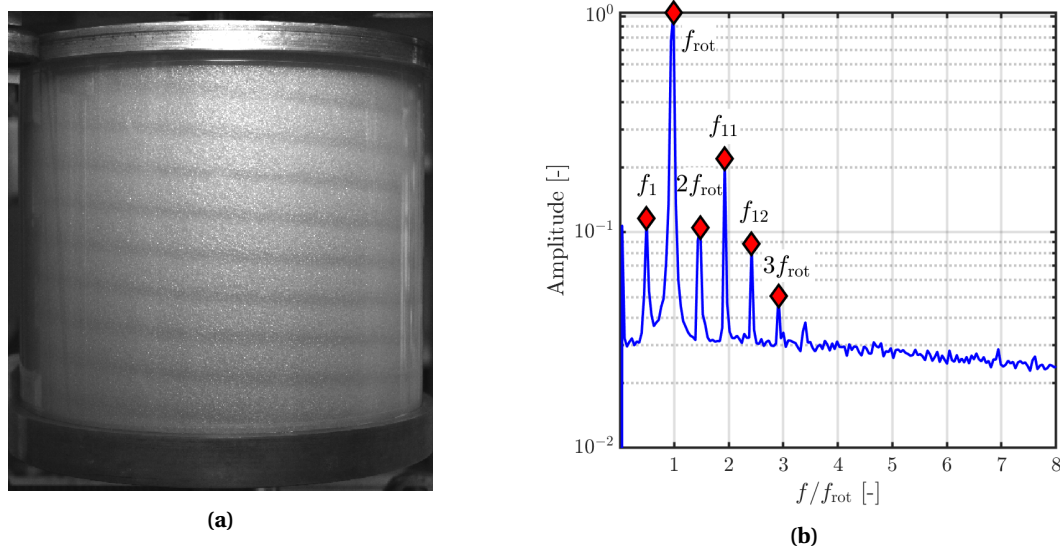


**Figure 4.2:** (a) Snapshot of the spiral vortex flow for  $\phi = 0.30$  (b) Power spectrum of the spiral vortex flow with the marked dominant frequencies.  $f_{rot}$  is the inner cylinder rotational frequency,  $f_1$  is the spiral frequency and the integer combinations of the two are shown as  $f_{11} = f_1 + f_{rot}$  and  $f_{12} = f_1 + 2f_{rot}$

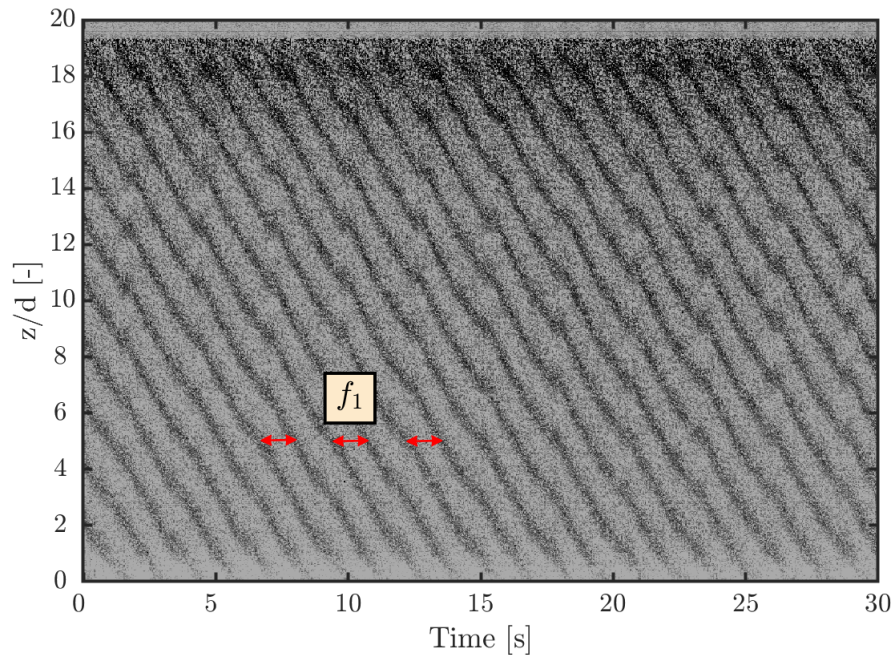


**Figure 4.3:** Space-time plot of the spiral vortex flow, where the frequency of the spirals is shown by  $f_1$  for a suspension viscosity based Reynolds number,  $Re_i = 108$  and  $\phi = 0.30$ .

The spectral plot of this S-T plot shows multiple peaks, clearly designated. The peak  $f_{rot}$  is the cylinder rotational frequency and the characteristic frequency of the spirals is  $f_1$ . This is also shown in the S-T plot. The other peaks which appear in the spectrum are integer combinations of the above frequencies, namely  $f_{11} = f_{rot} + f_1$  and  $f_{12} = 2f_{rot} + f_1$ . Andereck [16] labelled this regime "Laminar spiral" flow for counter-rotating inner and outer cylinders in single-phase flow. Majji et al. [43] found spirals that had an azimuthal speed which was half the speed of the inner cylinder rotation for their suspension study. The spirals moved one axial band in two cylinder rotations for the Majji et al. [43] experiment. In the current experiment, the spectrum is taken horizontally and this will also give the same frequency, thus confirming the motion of spirals is approximately constant across experiments.

### Types of spiral instabilities

The SVF shown in Figure 4.2a is for  $\phi = 0.30$  and it is usually the exception rather than the norm that uniform "laminar spirals" are observed throughout the TC cell. For most of the other volume fractions, the primary instability is associated with the appearance of spirals, but not necessarily occupying the entire axial section. Based on the other flow regimes that appear along with spirals or a waviness that is present on the spirals, other regime classifications that are made.

#### 4.2.2. Wavy Spiral Vortex Flow (WSVF)

In this flow regime, interactions between the spirals and waves cause the 'wavy spirals' to exist. This can also be interpreted as the appearance of spirals in a WVF regime. The snapshot (Figure 4.4a) does not give a good representation of the waviness, which is seen in the S-T plot (Figure 4.5).

The power spectrum (Figure 4.4b) for this particular case does not seem different from laminar SVF. The waviness in the spirals is of very low amplitude and thus it does not appear in the spectrum, which shows only the spiral frequency, the inner cylinder rotational frequency and integer combinations of the two. The absence of waviness could also be explained by the fact that these 'waves' seem to occur at the same frequency intervals as the spirals themselves when traversing horizontally in the S-T plot.

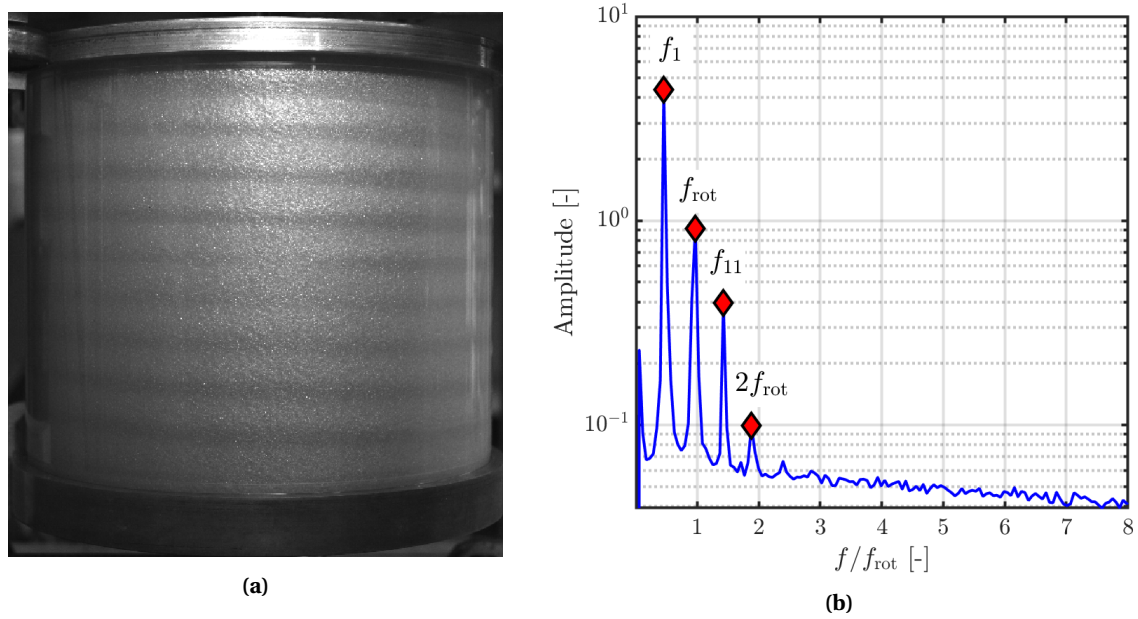


**Figure 4.4:** (a) Snapshot of the wavy spiral vortex flow for  $\phi = 0.20$  (b) Power spectrum of the wavy spiral vortex flow with the marked dominant frequencies.  $f_{\text{rot}}$  is the inner cylinder rotational frequency,  $f_1$  is the spiral frequency (also possibly the frequency of the overlapping waves) and the integer combination of the two is shown as  $f_{11} = f_1 + f_{\text{rot}}$

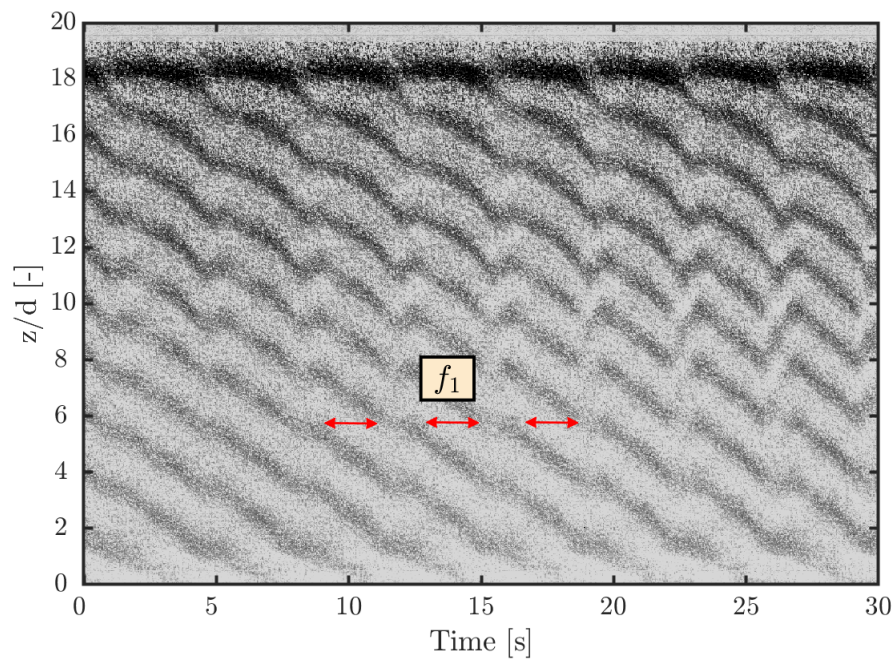


**Figure 4.5:** Space-time plot of the wavy spiral vortex flow, where the frequency of the spirals is shown by  $f_1$ , with  $\phi = 0.20$  and  $\text{Re} = 125$

### 4.2.3. Unstable regimes

In most of the cases, the flow seems to be in an unstable flux, exhibiting multiple regimes in the TC system simultaneously. This phenomenon was observed by Andereck [16], who labelled this a ‘Transition’ regime. This was also classified as a separate list of regimes in Ramesh et al. [44], who designated regime names based on the combination of regimes which coexisted (e.g., WVF+SVF). In the present study, several such regimes were observed, some of which are labelled as: (TVF + IPS), (TVF + SVF), (TVF + TW), (WVF + SVF), etc.

If multiple regimes are coexisting, then it is classified as an ‘Unstable/Transition’ regime, where each regime competes for stability. The regimes mentioned in the list are defined based on their appearance in the S-T plot, and not by their spectra or snapshots. The spectra consist of multiple frequency components, which were difficult to distinguish. The snapshots were not taken from multiple angles or for a longer duration to give a spatial idea of the flow state and so the finer classification of these sub-regimes is a task for future work. In the classification of these regimes, there is also a possibility of misidentification due to the subjective nature of classification.

#### Travelling waves (TW), Inter-Penetrating Spirals (IPS), Ribbons/Riblets (RIB)

Another special regime is designated as ‘Travelling Waves (TW)’. This regime has not been previously described in literature and from the S-T plot (Figure 4.14), it appears to be a low amplitude spike travelling on the Taylor vortices. From the spectra shown later in subsection 4.3.3, one would classify this as WVF as it has one sharp component but it has a completely different behaviour. This regime always occurs close to SVF and this could be an intermediate regime between TVF and SVE. The spirals seeking to split off from the Taylor vortices are not stable enough to sustain SVE, and this could probably be the cause of this regime.

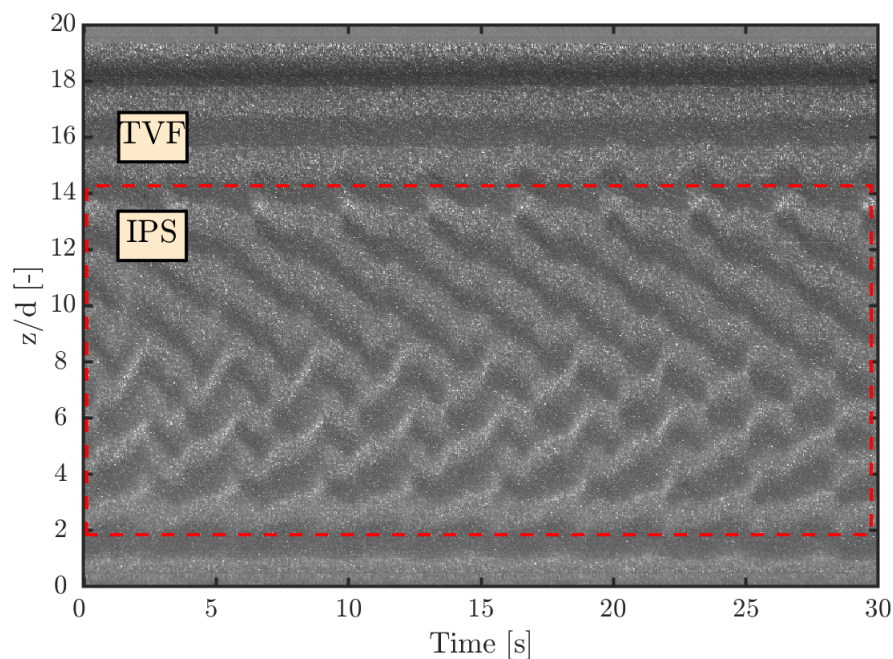


**Figure 4.6:** IPS regime containing both types of spirals (types refer to the inclination : left and right). This is the S-T plot at  $Re_i = 135$  for  $\phi = 0.20$ .

A special case where spirals of opposite inclination coexist is termed as ‘Inter-Penetrating Spirals (IPS)’, shown in Figure 4.6. This has been observed in the case of counter-rotating cylinders [16] (single-phase flow) and in particle-laden flow [43, 44]. When two sets of spirals of opposite inclinations intersect, there is a potential for the formation of riblets/ribbons (RIB). These box-shaped structures are also described briefly in section 4.4. The IPS and RIB regimes are not classified based on their spectrum or snapshots, rather they are solely chosen based on the S-T plots.

### 4.3. $\phi = 0.10$ , a case study

This volume fraction is considered in detail for the QSDown, and all the transitions are broken down based on the observed changes. The S-T figure containing all the information across the range of  $Re_i$  is shown in Figure 4.9, with the labelled regimes present for three ranges of  $Re_i$ . The experiment is a QSDown experiment and all the transitions are thus organised from the maximum Reynolds number to rest. All the transitions for this experiment are shown in Figure 4.7. The regimes are characterised similar to single-phase flow and here the regimes are defined by the number of distinct spatial frequencies 'k' (axial direction) and the temporal frequencies ' $\omega^*$ ' (along time in the S-T plot).

The nature of flow transitions can be observed by a closer look at Figure 4.7. The flow is in the WVF regime from the start of the experiment (maximum shear rate, shown by the green box) till it exhibits its first transition to MWVF. There is a couple of switches after which spirals are formed along with modulated waves. At  $Re_i = 321$ , the spirals disappear to give back the modulated wavy state. The next two transitions are similar to single-phase flow, the route being MWVF-WVF-TVF. It is between the TVF and the laminar flow states that the effect of particles appears again. Non-axisymmetric flow structures that appear initially from TVF are the travelling waves. As mentioned before, these could be the starting point of spiral development and surely enough, the next regime is TVF+SVF. When the Reynolds number is lowered even further, the flow finally becomes laminar, to the circular Couette flow. To take a closer look at the transitions, three interesting regions are considered, whose S-T plots are shown in Figure 4.8.

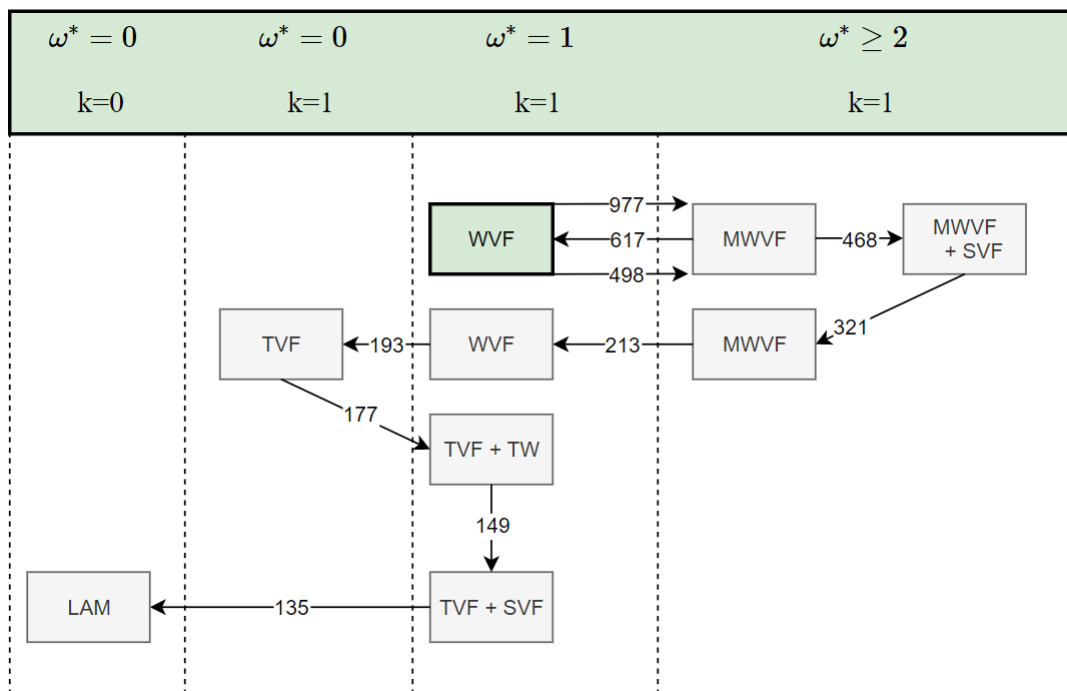


**Figure 4.7:** Complete transition map for  $\phi = 0.10$ , QSDown with the first regime marked with a green box (WVF). Each regime comes under the bracket of a specific spatial frequency (k) or temporal frequency ( $\omega^*$ , called  $f_{dom}$  in most plots). Both of them are obtained from the power spectrum of the S-T plots.

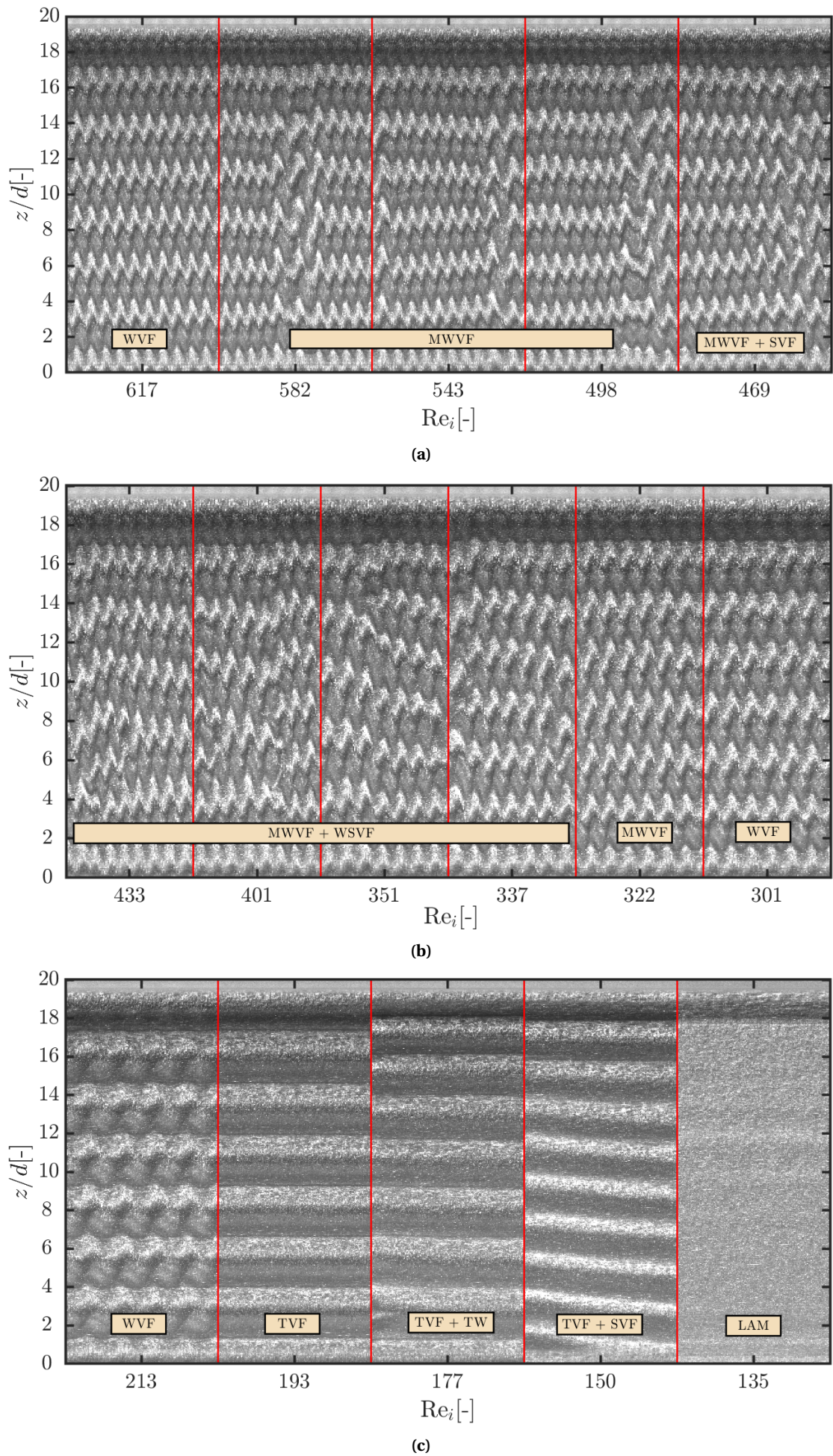


**Figure 4.8:** The three interesting regions from Figure 4.9 are split up and shown here.

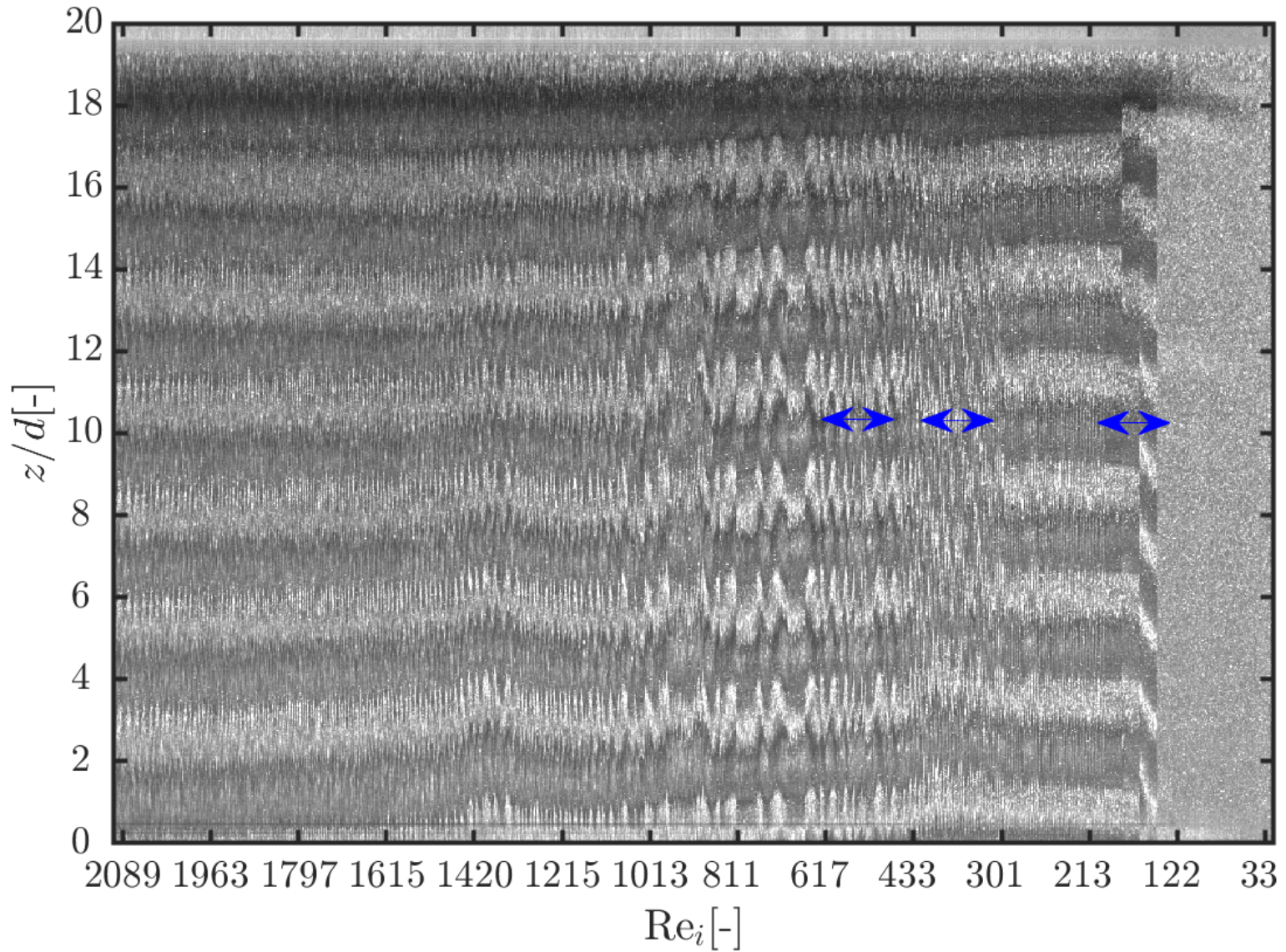


**Figure 4.9:** S-T plot for the entire QSDown experiment of  $\phi = 0.10$ . The x-axis has the Reynolds number from maximum value of cylinder rotation to rest (QSDown). The regions with interesting transitions are marked in blue arrows. The regimes from  $Re_i = 2089$  up to  $Re_i = 811$  have only transitions between MWVF and WVF and the region from  $Re_i = 811$  to  $Re_i = 617$  is an optical illusion, as when the region is zoomed, it shows standard WVF/MWVF. The red lines separating the quasi-steady experiments has been removed to better represent the image.

### 4.3.1. WVF to MWVF to MWVF + WSVF

Flow at the maximum shear rate is purely WVF. When the inner cylinder rotational frequency is reduced, the first regime transition that occurs is from WVF to MWVF. An additional temporal frequency arises that is characteristic of these modulations. This switching between MWVF and WVF occurs once more and the two-second S-T cuts of the region from  $Re_i = 617$  to 469 are shown combined in Figure 4.8a. The power spectra and S-T plot change between WVF and MWVF is similar to single-phase flow and is thus not shown here again.

First, the WVF transitions to MWVF with the development of a second frequency component, and this modulation is clearly visible in the S-T plot (Figure 4.8a) until  $Re_i = 498$ . The S-T plot of  $Re_i = 469$  has spirals which develop near the end of the experiment, shown zoomed in Figure 4.10. This could be an unstable transition as the spirals occur only in the latter half of the S-T plot, thus indicating the requirement of longer experimental run-times. This is considered as the transition to MWVF + SVE. Power spectra of these regimes do not give an idea about the transition as there are multiple peaks which are difficult to classify, as seen in Figure 4.11 where only the inner cylinder rotational frequency is labelled.

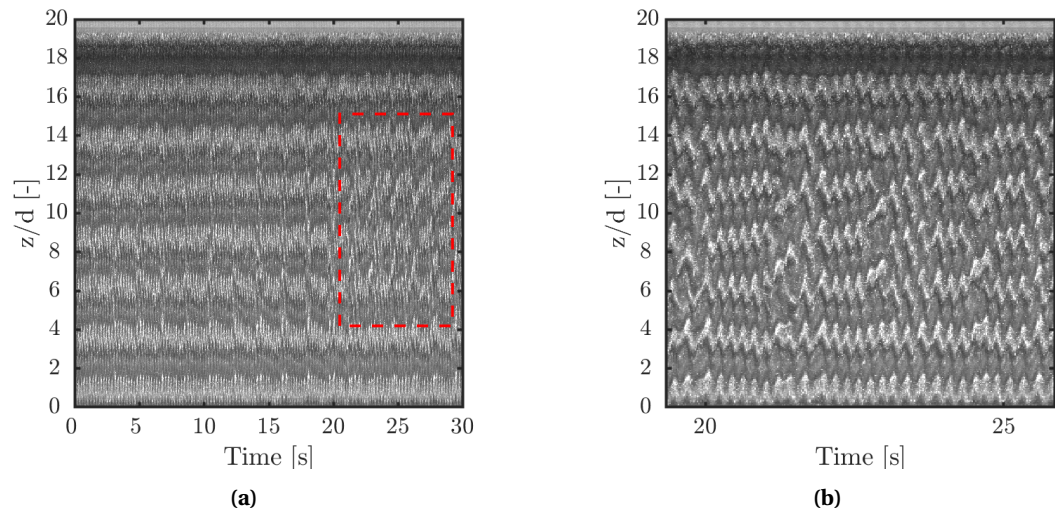


**Figure 4.10:** (a) S-T plot of MWVF + WSVF showing the wavy spirals forming in the latter half of the recording ( $Re_i = 469$ ). (b) A zoomed-in view shows how these spirals shift from one band to another

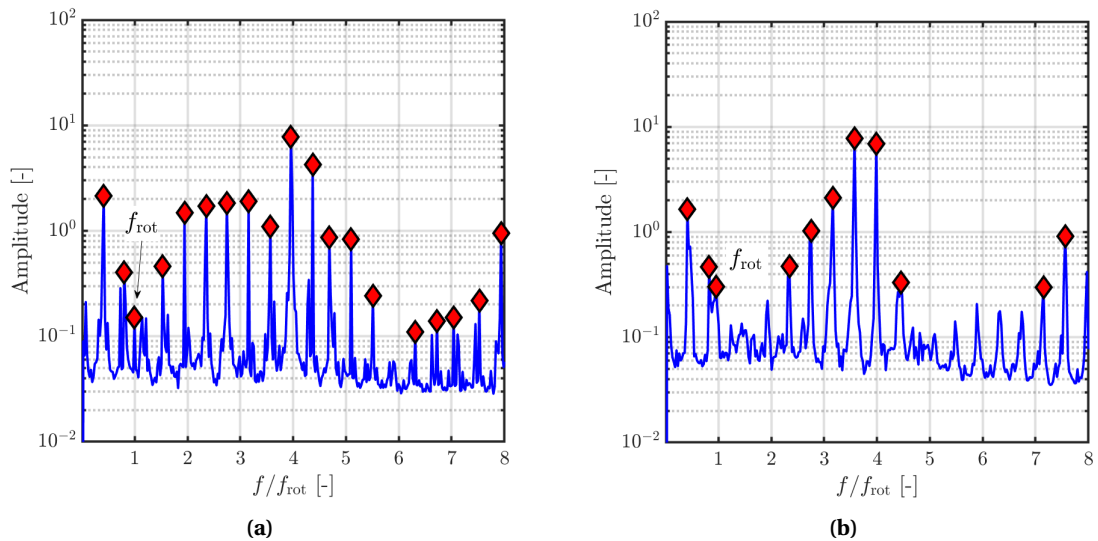


**Figure 4.11:** (a) Spectra of the regimes MWVF and (b) MWVF + WSVF. Multiple distinct peaks are present and the rotational frequency of the inner cylinder is labelled.

### 4.3.2. MWVF + WSVF to MWVF to WVF

From  $Re_i = 433$  to  $301$ , two transitions occur. First, the flow transitions from MWVF+SVF to MWVF wherein the spirals disappear and so the system goes back to MWVF. This is shown in Figure 4.12 where the differences in the S-T plots are prominent. The modulation present here is different compared to the earlier MWVF, where a secondary wave travelled over the primary wave resulting in a messy spectrum. Here, there is a second travelling wave with a low frequency  $f_2$ . The spectrum thus has a cleaner profile, as shown in Figure 4.13.

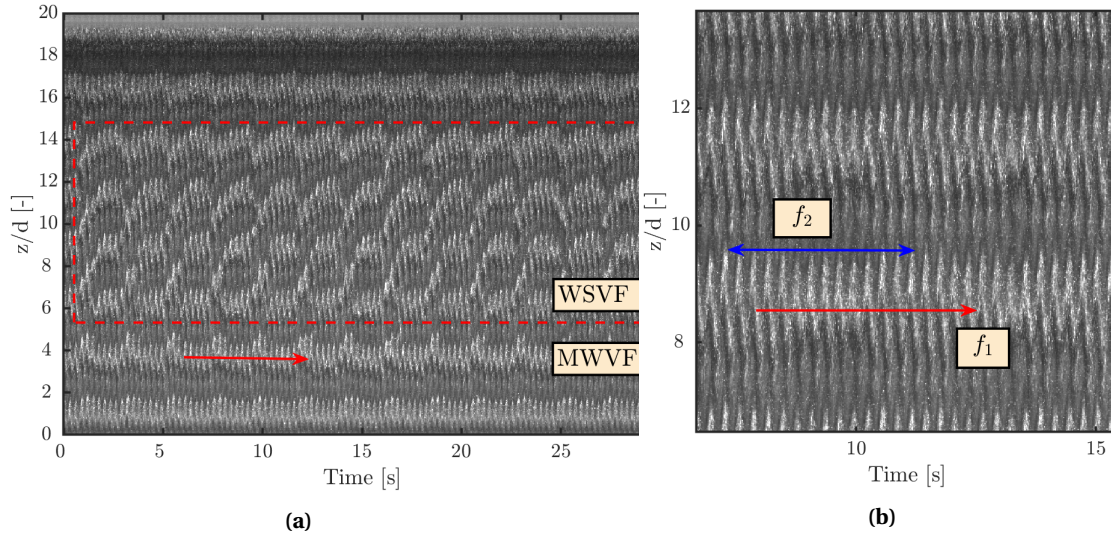


**Figure 4.12:** S-T plots of the (a) MWVF + WSVF ( $Re_i = 337$ ) and (b) MWVF (zoomed in to show the modulation,  $Re_i = 322$ ) regimes. The modulation is present in the form of second travelling wave, having a low frequency  $f_2$ .

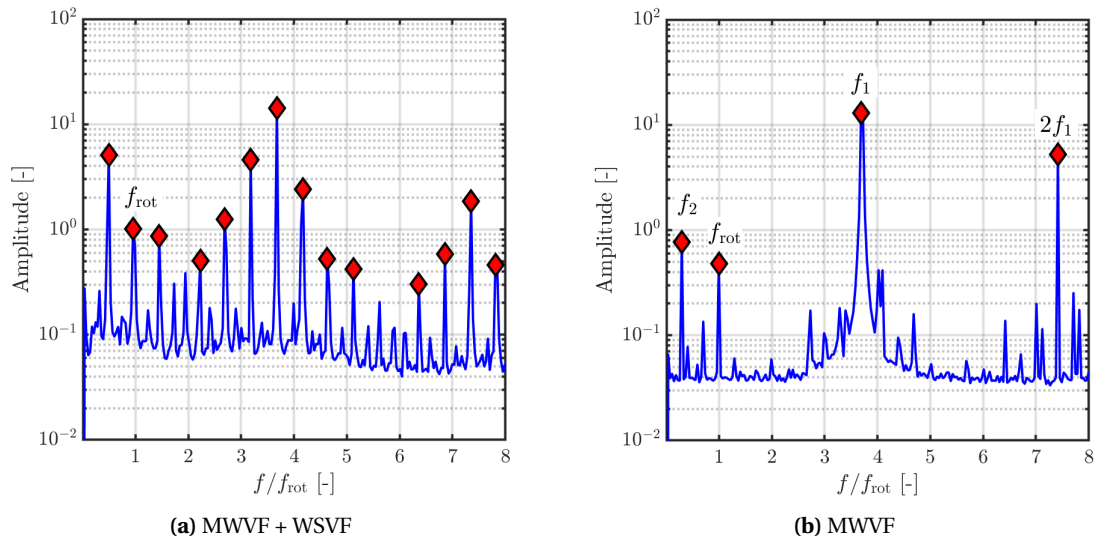


**Figure 4.13:** Spectra of the MWVF + WSVF (left) and MWVF (right) regimes. The new type of modulation shows a clear modulation frequency  $f_2$  over the primary wave frequency,  $f_1$ .

After returning to the familiar MWVF, the flow switches back to WVF, going back to having one dominant frequency component. This continuous back and forth between the modulated waves and pure wavy vortex flow indicates the sensitive nature of these flow transitions.

### 4.3.3. TVF to TVF + TW to TVF + SVF

From the WVF regime, the flow loses its waviness to form TVF similar to single-phase flow. This TVF has no temporal frequency but has a spatial frequency (wave-number) seen by the axial bands. The next transition is unique, where a travelling wave (TW) appears on top of the Taylor bands. From a cursory glance at the spectrum (Figure 4.15), this seems similar to SVF. Both have two dominant temporal frequencies with the same number of axial bands. These ‘travelling waves’ occur at the same points at which the spirals branch off from the Taylor vortices, as seen in Figure 4.14. They also have the same frequency as the spirals, which leads to the conclusion that these ‘travelling waves’ could be spirals which are beginning to form but are prevented from doing so as the TVF is more stable at that Reynolds number. When the Reynolds number was reduced from  $Re_i = 177$  to  $Re_i = 150$ , the spirals which were not forming in the TVF + TW regime stabilised and appeared across the whole axial section, with the exception of the top two bands.

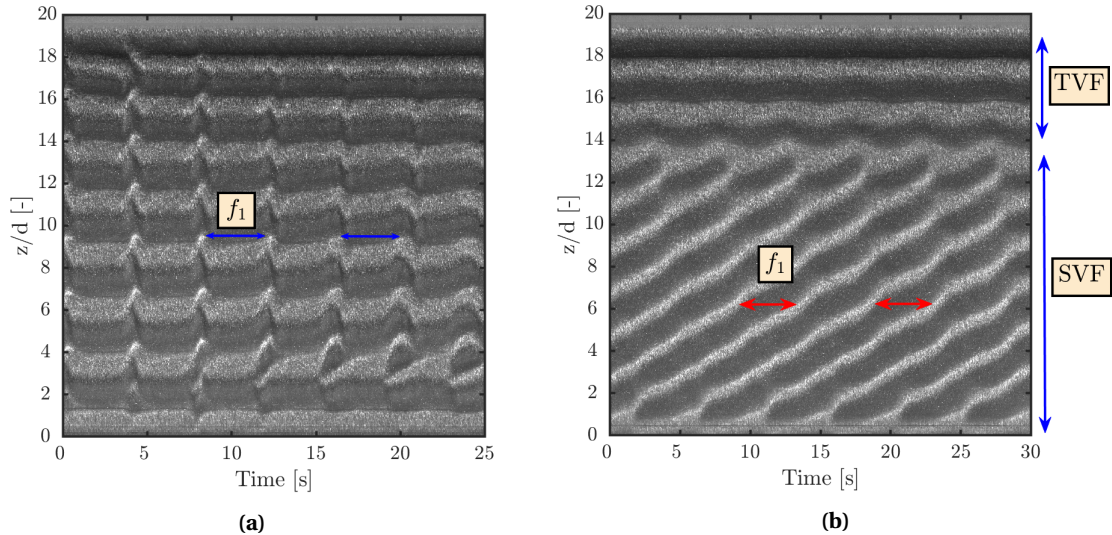


**Figure 4.14:** S-T plots of the (a) TVF + TW ( $Re_i = 177$ ) and (b) TVF + SVF ( $Re_i = 150$ ) regimes. The travelling wave disturbance has a frequency  $f_1$  in (a) which is similar to the frequency of the spirals’ occurrence  $f_1$  in (b)

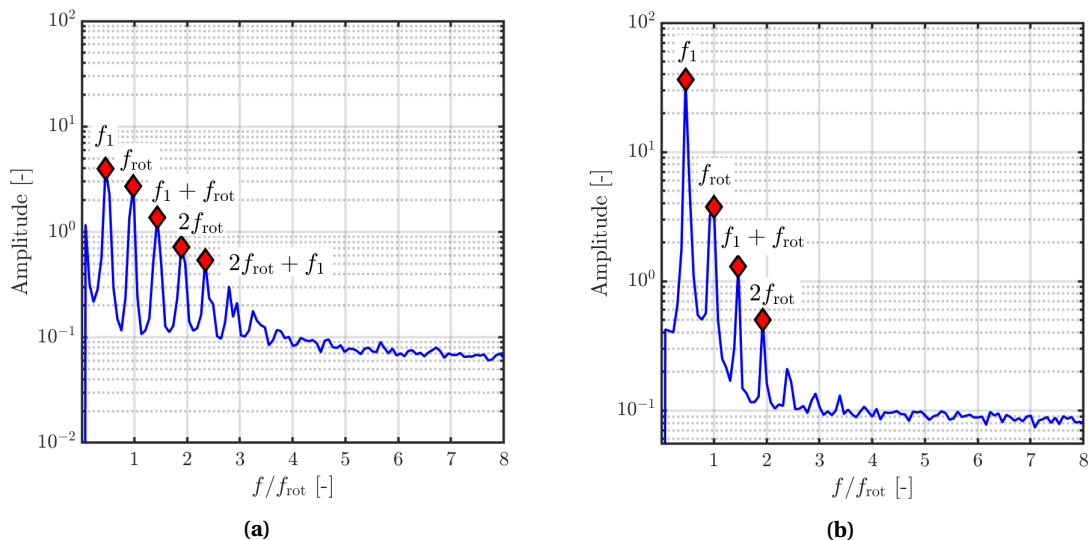


**Figure 4.15:** Spectra of the (a) TVF + TW and (b) TVF + SVF regimes. The travelling wave seems to have the same peak frequency in (a) as that of the spirals in (b), although much lower in amplitude.

The spirals have a frequency that is half of the inner cylinder rotational frequency, as seen in the power spec-

trum (Figure 4.15). The end effects from the top plate prevent the spirals from penetrating the top parts of the cylinder. Another reason for the non-propagation of the spirals into the top layer could be because the particles are slightly denser than the fluid in almost all the experiments. This could cause a lower concentration of particles at the top, thus making it more stable against spiral formation compared to the remaining axial sections of the cylinder.

#### 4.3.4. Transitions between wave patterns

For this case of  $\phi = 0.10$ , the change in the nature of waves can be observed from a frequency plot. The peak frequency identified from the power spectrum for each rotational frequency (normalised by the cylinder rotational frequency) is plotted against the Reynolds number. The changes can be seen in the form of steps, similar to the plot observed by Fenstermacher et al. [13], and the single-phase flow case. In the current setup, to additionally differentiate the obtained peaks, the amplitude of the peaks are considered by including them to be proportional to the marker size in Figure 4.16. The  $f_{\text{dom},1}$  name refers to the first peak value of dominant frequency obtained from the power spectrum. Figure 4.16 can be broken down into five separate regions and change between each is explained below. Even though the experimental direction is from right to left, the wave pattern changes are explained in regions from left to right.

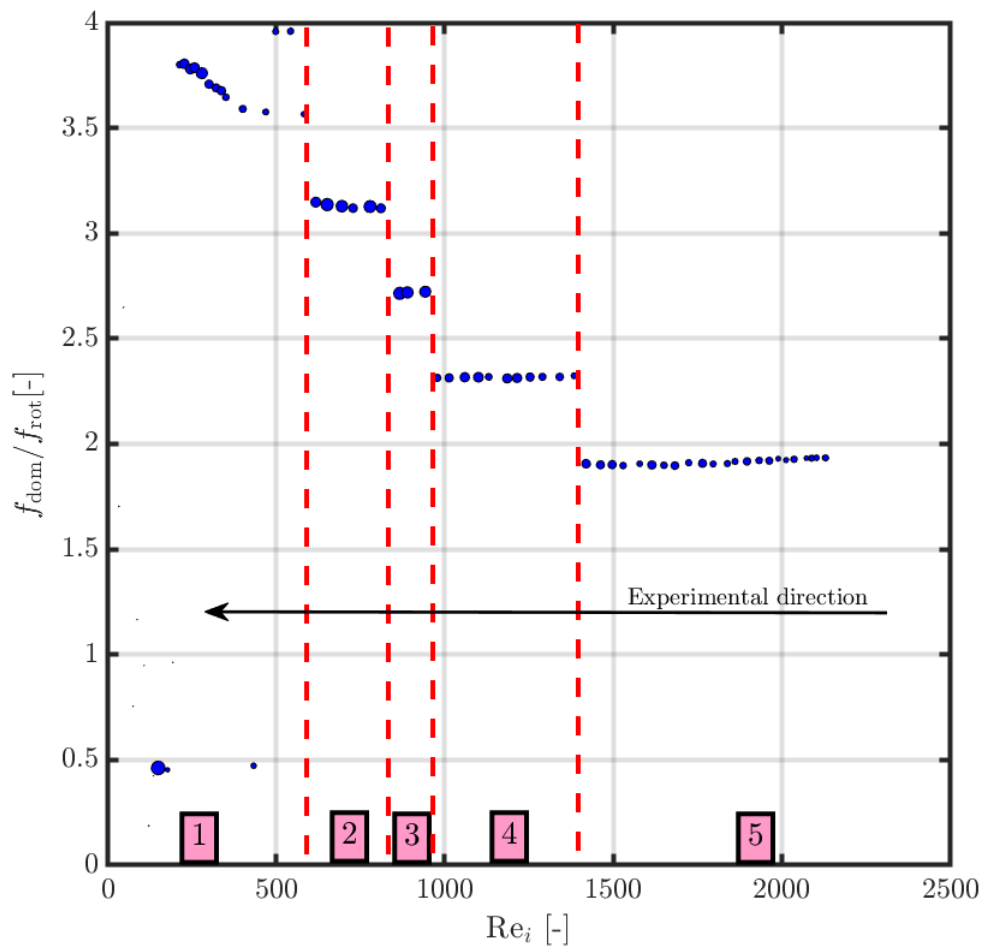


**Figure 4.16:** Variation of the normalised dominant frequency (first peak from power spectrum) with the Reynolds number. The plot is divided into five regions to understand the step change in value better. The marker size is proportional to the amplitude of the normalised dominant frequency  $f_{\text{dom},1}/f_{\text{rot}}$ .

#### 1 to 2

The first half of this region shows almost no markers, with an occasional point with relatively high amplitude. This is because the initial few points that are not visible are laminar and then due to the appearance of spirals, peaks are present which have low  $f_{\text{dom},1}/f_{\text{rot}}$ , but are relatively high in amplitude. The second half of '1' starts

from  $f_{\text{dom},1}/f_{\text{rot}} = 3.8$ , signifying the appearance of WVF. The value keeps reducing due to the appearance of spirals and unstable regimes, which also cause a drop in amplitude, signified by the smaller marker size.

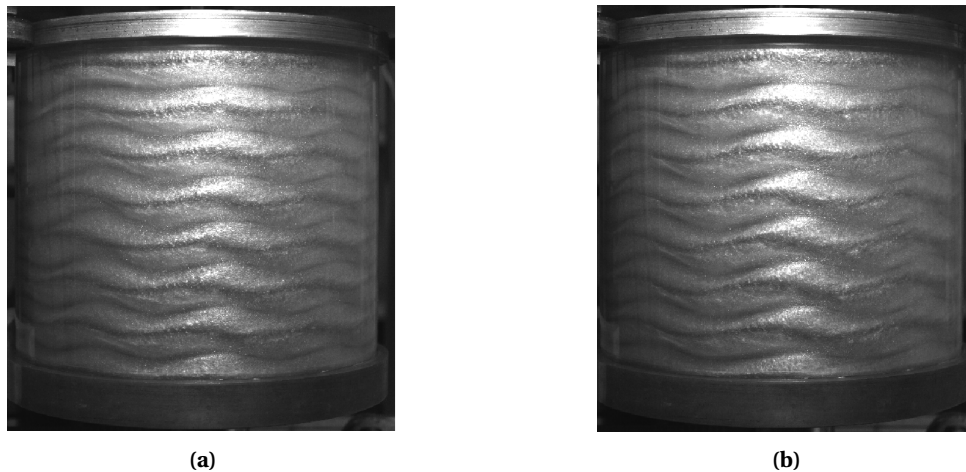


**Figure 4.17:** Snapshots of the TC system showing the change from (a) 9 azimuthal modulated waves at  $Re_i = 582$  to (b) 8 wavy vortices at  $Re_i = 617$

The shift from region '1' to '2' shown in Figure 4.17 is due to two reasons. Primarily, the regime changes from MWVF to WVF and this is accompanied by a decrease in the number of azimuthal waves, from 9 to 8. Not only does the regime change, but there is also an increase in azimuthal wave amplitude as the modulations disappear.

### 2 to 3

Region '2' has purely wavy vortex flow and the normalised dominant frequency ratio remains approximately the same. When a step down to '3' occurs, there is no regime change as the WVF is maintained. The reason for this change is fully attributed to the wavelength, shown in Figure 4.18, causing a reduction in the number of azimuthal waves from 8 to 7.



**Figure 4.18:** Snapshots of the TC system showing a reduction in number of azimuthal waves from 8 ( $Re_i = 811$ ) in (a) to 7 ( $Re_i = 866$ ) in (b) without a change in flow regime.

### 3 to 4

The shift between '3' and '4' is caused by the change of WVF to MWVF. The modulation which appears is axial, causing a phase difference between waves below each other, as seen in Figure 4.19. The appearance of modulations causes a significant reduction in wave speed, reducing the number of azimuthal waves from 7 closer to 5. The determination of the wavelength of modulated waves is not straightforward as only a few

snapshots of the system are captured. The absolute value of the waves should not be taken as a precise value, rather the qualitative inference is the result of this exercise.

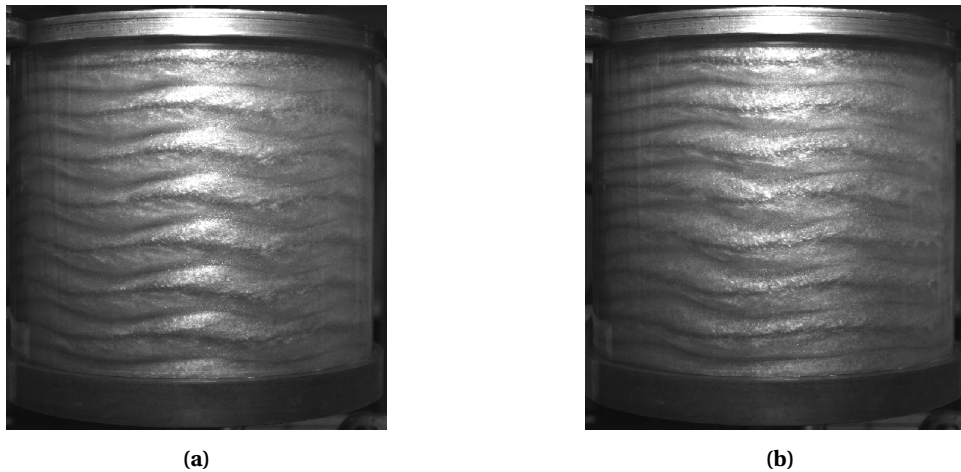


**Figure 4.19:** Snapshots of the TC system showing the change from wavy low wave amplitude flow (a) at  $Re_i = 942$  to a modulated high wave amplitude (b) flow regime at  $Re_i = 978$ .

#### 4 to 5

Within '4', the flow switches back to WVF and this is not observed in Figure 4.20. The shift from '4' to '5' is thus not associated with a change in flow regime. From the calculation of the azimuthal wavelength, no major change was identified in the number of waves. The reason for the change in dimensionless dominant frequency could be obtained in a finer analysis with more spatial data of the TC system.

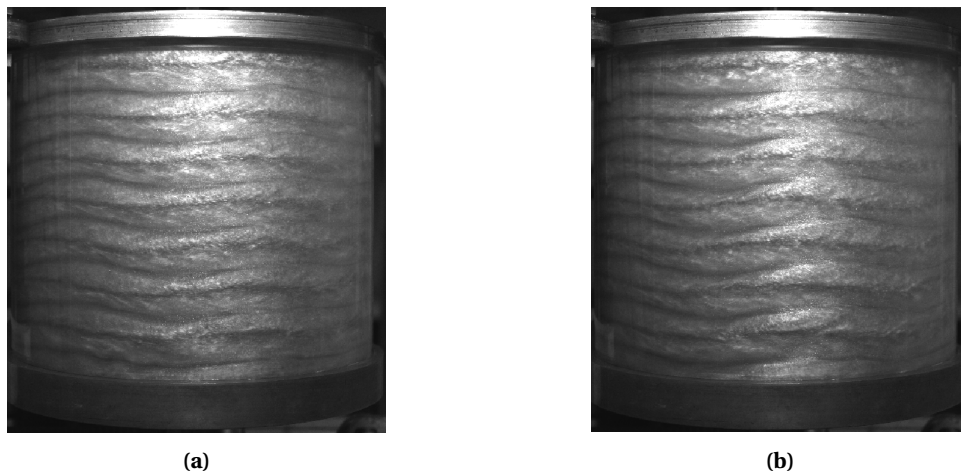


**Figure 4.20:** Snapshots of the TC system showing the change from '4' ( $Re_i = 1384$ ) to '5' ( $Re_i = 1419$ ) but with no visible change in the flow structures or number of azimuthal waves.

#### 4.4. Discussion on overall transition behaviour

The flow-map across all volume fractions summarising all the observed transitions is presented in Figure 4.21. As the volume fraction of particles is increased, the flow becomes more susceptible to an early onset of transition from laminar Couette flow. Multiple transitions that occur in the flow from laminar Couette flow till the time it stabilises to (WVF and MWVF). These include but are not limited to a combination of spirals, wavy spirals, interpenetrating spirals along with Taylor, wavy and modulated vortices. The reason for presenting the QSDown results is mainly because the particles are always well mixed in the system when coming down from a higher Reynolds number. During QSup experiments, if the fluid is lighter on a particular day (which is usually the case), the PMMA particles do not reach the top portion of the TC cell up to at least TVF. This might give a bias in the appearance of the first instability from rest.

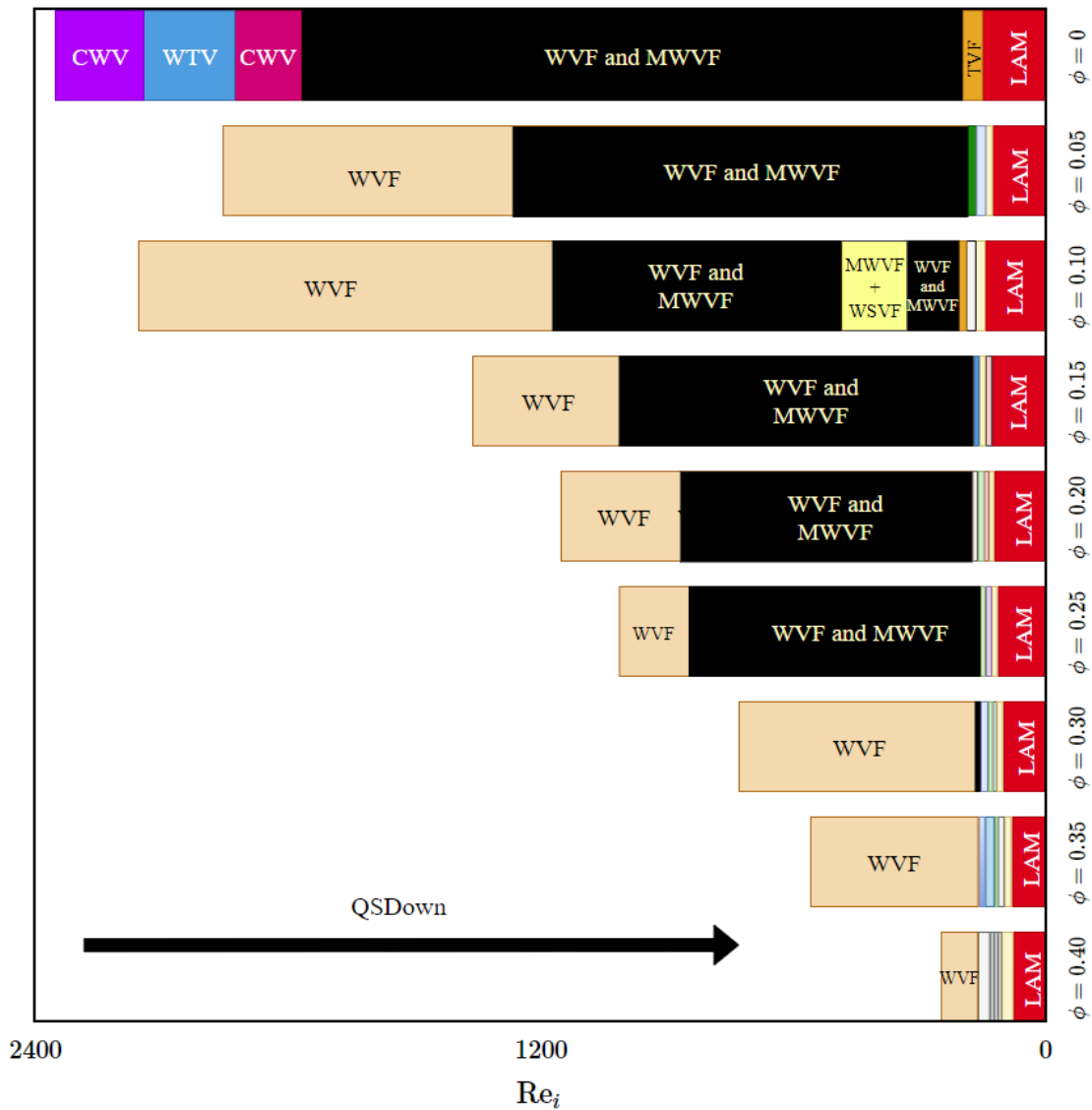


**Figure 4.21:** Complete flow map showing all the transitions across volume fractions (QSDown). The box sizes are scaled to the range of Reynolds numbers they last in the system. The non-labelled transitions after the first instability from ‘LAM’ are elaborated in Appendix B.

From Figure 4.21, the transition map covering the entire range of volume fractions are presented. As the particle loading is increased, the Reynolds number range covered also reduces due to the increase in the effective suspension viscosity and sensor measuring limits (torque sensor). The region marked as ‘WVF and MWVF’ should not be confused with the ‘+’ sign. The ‘+’ sign between two regime names indicates coexistence, like TVF+SVE. The WVF and MWVF region is the range of Reynolds numbers where there are multiple switches be-

tween the WVF and MWVF regimes. They cannot coexist (presence of a second frequency component makes it MWVF) and this classification is made to simplify the already information-heavy diagram. The transitions which are not labelled in the lower Reynolds number range consist mostly of spirals, riblets, wavy spirals and their combination. A detailed table containing all the transitions is presented in Appendix B. It is also interesting to note that the WVF is present for a longer range of Reynolds numbers as the particle loading is increased for the same range of compared values. The increased number of particles in the system seems to be almost removing the MWVF from the map, or it could be that the MWVF is triggered at much higher Reynolds numbers, outside the range of measurements.

#### 4.4.1. Destabilising effect of particles

The effect of particle loading on the  $Re_c$  in the flow map is presented in Figure 4.22, where the first onset of instability (from laminar flow) for all the flow regimes are plotted for QSDown. This is compared to the results obtained from the particle-laden experiments of [43, 44] and the takeaway is that there is a qualitative agreement between the studies and the current experiments. They also observed a reduction in the critical Reynolds number with an increase in particle volume fraction. A recent study by Gillissen et al. [65] also confirms this as they find analytically that a non-Brownian suspension is more unstable than a corresponding Newtonian fluid at the same effective viscosity. This confirms the fact that the effect of destabilisation is caused by the particles, not by an increase in effective suspension viscosity.

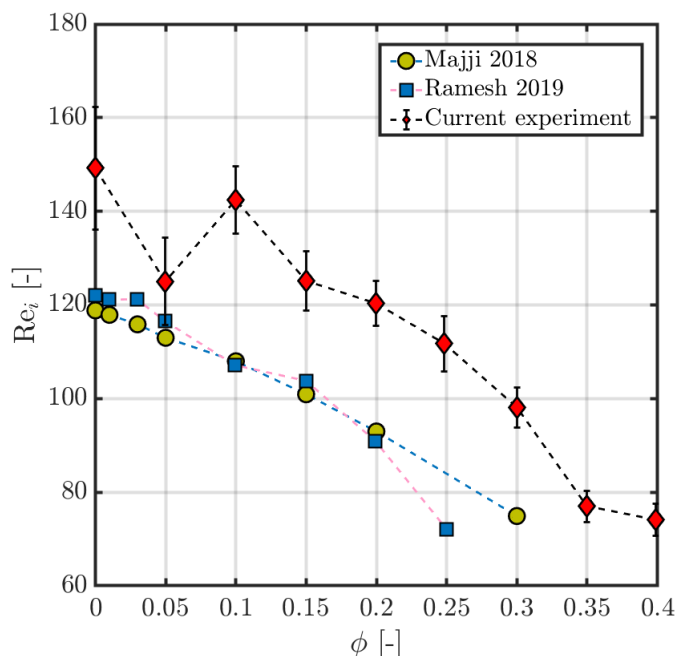


**Figure 4.22:** First onset of instability from Couette flow across all volume fractions with results also from Majji et al. [43] and Ramesh et al. [44].

However, for the current experiments, across the entire range of suspension and single-phase experiments, the critical Reynolds number seems to be higher in value. Possible reasons for the increase in this value are experimental conditions and errors. There were potential issues noticed with the temperature calibration that resulted in a bias leading to increased temperature readings. This bias induced increase in Reynolds number could be the reason for the difference in the appearance of the first instability from Couette flow. The reason for a reduced critical Reynolds number for  $\phi = 0.05$  is also unclear. Throughout the entire thesis, the extremely sensitive nature of Taylor-Couette flow and its dependence on the experimental history and conditions has been observed to play an important role in the results obtained.

#### 4.4.2. Effect of short experimental time

Even though the quasi-steady experiments were conducted, the acceleration of the cylinder rotation between rotational frequencies is very high. The flow is dependent on the history of the system, i.e., how the flow

state was obtained. For example, Xiao et al. [11] found that the acceleration rates affected the wavelength, speed and Reynolds number relation. To ensure that the system remained free of memory effects, they gave 2 hours after acceleration to record a data point and 1 hour between experiments. The experimental protocol followed by [43] was to accelerate the system to the desired rotational frequency and holding it at that state for a long duration. In the present experiments, each reading is held for 90 seconds and the S-T recording is made during the last 30 seconds of the 90-second measurement. The reasons for a shorter measurement were two-fold. Primarily, the condition for convergence of torque for single-phase flows was satisfied, which is elaborated in section A.3. Secondly, to cover a wide range of Reynolds numbers, a shorter measurement duration was worthwhile for practical reasons of time consumption and data processing. The key takeaway from the experiments is the fact that most of the regimes seen by [43] and [44] were observed in the current system. The appearance of these regimes, however is not in a well-defined sequence. The flow in the current TC system is highly sensitive, with some cases of multiple regimes competing for stability. An example of such a case was shown earlier in the transition for MWVF + WSVF, wherein the wavy spirals did not occupy the whole axial section.

#### 4.4.3. Ribbon and spiral formation dependence on particle loading

An interesting point to note is that riblets (also called ribbons), which were observed by Majji et al. [43], were not fully seen in the QSDown experiments. Majji et al. [43] found that for  $\phi = 0.10$ , the riblets took 13 min to form in the full annular length and that the fully developed riblets were seen 30 min into the transient experiment. In their quasi-steady experiments, the riblets took a long time to establish its pattern. This could be the reason why the riblet regime is not vividly visualised, with only partial riblets seen, as shown in Figure 4.23 for  $\phi = 0.15$ . These are still classified as unstable/ IPS as the mechanism for the formation of riblets is proposed by Majji et al. [43] as the combination of L and R mode spirals (Left and Right mode spirals respectively). These are spirals that are classified based on the direction of inclination, and both types are seen in the current experiments. Ramesh et al. [44] did not observe the formation of riblets and since the radius ratio of that experiment is closer to the current system, there is a possibility of geometrical dependence on the formation of riblets.

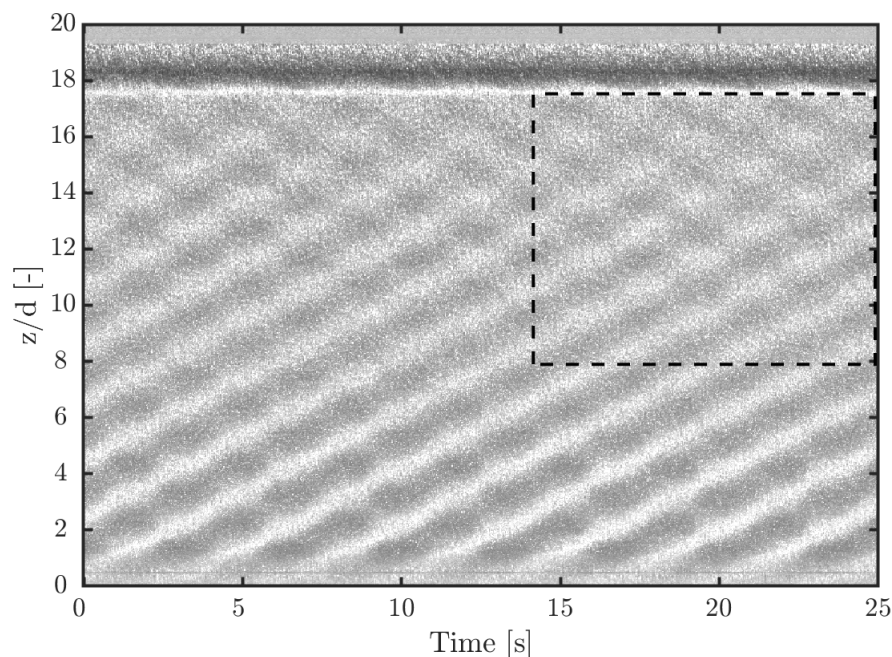


**Figure 4.23:** Partial riblets seen in the S-T plot of  $\phi = 0.15$  at  $Re_i = 125$ .

The types of spirals observed are shown in Figure 4.24. In the lower volume fractions, the R-type of spirals are the dominant mode as the first appearance of the L type occurs only at  $\phi = 0.15$ . This is also where the first occurrence of riblets is spotted, which makes sense as both types seemingly combine to form riblets. The coexistence of the R and L type of spirals is noticeable until  $\phi = 0.25$ , where, in one case the spirals alternate in an R-L-R fashion along the axial section, shown in Figure 4.24.

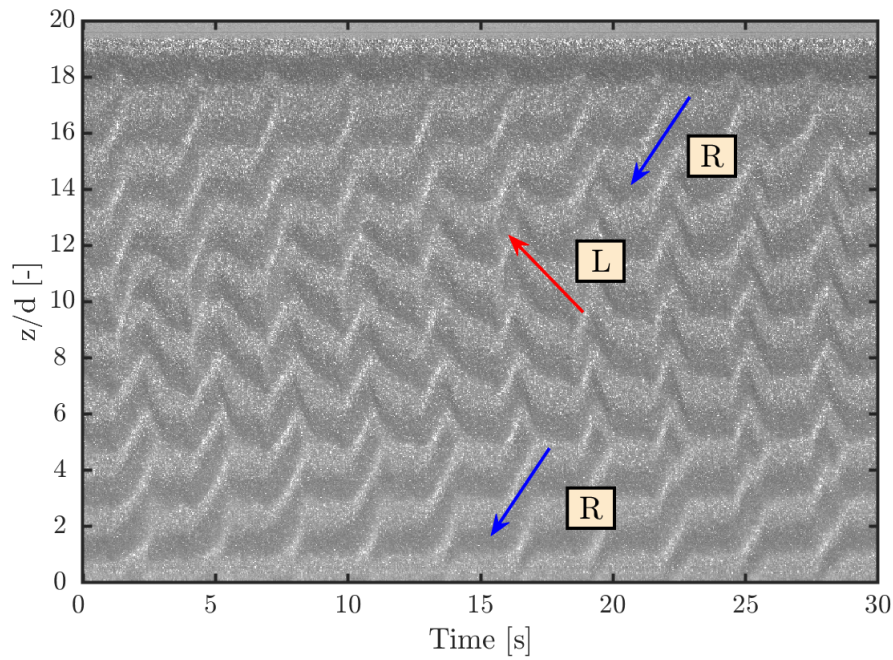


**Figure 4.24:** S-T plot of  $\phi = 0.25$  at  $Re_i = 134$  showing the coexistence of both L and R type spirals, with the inclinations indicated by the arrows on the figure.

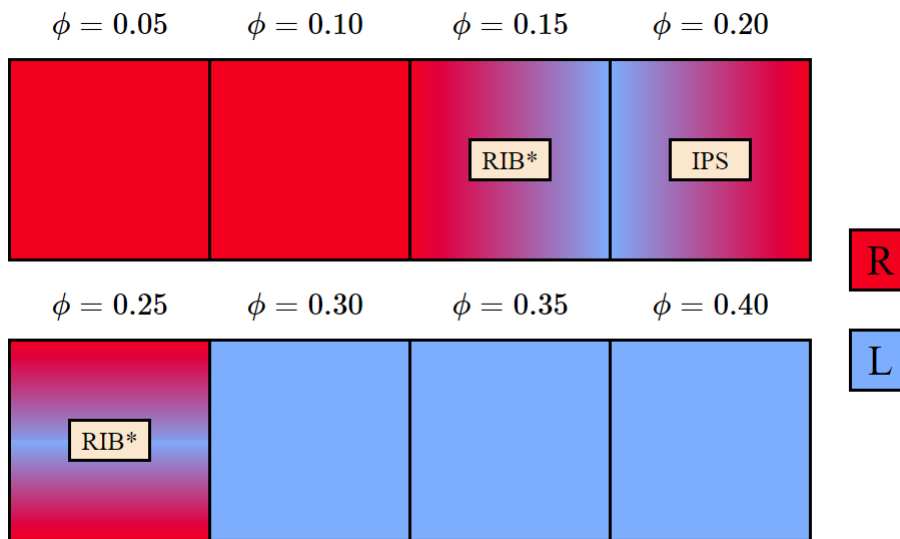


**Figure 4.25:** Graphical representation of the types of spirals that appear in the experiments. The lower particle loading range is filled by R-mode spirals (red) and then the appearance of the L-mode (blue) causes the formation of Riblets (\* indicates partial) and IPS. Beyond  $\phi = 0.30$ , only the L-mode persists.

The appearance of spirals across all volume fractions is graphically represented in Figure 4.25. This clearly shows that the IPS and riblet regimes occur only when the L-type spirals enter the system. For volume fractions higher than  $\phi = 0.30$ , there are no more R type spirals present, and there are also no riblets seen. The reason for the disappearance of the spirals is not known, but at the same time, the visualisation for the highest two volume fractions is also poor in quality, as there are too many particles in the system. The increased particle-particle interactions at the higher particle loading cases could affect the way the spirals are formed, but this is conjectured based on observed results. A deeper analysis of the spiral formation theory could help provide some insights to support the claims. Nevertheless, the observed spectra and S-T plots for all the volume fractions give a good overall idea about the transitions that exist in the current Taylor-Couette facility.



# 5

## Conclusions and recommendations

Flow visualisation experiments were performed in the Taylor-Couette system for both single and multiphase flow. The effect of particle loading was studied on the flow transitions and the major conclusions of this report are summarised in section 5.1 while the recommendations for future work are presented in section 5.2.

### 5.1. Conclusions

- The critical Reynolds number at which the flow transitioned from laminar Couette flow to TVF was compared based on torque and flow visualisation. The **order of transitions qualitatively matched** prior experiments performed in literature, but the range of values in the current experiment were found to be higher. This was attributed to the temperature estimation error that could have given a bias in the viscosity values, thus causing a Reynolds number error.
- The various regimes were classified first by constructing Space-Time (S-T) plots, from which a spectral analysis gave the distinct temporal and spatial frequencies of a measurement. A **flow map was constructed** and the effect of hysteresis was also described. **Hysteresis affects the nature of transitions** significantly, as there were changes in the order of regime appearance and torque values. The coarse nature of the experimental steps in the rotational frequency of the inner cylinder and lack of temperature control proved to be limiting factors in conducting a deeper hysteresis study.
- In chapter 4, the effect of particle loading on flow transitions was studied. PMMA particles were utilised and a neutrally buoyant suspension was prepared. The **addition of particles** resulted in an **earlier onset of transition from laminar Couette flow**, characterised by the reduction in the suspension viscosity based Reynolds number,  $Re_c$ .
- The second effect of particle addition was the **emergence of non-axisymmetric flow structures** that were not observed before for pure inner cylinder rotation. The results of the particle-laden suspension experiments were compared to the recent similar suspension experiments- Majji et al. [43] and Ramesh et al. [44] and there was a **qualitative agreement in the appearance of these non-axisymmetric regimes**. In the current experiments, multiple cases of **coexisting regimes** were observed. This was attributed to the flow not getting sufficient time to stabilise as the measurement time was kept short to cover a wide range of Reynolds numbers.
- At higher particle loading ( $\phi > 0.15$ ), **two types of spirals** (L and R mode) seemingly combined to form ribbon structures, albeit partially. This regime was observed by Andereck et al. [16] for counter-rotating cylinders and Majji et al. [43] for suspension experiments. The nature of the spiral modes changed from R to the L type at the highest volume fractions, indicating a **possible dependence of the spiral nature on the particle loading**.
- The complexity of the flow system at higher particle loadings made it **difficult to extract extensive quantitative information** based on a single view of the system for short measurement times. The visualisation also dropped significantly in quality at the highest cases of particle loading. However, the information extracted from the S-T plots has given a **good idea about the nature of flow transitions** in a Taylor-Couette system with particles.

## 5.2. Recommendations

The current experiments covered a wider range of Reynolds numbers not studied before and the interesting nature of results does not come without possible improvements to the experiment and analysis.

### 5.2.1. Experiment

- The temperatures determined throughout the experiments were not satisfactorily calibrated, which could have caused the higher range of Reynolds numbers in single-phase flow. Due to the sensitive nature of the viscosity to temperature changes, the TC system could greatly benefit from a temperature-controlled lab environment.
- Better quality of particles could help in achieving good neutral buoyancy. The difficulty in the preparation of a neutrally buoyant suspension was due to the poly-disperse particles, compounded by the presence of voids, which caused them to float.
- The motor-torque sensor- acquisition system did not achieve the target rotational frequencies and also developed a systematic error in the torque values. Updating this part of the setup could greatly increase the confidence in the measured values.
- The effect of different aspect ratios, radius ratios and gap widths on particle loading and flow transition provides a lot of potential for future research.

### 5.2.2. Analysis and methodology

- The Reynolds number range covered in the current experiments can be split into multiple campaigns. The main advantage of this is longer experimental times, where sufficient time could be given for the flow to stabilise, especially with particles.
- Multiple cameras can be used to construct the entire view of the TC system. This will aid in the determination of the azimuthal wave speeds and also give more information on the non-axisymmetric structures in suspensions.
- The effect of particle interactions is not studied in this report, mainly due to lack of available information (opaque flow). Using particle velocities/trajectories (from another technique, like ultrasound), the reason for the formation of these structures can be studied in detail.

# A

## Data processing and analysis

### A.1. Determination of the torque offset

The torque offset is calculated with the laminar reading as a base case. When the flow is still laminar, the torque follows a linear relation with the rotational frequency. Using this, the first few values of torque in all the experiments were fitted using a linear fit to obtain the y-intercept, shown in Figure A.1.

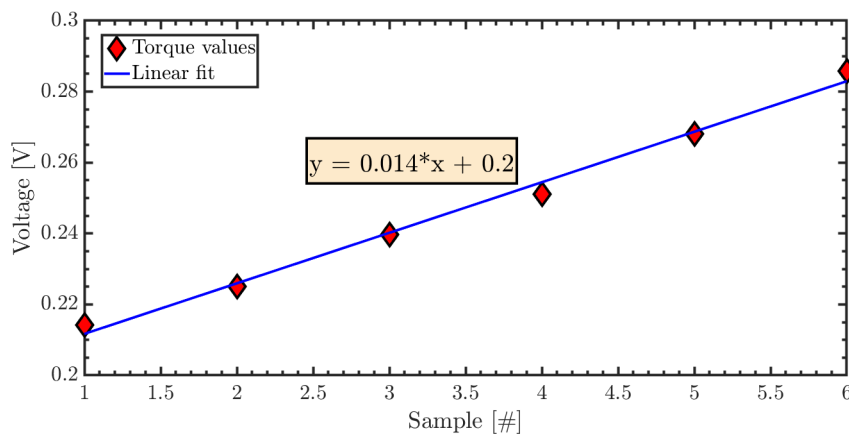


**Figure A.1:** The first few measurements of laminar flow are considered and a linear fit is used to obtain an offset, thus correcting for the offset error in the torque values.

The obtained y-intercept was used as a reference value at all the values were subtracted from it, essentially pushing the first value to zero. The Voltage is related to the actual torque value by a factor of 0.2 from the calibration of prior experiments. The torque sensor was not calibrated for the current measurements as the previous calibration was taken to be accurate.

$$T_{\text{actual}} = (T_{\text{experiment}} - T_{\text{offset}}) \times 0.2$$

### A.2. TTL signal processing for $f_{\text{in}}$ determination

The TTL counter gives a square pulse output with an amplitude of 5V for every 36 degrees of the cylinder rotation. This results in 10 pulses for each rotation of the inner cylinder. An FFT is performed across the raw TTL data, as shown in Figure A.2 to obtain the power spectrum in Figure A.3. The peaks represent ten times the actual inner cylinder rotational frequency and its harmonics. This is done for all the measurements as the system developed an error which caused it to output higher rotational frequencies than the input, shown in Figure A.4. In addition to this error, the DAQ also outputs very unreliable frequencies in the low end, thus not making it feasible to achieve a particular Reynolds number.

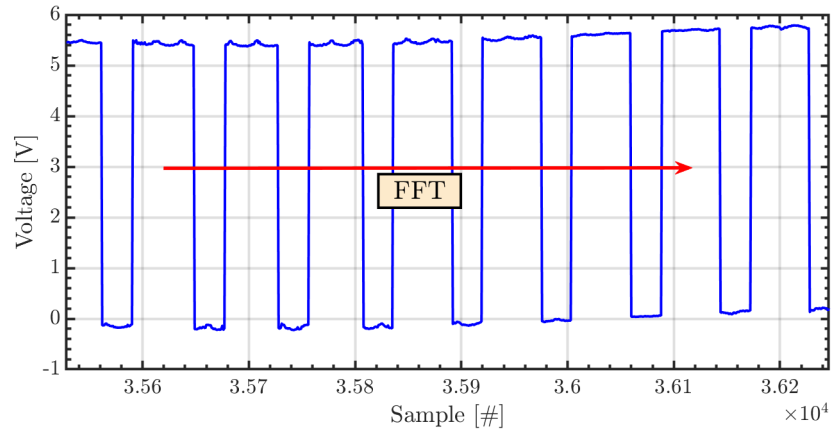


**Figure A.2:** Raw TTL signal, where each pulse corresponds to 36 degrees of the inner cylinder rotational frequency. An FFT is done across this TTL data.

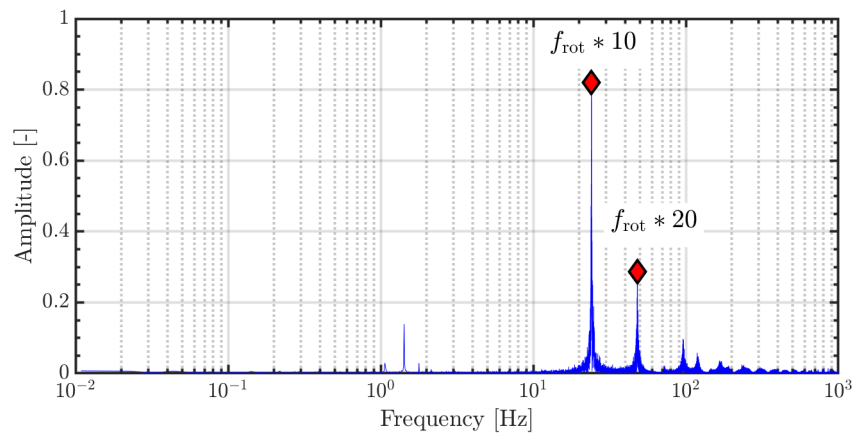


**Figure A.3:** FFT of the raw TTL data results in a spectrum with peaks that represent ten times the actual rotational frequency of the inner cylinder.

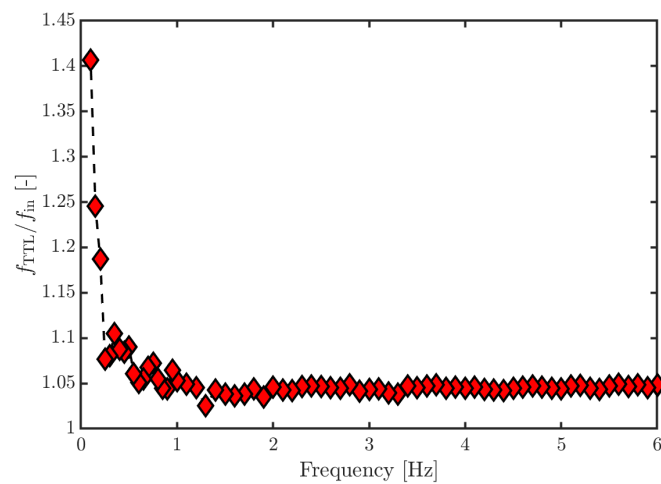


**Figure A.4:** The ratio of the actual frequency of rotation computed from the TTL data to the input vs the Reynolds numbers. Not only is the actual frequency of rotation biased on the higher side, it is poor in the lower frequency output, as the least count of the systems becomes a factor.

### A.3. Determination of experimental time - convergence of torque

To cover a wide range of Reynolds numbers, a compromise had to be made with the experimental duration. This duration was decided based on the time for the convergence of the mean torque values, similar to the procure followed in the particle size distribution.

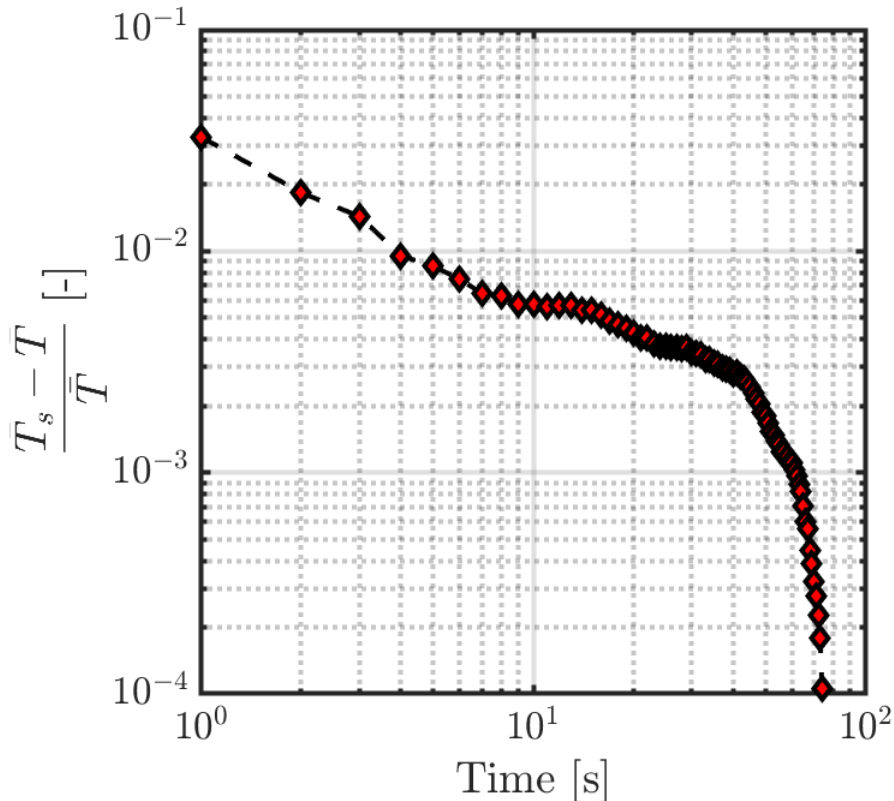


**Figure A.5:** Convergence of the torque value for a single measurement showing that the mean torque is converged to 1% of its true mean within 10 seconds. This is used to determine the 90 second measurement time for each rotational frequency.

From Figure A.5, the mean torque value is within within 1% of its true value very quickly, and close to 100 seconds, it each even reaches closer to 0.1% of the true mean. The measurement duration was thus set as 90 seconds, and the 30-second recording for making S-T plots was captured towards the end of this 90 seconds. Even with a shorter measurement time, a single QSDown case took close to 2 hours to complete.

### A.4. Determination of the wavelengths of wavy vortices

In the comparison of flow transitions, the changes in dimensionless temporal frequencies were sometimes attributed to a change in the number of azimuthal waves. The wavelength of the wavy vortices was used to determine the number of waves around the system in the azimuthal direction.

$$\text{Number of waves} = 2\pi r_o / \lambda$$

where  $\lambda$  is the wavelength obtained by comparing two crests of a single wave to the calibration image, shown in Figure A.6. Based on the number of '+' marks separating the crests,  $\lambda$  is found as the distance between the markers is 2 mm. As this method relies on manual identification of the crests/troughs, an approximate number of azimuthal waves is obtained by rounding off to the nearest integer.

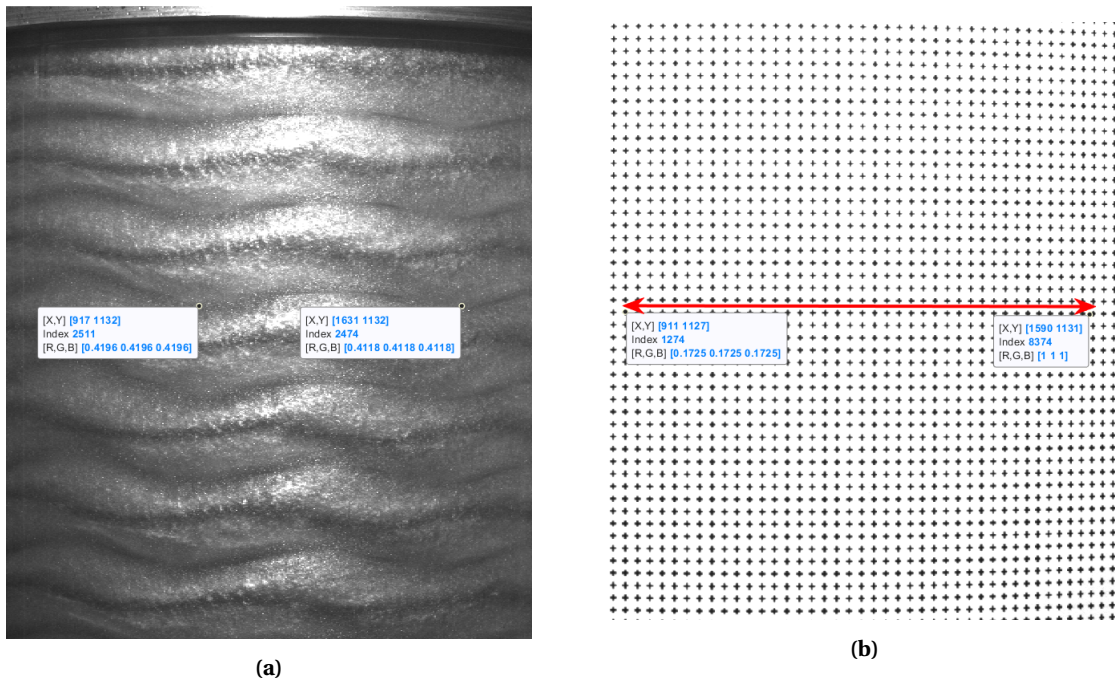


**Figure A.6:** Determination of the wavelength of the flow at (a)  $Re_i = 582$  at  $\phi = 0.10$  by comparing the snapshot to the (b) calibration image.

# B

## Multiphase flow regime classification

**Table B.1:** The order of transition in all of the particle laden suspension experiments (QSDown). The regions marked unstable and tentative are not clearly one or even two well defined regimes.

$\phi$ [-]	0	0.049	0.099	0.150	0.199	0.248	0.300	0.350	0.398
From rest	Laminar	Laminar	Laminar	Laminar	Laminar	Laminar	Laminar	Laminar	Laminar
	TWF	TWF+SVF	SVF+TWF	SVF	SVF+WSVF	Unstable	SVF	Lam+SVF	Lam+SVF
	WVF	TWF	TWF+ TW	WVF+SVF	TWF+IPS/SVF	IPS	IPS/ large MWVF	SVF/IPS	SVF
	MWVF	Unstable modulations	TWF	WSVF	SVF+WVF	TW	TWF+SVF	WSVF (tentative)	Lam+SVF+MWVF
	WVF	WVF	WVF	MWVF	TWF	WVF	TW+SVF	TWF+IPS/MWVF	SVF+MWVF
	MWVF	MWVF	MWVF	WVF	MWVF	MWVF	TW+MWVF	TWF+IPS+MWVF	IPS+MWVF
	CWV	WVF	MWVF+WSVF	MWVF	WVF	WVF	MWVF	WSVF+MWVF	TWF+SVF+MWVF
	WTW	MWVF	MWVF	WVF	MWVF	MWVF	WVF	WVF	WVF
	CWV	WVF	WVF	MWVF	WVF	WVF	WVF	WVF	WVF
		MWVF	MWVF	WVF	MWVF	MWVF	MWVF	MWVF	MWVF
		WVF	WVF	MWVF	WVF	WVF	WVF	WVF	WVF
		MWVF	MWVF	WVF	MWVF	MWVF	MWVF	MWVF	MWVF
		WVF	WVF	MWVF	WVF	WVF	WVF	WVF	WVF
				MWVF	WVF	MWVF	WVF	WVF	WVF
				WVF	WVF	WVF	WVF	WVF	WVF

# C

## Flow visualisation alternatives

### Stearic acid crystals, a suitable alternative?

One major issue faced when using these particles in mass fractions even as low as 0.1% was that in the case of water only tests, the particles ended up sticking to the walls of the cylinder and this worsened the image quality significantly. The whole system had to be disassembled as shown in Figure C.1 , C.2b and cleaned thoroughly to remove the particles.



(a) Inner cylinder



(b) Outer cylinder

**Figure C.1:** The disassembled setup showing the Iridin particles sticking to the wall surface

When preliminary tests were done on the TC system with water to test out the image quality, the Iridin particles stuck to the walls of the cylinder, making it cumbersome to clean and mainly it reduced the image quality significantly after a week of tests. In the hunt to find an alternative, the work of Borrero-Echeverry et al. [48] stood out as a good option. As the worldwide production of Kalliroscope particles came to a halt, alternatives to these particles were in demand. In the studies conducted by Borrero-Echeverry et al. [48], the options for flow visualisation in a post Kalliroscope world was the main subject matter. They found that the stearic acid crystals present in shaving cream gave very good visualisation for the flow and followed the large scale structures in the TC system.

A mixture of these particles was made containing the same chemical composition as the shaving cream used in Borrero-Echeverry et al. [48], and the structures were clearly visible for water only solutions. When this was added to the 60% glycerol water solution even in larger quantities, the visualisation was weak at best. Another point to note was that when added in larger quantities, the viscosity of the base solution lowered significantly due to the increased concentration of water in the stearic acid mixture. The Iridin particles

when added to the glycerol-water mixture did not stick to the walls of the TC system and so all the single and multi-phase experiments were done with Iridin particles. The stearic acid crystals are well suited for water and the visualisation is likely poor due to the refractive index of the crystals when compared to that of the glycerol water mixtures. The mixture prepared using standard Gillette shaving foam is shown in Figure C.2



**Figure C.2:** (a) Gillette shaving foam weighed in the required proportion (b) Prepared solution with the top layer of foam to be removed.

When the aqueous glycerol density matched solution was prepared, Iridin gave excellent visualisation and conveniently, the presence of larger quantities of glycerol prevented the Iridin from sticking to the walls and did not affect image quality even after weeks of testing.

# D

## Setup operation and intricacies

### D.1. Experimental protocol

#### Before the start of the experiment:

1. Switch on the camera, calibrate the lens with the light on.
2. Fill the fluid till it is seen in the ring and shear it up so that there are no particles settling at the bottom, this includes hand-rotating the outer cylinder.
3. Keep the input files for camera, torque, IR temperature and ultrasound ready. Make sure there are no decimal point conflicts between the units used as the DAQ system accepts only commas to separate the whole number from the fraction.
4. Get the initial temperature for the system (PT100) using the offset file with the system in disable mode and save the offset file.
5. Check the fluid level once more after closing and get the offset for the rotation of the cylinder/s.
6. Start the experiment – simultaneously the temp (IR) and torque should be started.

#### During the experiment:

1. Ensure at periodic intervals to maintain the fluid level to prevent entrainment of air bubbles.
2. This frequency of fluid addition will increase with rotational speed.
3. Do not place objects on the DAQ table or hit it as this will change the cylinder rotational offset significantly.

#### After the experiment:

1. When the experiment is stopped, immediately switch off the IR reading.
2. Check the final fluid temperature (PT100) and save that offset file.
3. Disable the system and turn off the camera and lights.
4. Cover the beakers containing the test fluid so as to not lose solution by evaporation.
5. Ensure that the camera lens cap is on.

Mention the link to the website and shaker model for sieving

## D.2. Preparation of the suspension and particles

### D.2.1. Suspension

The procedure for the solution preparation can be found in the Cospheric website and can be accessed from "[https://www.cospheric.com/tween\\_solutions\\_density\\_marker\\_beads.htm](https://www.cospheric.com/tween_solutions_density_marker_beads.htm)". The required quantities of glycerine 1.23 and distilled water are combined in a beaker. This is stirred till no density currents are visible in the beaker. Ensure that the stirring velocity is not too high to prevent trapping air in the solution. Tween-20 is added (0.1g per 100 ml of solution) to the heated aqueous glycerine mixture (50-70°C) and this is stirred for 20 minutes. The solution can now be added to the TC setup directly or with Iridodin.

### D.2.2. Particles

The PMMA particles from Goodfellow are poor in quality after checking with a size distribution check from the micro-lab microscope. The size range is better with sieving, for which a sieve range of 560-600  $\mu\text{m}$  is used along with the shaker, shown in Figure D.1.

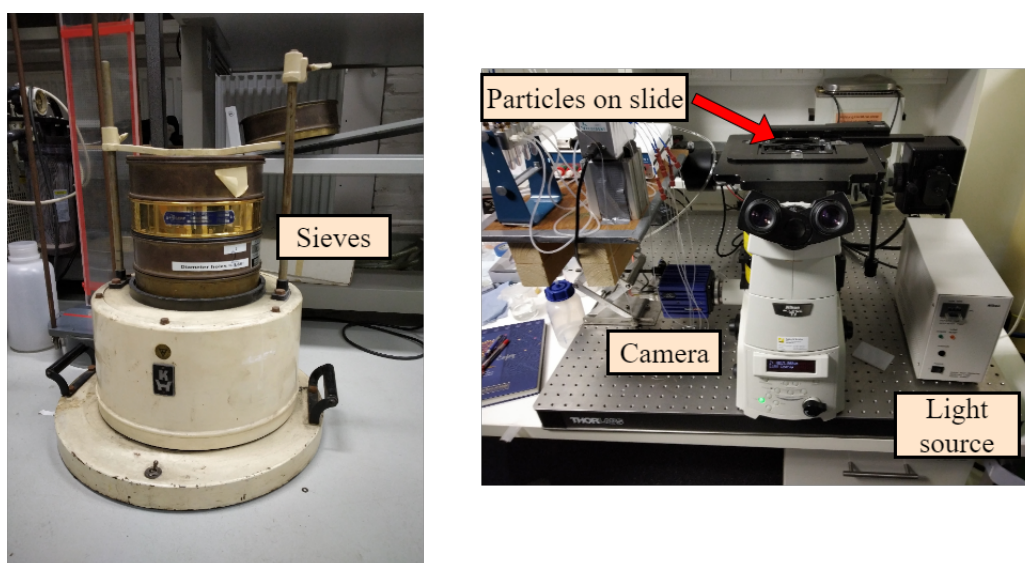


**Figure D.1:** (Left) Shaker with the 560  $\mu\text{m}$  sieve to filter out smaller particles. (Right) The microscope setup used to obtain images for determination of particle size distribution.

To determine the particle size distribution, the particles are analysed using the microscope present in the micro-lab. Small amounts of particles are placed on a glass slide, held by cellophane tape. A mercury lamp can also be used as the light source if the background illumination is insufficient. The background lighting was sufficient for the PMMA particles and the sizes had to be determined manually due to the presence of voids and irregularities in the particles.

After the sieving, the "bad" particles have to be removed. This "badness" is caused by the presence of voids in the particles, causing a lot of them to float in the prepared neutrally buoyant suspension. First, the at least twice required amount of particles are added to a buffer solution of the suspension and stirred for 5-10 minutes. The mixture is allowed to rest for 20-30 minutes after which the top layer of particles are removed. The good particles in the mixture are then removed from the mixture in a sieve and washed. The required amount of particles \*1.3 (to account for the weight of the water) are added to the TC system, thus facilitating the variation of particle loading.

## D.3. Maintaining neutral buoyancy in spite of global warming induced heat-waves

The recent heat wave across Europe saw temperatures in Netherlands increase to record highs. This had a significant effect on the lab ambient temperature, and in turn the setup. Across the weekend, the temperature difference was as high as 20 degrees during the day. This causes the density to vary and so the particles are

not neutrally buoyant, shown by the variation of the particle to fluid density ratio in Chapter 4. The only method to avoid this is to have temperature control, or keep a keen eye on Buienalarm and hope for uniform temperatures for a week. Not unlike climate change, these errors are inevitable and only drastic changes can offer a path to resolution of the long standing issues.

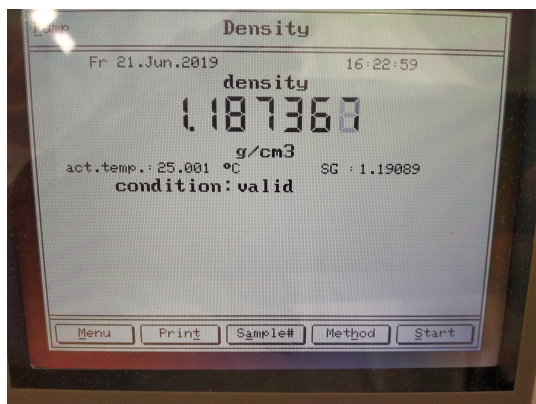


**Figure D.2:** Density meter reading of the working fluid (without particles).

During the addition of wetted particles to the system, water also entered the system, causing a significant change in the suspension density. The density of the solution was measured at the start of every experiment with the help of an Anton Paar density meter (DMA 5000, shown in Figure D.2) and the necessary amount of glycerine was added to maintain suspension density.

#### D.4. Temperature calibration of lab sensors

These images are included to give an idea of some details that were unmentioned in earlier sections. In Figure D.3, the calibration that was done for the PT100 sensor with boiling water is shown. This image clearly demonstrates the need for improved calibration of the sensors. All the sensors displayed different temperatures and since the temperature source for comparison is also not standardised, this procedure has to be redone with a well known reference temperature. The temperature bath in the viscometer is supposed to be well calibrated and that could be used in future tests.

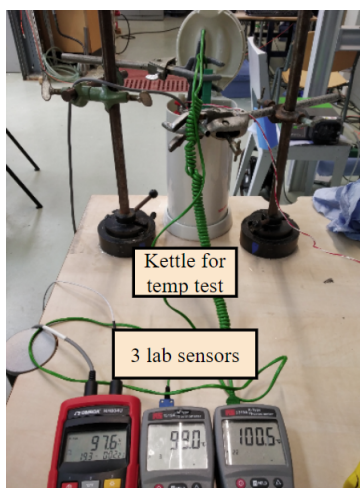


**Figure D.3:** Temp calibration for the PT100 sensor with boiling water. Other sensors from the lab were used for reference.

### D.5. Setup disassembly

The coupling between the cylinder shaft and the motor (and torque sensor) is very sensitive and prone to damage. This is shown in Figure D.4, where the claw coupling and two screws are labelled. The rubber coupling was replaced twice during the course of the current experimental campaign. New couplings can be manufactured in the lab and when holes are punched in the mould, care should be taken to make it loose fitting (not too loose) so that there is room for the shafts to compensate for eccentric mounting. When the torque readings show wild fluctuations or when the system screams out in agony,

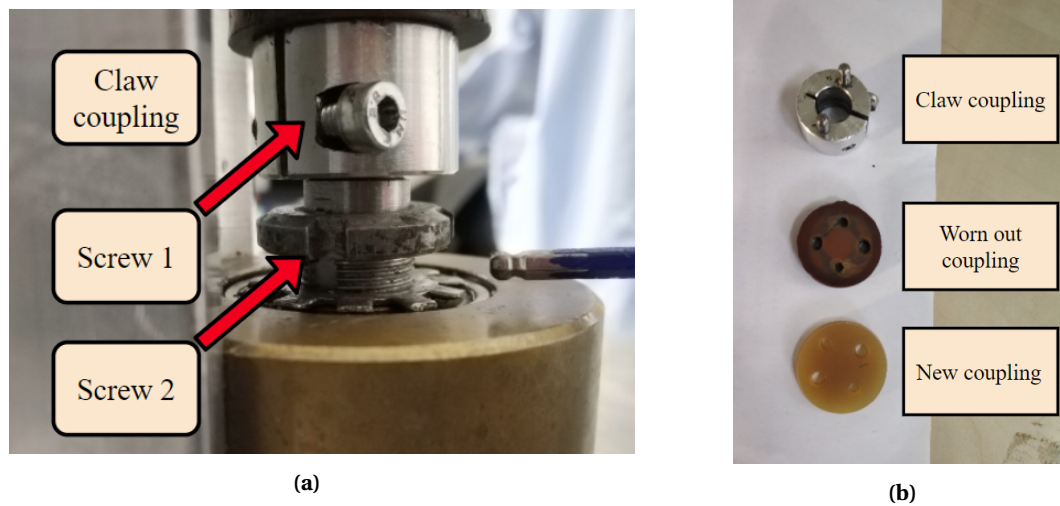


**Figure D.4:** (a) Coupling connections connecting the inner cylinder shaft to the motor and torque sensor (b) The most part likely to wear out is the rubber coupling, which was replaced twice in the current experimental run

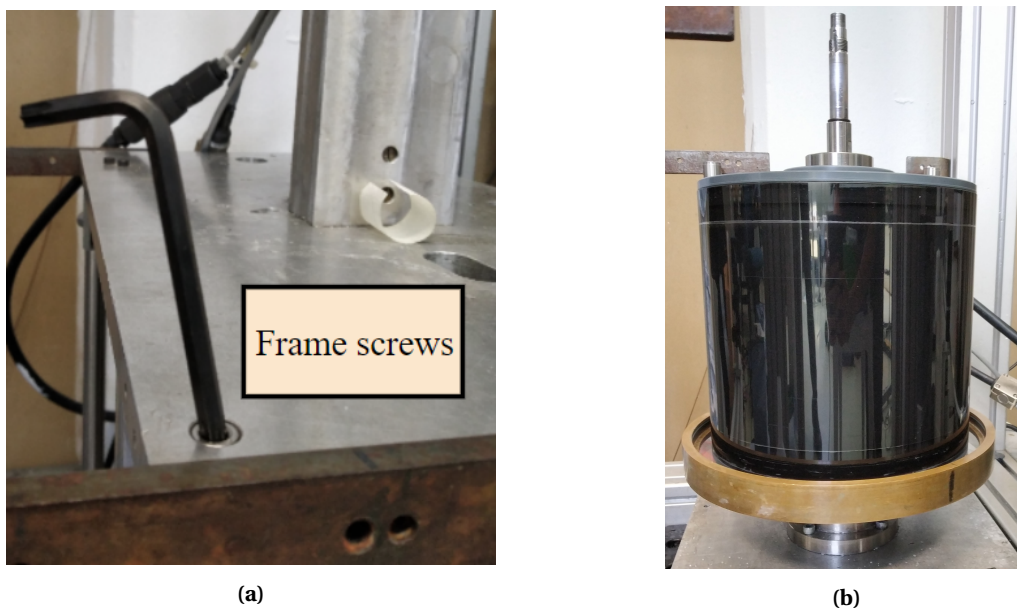


**Figure D.5:** (a) Screws to be loosened to remove the frame of the TC system (b) The TC setup after the removal of the frame and outer cylinder.

- The first step is to loosen the coupling connecting the motor to the cylinder shaft. If this is not done before removing the fluid, the whole cylinder hangs on the motor coupling and this can cause damage to the system. See Figure D.4. Screws 1 and 2 have to be loosened for this.

- Remove the fluid from the TC system. This can be done quickly with a peristaltic pump.
- Loosen the supports of the frame so that the whole top portion containing the motor and torque sensor can be removed. Place it safely on a support by the side, not directly on the ground. See Figure D.5.
- Remove the outer cylinder first, then the inner cylinder. The inner cylinder might be tougher to remove due to a seal formation by the fluid at the bottom. Remove with some force if necessary but keep the base supported at all times.

The assembly process can be derived from the above steps, just in reverse order. Make sure that all the screws are tight and that the coupling connections are proper. The placing of the frame on the TC system is the most important step. Care has to be taken so that the shaft passes through the housing such that the outer cylinder is not moved from its position. To create a proper seal between the base and outer cylinder, all the O-rings and edges are lubricated with Vaseline. If the outer cylinder is dislodged from its fixed position, fluid will leak from the edges when the system is filled up which can be very tedious to clean if glycerine is used as the working fluid.

## D.6. Miscellaneous setup images

These images are included in this report to give future TC experimentalists an idea of the system operation with the synchronised imaging and ultrasound measurements. The setup is also shown in Figure D.6. The outer cylinder is held in place by a wooden stop and this is checked before the start of every trial. The filling hole for the fluid is also tightened before the start of every experiment. As more particles are added to the system, the screw threads become jammed by particles, so care has to be taken when filling particles. The filling hole screw is also periodically cleaned to ensure smooth tightening.

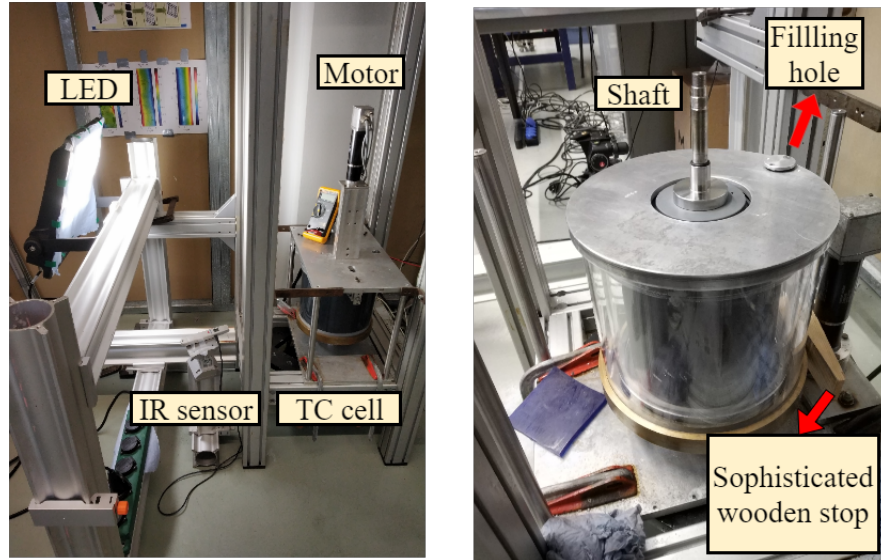


**Figure D.6:** Images of the setup with the labelled components. The filling hole is held in place by a screw.

Measurements were simultaneously performed by three separate techniques: imaging, torque and ultrasound. The imaging system is remotely controlled by the Dell 7577 and the torque system does not need monitoring once the experiments are started. The ultrasound measurements were performed by Amitosh up to  $\phi = 0.175$ , beyond which the data quality was too poor for proper analysis. A snapshot of this in action is shown in Figure D.7.

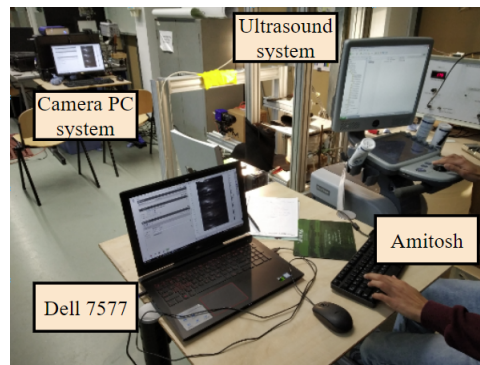


**Figure D.7:** Synchronised imaging measurements controlled by the Dell 7577 and ultrasound measurements performed by Amitosh.

# Bibliography

- [1] Russell J Donnelly. Taylor–couette flow: the early days. *Phys. Today*, 44(11):32–39, 1991.
- [2] G. I. Taylor. Stability of a Viscous Liquid Contained between Two Rotating Cylinders. *Philosophical Transactions of the Royal Society A: Mathematical, Physical and Engineering Sciences*, 223 (605-615):289–343, 1923. ISSN 1364-503X. doi: 10.1098/rsta.1923.0008. URL <http://rsta.royalsocietypublishing.org/cgi/doi/10.1098/rsta.1923.0008>.
- [3] R Lueptow. Taylor-couette flow. *Scholarpedia*, 4(11):6389, 2009. ISSN 1941-6016 1941-6016.
- [4] B. Haut, H Ben Amor, L. Coulon, A. Jacquet, and V. Halloin. Hydrodynamics and mass transfer in a Couette–Taylor bioreactor for the culture of animal cells. *Chemical Engineering Science*, 58(3-6):777–784, 2 2003. ISSN 00092509. doi: 10.1016/S0009-2509(02)00607-3. URL <https://linkinghub.elsevier.com/retrieve/pii/S0009250902006073>.
- [5] Arno Behr and Tobias Färber. Application of a Taylor-Couette reactor in homogeneous catalysis. *Chemical Engineering Transactions*, 43(Figure 1):835–840, 2015. ISSN 22839216. doi: 10.3303/CET1543140.
- [6] M. A. Fardin, C. Perge, and N. Taberlet. “The hydrogen atom of fluid dynamics” – introduction to the Taylor–Couette flow for soft matter scientists. *Soft Matter*, 10(20):3523, 2014. ISSN 1744-683X. doi: 10.1039/c3sm52828f. URL <http://xlink.rsc.org/?DOI=c3sm52828f>.
- [7] G. Chossat, P. Iooss. *The Couette-Taylor Problem*. Springer Science & Business Media, vol 102 edition, 2012.
- [8] E.L. Koschmieder. *Bénard cells and Taylor vortices*. Cambridge University Press, 1993.
- [9] S Chandrasekhar. The stability of viscous flow between rotating cylinders. *Proceedings of the Royal Society of London. Series A. Mathematical and Physical Sciences*, 246(1246):301–311, 8 1958. ISSN 2053-9169. doi: 10.1098/rspa.1958.0139. URL <http://www.royalsocietypublishing.org/doi/10.1098/rspa.1958.0139>.
- [10] Donald Coles. Transition in circular Couette flow. *Journal of Fluid Mechanics*, 21(03):385, 3 1965. ISSN 0022-1120. doi: 10.1017/S0022112065000241. URL [http://www.journals.cambridge.org/abstract\\_S0022112065000241](http://www.journals.cambridge.org/abstract_S0022112065000241).
- [11] Q. Xiao, T. T. Lim, and Y. T. Chew. Effect of acceleration on the wavy Taylor vortex flow. *Experiments in Fluids*, 32(6):639–644, 6 2002. ISSN 0723-4864. doi: 10.1007/s00348-001-0399-y. URL <http://link.springer.com/10.1007/s00348-001-0399-y>.
- [12] D. Coles and C. Van Atta. Measured distortion of a laminar circular Couette flow by end effects. *Journal of Fluid Mechanics*, 25(3):513–521, 7 1966. ISSN 0022-1120. doi: 10.1017/S0022112066000223. URL [https://www.cambridge.org/core/product/identifier/S0022112066000223/type/journal\\_article](https://www.cambridge.org/core/product/identifier/S0022112066000223/type/journal_article).
- [13] P. R. Fenstermacher, Harry L. Swinney, and J. P. Gollub. Dynamical instabilities and the transition to chaotic Taylor vortex flow. *Journal of Fluid Mechanics*, 94(1):103–128, 9 1979. ISSN 0022-1120. doi: 10.1017/S0022112079000963. URL [https://www.cambridge.org/core/product/identifier/S0022112079000963/type/journal\\_article](https://www.cambridge.org/core/product/identifier/S0022112079000963/type/journal_article).
- [14] M. Gorman and Harry L. Swinney. Spatial and temporal characteristics of modulated waves in the circular Couette system. *Journal of Fluid Mechanics*, 117(-1):123–142, 4 1982. ISSN 0022-1120. doi: 10.1017/S0022112082001554. URL [http://www.journals.cambridge.org/abstract\\_S0022112082001554https://www.cambridge.org/core/product/identifier/S0022112082001554/type/journal\\_article](http://www.journals.cambridge.org/abstract_S0022112082001554https://www.cambridge.org/core/product/identifier/S0022112082001554/type/journal_article).

- [15] Li-Hua Zhang and Harry L. Swinney. Nonpropagating oscillatory modes in Couette-Taylor flow. *Physical Review A*, 31(2):1006–1009, 2 1985. ISSN 0556-2791. doi: 10.1103/PhysRevA.31.1006. URL <https://link.aps.org/doi/10.1103/PhysRevA.31.1006>.
- [16] C. David Andereck, S. S. Liu, and Harry L. Swinney. Flow regimes in a circular Couette system with independently rotating cylinders. *Journal of Fluid Mechanics*, 164:155–183, 3 1986. ISSN 0022-1120. doi: 10.1017/S0022112086002513. URL [https://www.cambridge.org/core/product/identifier/S0022112086002513/type/journal\\_article](https://www.cambridge.org/core/product/identifier/S0022112086002513/type/journal_article).
- [17] Gregory P. King, W. Lee, Y. Li, Harry L. Swinney, and Philip S. Marcus. Wave speeds in wavy Taylor-vortex flow. *Journal of Fluid Mechanics*, 141:365–390, 4 1984. ISSN 0022-1120. doi: 10.1017/S0022112084000896. URL [https://www.cambridge.org/core/product/identifier/S0022112084000896/type/journal\\_article](https://www.cambridge.org/core/product/identifier/S0022112084000896/type/journal_article).
- [18] CARI S. DUTCHER and SUSAN J. MULLER. Spatio-temporal mode dynamics and higher order transitions in high aspect ratio Newtonian Taylor–Couette flows. *Journal of Fluid Mechanics*, 641:85, 12 2009. ISSN 0022-1120. doi: 10.1017/S0022112009991431. URL [http://www.journals.cambridge.org/abstract\\_S0022112009991431](http://www.journals.cambridge.org/abstract_S0022112009991431).
- [19] Siegfried Grossmann, Detlef Lohse, and Chao Sun. High-Reynolds Number Taylor-Couette Turbulence. *Annual Review of Fluid Mechanics*, 48(1):53–80, 2015. ISSN 0066-4189. doi: 10.1146/annurev-fluid-122414-034353.
- [20] P. ASHWIN and G. P. KING. A study of particle paths in non-axisymmetric Taylor–Couette flows. *Journal of Fluid Mechanics*, 338:341–362, 5 1997. ISSN 0022-1120. doi: 10.1017/S0022112097004990. URL [https://www.cambridge.org/core/product/identifier/S0022112097004990/type/journal\\_article](https://www.cambridge.org/core/product/identifier/S0022112097004990/type/journal_article).
- [21] N. Abcha, N. Latrache, F. Dumouchel, and I. Mutabazi. Qualitative relation between reflected light intensity by Kalliroscope flakes and velocity field in the Couette-Taylor flow system. *Experiments in Fluids*, 45(1):85–94, 2008. ISSN 07234864. doi: 10.1007/s00348-008-0465-9.
- [22] M. A. Dominguez-Lerma, Guenter Ahlers, and David S Cannell. Effects of “Kalliroscope” flow visualization particles on rotating Couette–Taylor flow. *Physics of Fluids*, 28(4):1204, 1985. ISSN 00319171. doi: 10.1063/1.864997. URL <https://aip.scitation.org/doi/10.1063/1.864997>.
- [23] Innocent Mutabazi, Nizar Abcha, Olivier Crumeyrolle, and Alexander Ezersky. Application of the Particle Image Velocimetry to the Couette-Taylor Flow. In *The Particle Image Velocimetry - Characteristics, Limits and Possible Applications*, number May. InTech, 5 2012. doi: 10.5772/45644. URL <http://www.intechopen.com/books/the-particle-image-velocimetry-characteristics-limits-and-possible-applications/application-of-the-particle-image-velocimetry-to-the-couette-taylor-flow>.
- [24] Yasushi Takeda. Quasi-periodic state and transition to turbulence in a rotating Couette system. *Journal of Fluid Mechanics*, 389:81–99, 1999. ISSN 00221120. doi: 10.1017/S0022112099005091.
- [25] G. Gauthier, P. Gondret, and M. Rabaud. Motions of anisotropic particles: Application to visualization of three-dimensional flows. *Physics of Fluids*, 10(9):2147–2154, 9 1998. ISSN 1070-6631. doi: 10.1063/1.869736. URL <http://aip.scitation.org/doi/10.1063/1.869736>.
- [26] Ö. Savas. On flow visualization using reflective flakes. *Journal of Fluid Mechanics*, 152(-1):235, 3 1985. ISSN 0022-1120. doi: 10.1017/S0022112085000672. URL [http://journals.cambridge.org/abstract\\_S0022112085000672%5Cnfile:///Users/alexandresuryadi/Library/ApplicationSupport/Papers2/Articles/1985/Savas/JournalofFluidMechanics1985Savas.pdf%5Cnpapers2://publication/uuid/F4064725-8EC8-43D9-8ADE-DB35CEE4E417](http://journals.cambridge.org/abstract_S0022112085000672%5Cnfile:///Users/alexandresuryadi/Library/ApplicationSupport/Papers2/Articles/1985/Savas/JournalofFluidMechanics1985Savas.pdf%5Cnpapers2://publication/uuid/F4064725-8EC8-43D9-8ADE-DB35CEE4E417).
- [27] Dah-Chyi Kuo and Kenneth S. Ball. Taylor–Couette flow with buoyancy: Onset of spiral flow. *Physics of Fluids*, 9(10):2872–2884, 10 1997. ISSN 1070-6631. doi: 10.1063/1.869400. URL <http://aip.scitation.org/doi/10.1063/1.869400>.

- [28] T. Alziary de Roquefort and G. Grillaud. Computation of Taylor vortex flow by a transient implicit method. *Computers and Fluids*, 1978. ISSN 00457930. doi: 10.1016/0045-7930(78)90017-8.
- [29] M. Gul, G. E. Elsinga, and J. Westerweel. Experimental investigation of torque hysteresis behaviour of Taylor-Couette Flow. *Journal of Fluid Mechanics*, 836:635–648, 2018. ISSN 14697645. doi: 10.1017/jfm.2017.809.
- [30] Kwangjai Park, Gerald L. Crawford, and Russell J. . Characteristic Lengths in the Wavy Vortex State of Taylor-Couette Flow. *Physical Review Letters*, 51(15):1352–1354, 10 1983. ISSN 0031-9007. doi: 10.1103/PhysRevLett.51.1352. URL <https://link.aps.org/doi/10.1103/PhysRevLett.51.1352>.
- [31] Klaus Kirchgässner. Die Instabilität der Strömung zwischen zwei rotierenden Zylindern gegenüber Taylor-Wirbeln für beliebige Spaltbreiten. *Zeitschrift für angewandte Mathematik und Physik ZAMP*, 12(1):14–30, 1 1961. ISSN 0044-2275. doi: 10.1007/BF01601104. URL <https://doi.org/10.1007/BF01601104> <http://link.springer.com/10.1007/BF01601104>.
- [32] M J Burin, H Ji, E Schartman, R Cutler, P Heitzenroeder, W Liu, L Morris, and S Raftopolous. Reduction of Ekman circulation within Taylor-Couette flow. *Experiments in Fluids*, 40(6):962–966, 6 2006. ISSN 1432-1114. doi: 10.1007/s00348-006-0132-y. URL <https://doi.org/10.1007/s00348-006-0132-y>.
- [33] Sedat Tokgöz. *Coherent Structures in Taylor-Couette Flow*. PhD thesis, Delft University of Technology, 2014.
- [34] Rodolfo Ostilla-Mónico, Sander G. Huisman, Tim J.G. Jannink, Dennis P.M. Van Gils, Roberto Verzicco, Siegfried Grossmann, Chao Sun, and Detlef Lohse. Optimal Taylor–Couette flow: radius ratio dependence. *Journal of Fluid Mechanics*, 747:1–29, 5 2014. ISSN 0022-1120. doi: 10.1017/jfm.2014.134. URL [https://www.cambridge.org/core/product/identifier/S0022112014001347/type/journal\\_article](https://www.cambridge.org/core/product/identifier/S0022112014001347/type/journal_article).
- [35] Rodolfo Ostilla, Richard J A M Stevens, Siegfried Grossmann, Roberto Verzicco, and Detlef Lohse. Optimal Taylor–Couette flow: direct numerical simulations. *Journal of Fluid Mechanics*, 719:14–46, 3 2013. ISSN 0022-1120. doi: 10.1017/jfm.2012.596. URL [http://www.journals.cambridge.org/abstract\\_S0022112012005964](http://www.journals.cambridge.org/abstract_S0022112012005964).
- [36] G. Segré and A. Silberberg. Behaviour of macroscopic rigid spheres in Poiseuille flow Part 2. Experimental results and interpretation. *Journal of Fluid Mechanics*, 14(1):136–157, 9 1962. ISSN 0022-1120. doi: 10.1017/S0022112062001111. URL [https://www.cambridge.org/core/product/identifier/S0022112062001111/type/journal\\_article](https://www.cambridge.org/core/product/identifier/S0022112062001111/type/journal_article).
- [37] B. P. Ho and L G Leal. Inertial migration of rigid spheres in two-dimensional unidirectional flows. *Journal of Fluid Mechanics*, 65(2):365–400, 8 1974. ISSN 0022-1120. doi: 10.1017/S0022112074001431. URL [https://www.cambridge.org/core/product/identifier/S0022112074001431/type/journal\\_article](https://www.cambridge.org/core/product/identifier/S0022112074001431/type/journal_article).
- [38] J. S. Halow and G. B. Wills. Experimental Observations of Sphere Migration in Couette Systems. *Industrial & Engineering Chemistry Fundamentals*, 9(4):603–607, 11 1970. ISSN 0196-4313. doi: 10.1021/i160036a013. URL <https://pubs.acs.org/doi/abs/10.1021/i160036a013>.
- [39] JEAN-PHILIPPE MATAS, JEFFREY F MORRIS, and ÉLISABETH GUAZZELLI. Inertial migration of rigid spherical particles in Poiseuille flow. *Journal of Fluid Mechanics*, 515:171–195, 9 2004. ISSN 0022-1120. doi: 10.1017/S0022112004000254. URL [http://www.journals.cambridge.org/abstract\\_S0022112004000254](http://www.journals.cambridge.org/abstract_S0022112004000254).
- [40] Mohamed E. Ali, Deepanjan Mitra, John A. Schuille, and Richard M. Lueptow. Hydrodynamic stability of a suspension in cylindrical Couette flow. *Physics of Fluids*, 14(3):1236–1243, 2002. ISSN 10706631. doi: 10.1063/1.1449468.
- [41] D. Dherbécourt, S. Charton, F. Lamadie, S. Cazin, and E. Climent. Experimental study of enhanced mixing induced by particles in Taylor–Couette flows. *Chemical Engineering Research and Design*, 108:109–117, 4 2016. ISSN 02638762. doi: 10.1016/j.cherd.2016.02.025. URL <https://linkinghub.elsevier.com/retrieve/pii/S0263876216000885>.

- [42] Madhu V. Majji and Jeffrey F. Morris. Inertial migration of particles in Taylor-Couette flows. *Physics of Fluids*, 30(3), 2018. ISSN 10897666. doi: 10.1063/1.5020220.
- [43] Madhu V. Majji, Sanjoy Banerjee, and Jeffrey F. Morris. Inertial flow transitions of a suspension in Taylor-Couette geometry. *Journal of Fluid Mechanics*, 835:936–969, 2018. ISSN 14697645. doi: 10.1017/jfm.2017.754.
- [44] Prashanth Ramesh, S Bharadwaj, and Meheboob Alam. Suspension Taylor–Couette flow: co-existence of stationary and travelling waves, and the characteristics of Taylor vortices and spirals. *Journal of Fluid Mechanics*, 870:901–940, 7 2019. ISSN 0022-1120. doi: 10.1017/jfm.2019.291. URL [https://www.cambridge.org/core/product/identifier/S002211201900291X/type/journal\\_article](https://www.cambridge.org/core/product/identifier/S002211201900291X/type/journal_article).
- [45] A. J. Greidanus, R. Delfos, and J. Westerweel. Drag reduction by surface treatment in turbulent Taylor-Couette flow. *Journal of Physics: Conference Series*, 318(SECTION 8), 2011. ISSN 17426596. doi: 10.1088/1742-6596/318/8/082016.
- [46] Daniel Borrero-Echeverry, Michael F. Schatz, and Randall Tagg. Transient turbulence in Taylor-Couette flow. *Physical Review E*, 81(2):025301, 2010. ISSN 1539-3755. doi: 10.1103/PhysRevE.81.025301. URL <https://link.aps.org/doi/10.1103/PhysRevE.81.025301>.
- [47] A. J. Greidanus, R. Delfos, S. Tokgoz, and J. Westerweel. Turbulent Taylor–Couette flow over riblets: drag reduction and the effect of bulk fluid rotation. *Experiments in Fluids*, 56(5):1–13, 2015. ISSN 07234864. doi: 10.1007/s00348-015-1978-7.
- [48] Daniel Borrero-Echeverry, Christopher J. Crowley, and Tyler P. Riddick. Rheoscopic fluids in a post-Kalliroscope world. *Physics of Fluids*, 30(8), 2018. ISSN 10897666. doi: 10.1063/1.5045053.
- [49] Oliver Richter, Heike Hoffmann, and Bettina Kraushaar-Czarnetzki. Effect of the rotor shape on the mixing characteristics of a continuous flow Taylor-vortex reactor. *Chemical Engineering Science*, 63(13):3504–3513, 7 2008. ISSN 00092509. doi: 10.1016/j.ces.2008.04.003. URL <https://linkinghub.elsevier.com/retrieve/pii/S0009250908001796>.
- [50] T. TSUKAHARA, N. TILLMARK, and P. H. ALFREDSSON. Flow regimes in a plane Couette flow with system rotation. *Journal of Fluid Mechanics*, 648:5–33, 4 2010. ISSN 0022-1120. doi: 10.1017/S0022112009993880. URL [http://www.journals.cambridge.org/abstract\\_S0022112009993880https://www.cambridge.org/core/product/identifier/S0022112009993880/type/journal\\_article](http://www.journals.cambridge.org/abstract_S0022112009993880https://www.cambridge.org/core/product/identifier/S0022112009993880/type/journal_article).
- [51] John J Hegseth. Turbulent spots in plane Couette flow. *Physical Review E*, 54(5):4915–4923, 11 1996. ISSN 1063-651X. doi: 10.1103/PhysRevE.54.4915. URL <https://link.aps.org/doi/10.1103/PhysRevE.54.4915>.
- [52] K. ATKHEN, J. FONTAINE, and J. E. WESFREID. Highly turbulent Couette–Taylor bubbly flow patterns. *Journal of Fluid Mechanics*, 422:S0022112000001592, 11 2000. ISSN 00221120. doi: 10.1017/S0022112000001592. URL [http://www.journals.cambridge.org/abstract\\_S0022112000001592](http://www.journals.cambridge.org/abstract_S0022112000001592).
- [53] P. Wulf, C. Egbers, and H. J. Rath. Routes to chaos in wide-gap spherical Couette flow. *Physics of Fluids*, 11(6):1359–1372, 6 1999. ISSN 1070-6631. doi: 10.1063/1.870001. URL <http://aip.scitation.org/doi/10.1063/1.870001>.
- [54] Carl D. Meinhart and Steven T. Wereley. The theory of diffraction-limited resolution in microparticle image velocimetry. *Measurement Science and Technology*, 14(7):1047–1053, 7 2003. ISSN 0957-0233. doi: 10.1088/0957-0233/14/7/320. URL <http://stacks.iop.org/0957-0233/14/i=7/a=320?key=crossref.d4bcef7dcc96e66dcc7f8d48b43a687b>.
- [55] M. G. Olsen and R. J. Adrian. Out-of-focus effects on particle image visibility and correlation in microscopic particle image velocimetry. *Experiments in Fluids*, 29(7):S166–S174, 12 2000. ISSN 0723-4864. doi: 10.1007/s003480070018. URL <http://link.springer.com/10.1007/s003480070018>.
- [56] K. Koeltzsch, Y. Qi, R. S. Brodkey, and J. L. Zakin. Drag reduction using surfactants in a rotating cylinder geometry. *Experiments in Fluids*, 34(4):515–530, 2003. ISSN 07234864. doi: 10.1007/s00348-003-0590-4.

- [57] Dennis P. M. van Gils, Sander G. Huisman, Gert-Wim Bruggert, Chao Sun, and Detlef Lohse. Torque Scaling in Turbulent Taylor-Couette Flow with Co- and Counterrotating Cylinders. *Physical Review Letters*, 106(2):024502, 1 2011. ISSN 0031-9007. doi: 10.1103/PhysRevLett.106.024502. URL <https://link.aps.org/doi/10.1103/PhysRevLett.106.024502>.
- [58] BRUNO ECKHARDT, SIEGFRIED GROSSMANN, and DETLEF LOHSE. Torque scaling in turbulent Taylor-Couette flow between independently rotating cylinders. *Journal of Fluid Mechanics*, 581:221, 6 2007. ISSN 0022-1120. doi: 10.1017/S0022112007005629. URL [http://www.journals.cambridge.org/abstract\\_S0022112007005629](http://www.journals.cambridge.org/abstract_S0022112007005629).
- [59] T. T. Lim and K. S. Tan. A note on power-law scaling in a Taylor-Couette flow. *Physics of Fluids*, 16(1):140–144, 1 2004. ISSN 1070-6631. doi: 10.1063/1.1631417. URL <http://aip.scitation.org/doi/10.1063/1.1631417>.
- [60] Daniel P Lathrop, Jay Fineberg, and Harry L Swinney. Transition to shear-driven turbulence in Couette-Taylor flow. *Physical Review A*, 46(10):6390–6405, 11 1992. ISSN 1050-2947. doi: 10.1103/PhysRevA.46.6390. URL <https://link.aps.org/doi/10.1103/PhysRevA.46.6390>.
- [61] Gregory S. Lewis and Harry L. Swinney. Velocity structure functions, scaling, and transitions in high-Reynolds-number Couette-Taylor flow. *Physical Review E*, 59(5):5457–5467, 5 1999. ISSN 1063-651X. doi: 10.1103/PhysRevE.59.5457. URL <https://link.aps.org/doi/10.1103/PhysRevE.59.5457>.
- [62] F. Ravelet, R. Delfos, and J. Westerweel. Influence of global rotation and Reynolds number on the large-scale features of a turbulent Taylor-Couette flow. *Physics of Fluids*, 22(5):1–8, 2010. ISSN 10706631. doi: 10.1063/1.3392773.
- [63] B. Dubrulle, O. Dauchot, F. Daviaud, P. Y. Longaretti, D. Richard, and J. P. Zahn. Stability and turbulent transport in Taylor-Couette flow from analysis of experimental data. *Physics of Fluids*, 17(9):1–19, 2005. ISSN 10706631. doi: 10.1063/1.2008999.
- [64] Élisabeth Guazzelli and Olivier Pouliquen. Rheology of dense granular suspensions. *Journal of Fluid Mechanics*, 852:P1, 10 2018. ISSN 0022-1120. doi: 10.1017/jfm.2018.548. URL [https://www.cambridge.org/core/product/identifier/S0022112018005487/type/journal\\_article](https://www.cambridge.org/core/product/identifier/S0022112018005487/type/journal_article).
- [65] J. J. J. Gillissen and H. J. Wilson. Taylor-Couette instability in sphere suspensions. *Physical Review Fluids*, 4(4):043301, 4 2019. ISSN 2469-990X. doi: 10.1103/PhysRevFluids.4.043301. URL <https://link.aps.org/doi/10.1103/PhysRevFluids.4.043301>.